

Photocurrent Limiting Mechanisms in Organic Bulk Heterojunction Solar Cells

A Dissertation

Presented to
the faculty of the School of Engineering and Applied Science
University of Virginia

in partial fulfillment
of the requirements for the degree

Doctor of Philosophy

by

Kejia Li

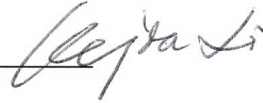
December

2012

APPROVAL SHEET

The dissertation
is submitted in partial fulfillment of the requirements
for the degree of
Doctor of Philosophy

Kejia Li
AUTHOR



The dissertation has been read and approved by the examining committee:

Joe C. Campbell

Advisor

Archie L. Holmes

Robert M. Weikle

Lloyd R. Harriott

David Green

Accepted for the School of Engineering and Applied Science:



Dean, School of Engineering and Applied Science

December
2012

**This thesis is dedicated
to my parents Jingqun Li and Lingying Tang
for their love and endless support,
and to my husband Yang Fu,
who is always the comfort of my heart.**

Abstract

As we use more energy as a society, there is a greater need to become less reliant on non-renewable energy sources. Photovoltaics (PV), as a method of harvesting sunlight and converting it into electricity, provide a potential way of producing clean renewable energy.

Organic bulk heterojunction (BHJ) solar cells featured with low-cost, large-area and thin-film manufacture, have become more viable with the recent demonstration with power conversion efficiencies (PCE) as high as 10.7%. However, there is still a room for further improvement to reach the thermodynamic PCE limit of ~22%. For organic BHJ solar cells, the efficiency is essentially limited by the low short-circuit current density, which is determined by four sequential steps that are necessary to transform incident photons to free charge carriers. These steps are photo absorption and exciton formation, exciton diffusion, polaron pair dissociation and free polaron collection. In order to know the extent to which each of these steps limits the efficiency, a systematic study to analyze the limiting mechanisms is beneficial.

In this work, we report approaches that are capable of providing insight into these processes by applying several complementary experimental techniques and theoretical calculations. The material system that are studied are poly(3-hexylthiophene) (P3HT): phenyl-C₆₁-butyric acid methyl ester (PC₆₁BM), poly(3-hexylthiophene-thiophene-diketopyrrolopyrrole (P3HTT-DPP-10%): PC₆₁BM, benzothiadiazole (BTD) and thienopyrazine (TP) based polymers (P3HTT-BTD and P3HTT-TP): PC₆₁BM. Compared to P3HT: PC₆₁BM solar cells, the other three solar cells

have a much broadband absorption, but have a big variation in short circuit current. Therefore, it is quite intriguing to explore the reasons behind that.

For absorption, the optical transfer-matrix theory is applied on the multi-thin-layer structure of organic BHJ solar cells. The complex refractive index is extracted. Meanwhile, the optical electric field and the absorption efficiency are calculated and compared. The exciton diffusion efficiency is analyzed by using J-V measurements at large reverse bias. The breakdown mechanisms are also discussed and the tunneling effect is found to be dominating in most devices. The polaron pair dissociation efficiency is analyzed using the well known Onsager-Braun model. It is found that polaron pair decay rate plays an important role on polaron pair dissociation since other parameters are similar for all the cells. For free polaron pair collection, three techniques: transient photoconductivity, forward-to-zero transient-current response, and electric field dependent photoresponse techniques, are developed and used to measure the recombination lifetime of organic BHJ solar cells. Meanwhile, by measuring V_{oc} vs. light intensity, deep trap-assisted SRH recombination is found in P3HTT-TP:PC₆₁BM solar cells, and trap-assisted Auger recombination is found in P3HTT-BTD:PC₆₁BM solar cells. In addition to the experiments, a new organic BHJ solar cell numerical model including non-uniform photon absorption, exciton diffusion, non-geminate recombination, and the effect of series resistance, R_s , and shunt resistance, R_{sh} , are considered and added to the classic drift-diffusion model. The I-V curves have been simulated under AM1.5 condition and compared with experiment data. The combination of these studies show that trap assisted recombination is still restrictive in some BHJ solar cells.

Acknowledgement

The Ph.D study is a strict but a joyful scientific training. To make through it, I'd like to thank to the people who gave me tremendous support in these years.

First and foremost I would like to thank my supervisor, Dr. Joe C. Campbell, for his patient guidance, continual support and encouragement during my Ph.D study. I learned a lot from him, not only about how to tackle the experimental/theoretical problems, but also about the vision, the presentation skills, and the way to keep a good relationship with your collaborators. I also appreciate the research freedom that Dr. Joe C. Campbell gave to me, which allows me to deliberate, to try and to pursuit without worrying.

To the rest of my advising committee; Profs. Archie Holmes, Lloyd R. Harriott, David Green and Robert M. Weikle, thank you for your advice and valuable feedback.

I would also like to thank to my senior group members, Dr. Chong Hu, Dr. Han-Din Liu, Dr. Dion C. McIntosh-Dorsey, Dr. Qiugui Zhou, who have been my laboratories mentors and gave me useful suggestions through my studies. To my group members Dr. Andreas Beling, Dr. Xiaogang Bai, Dr. Xiaoguang Zheng, Dr. Huapu Pan, Dr. Zhi Li, Dr. Nabanita Majumdar, Hao Chen, Zhiwen Lu, Yang Fu, Lijun Li, Wenlu Sun and Yaojia Chen who have been both friends and research sounding boards.

Especially the solar cell group: Lijun Li, for useful discussion of technique questions, and collaboration of setting up the solar cell fabrication and characterization lab from the beginning. Thank to Yang Shen for teaching me the fabrication and sharing research opinions constantly. Thank to Professor Stephen Bradford, P. Daniel Dapkus, Dr. Cody Schlenker, Professor Barry C. Thompson, his students Petr Khlyabich and Beate

Burkhurt at the University of Southern California for insight into the dynamics of organic semiconductors. Especially Professor Barry C. Thompson group, for providing the polymers to us, great suggestion on device fabrication and experiment data interpretation.

I would also like to thank the staff members of the Microfabrication Lab at Uva, administrative staff of the Electrical Engineering Department in particular our group secretary Brenda Crider for the support through my studies.

Table of Content

Abstract.....	i
Acknowledgement.....	iii
List of Figures.....	ix
List of Tables	xv
List of Symbols and Acronyms	xvi
Chapter 1. Introduction	1
1.1 Motivation.....	1
1.2 Device physics: charge transfer processes	2
1.3 Photovoltaic characteristics	3
1.4 Thesis goal and organization	5
Chapter 2. Fundamentals of organic bulk heterojunction (BHJ) solar cells	7
2.1 Organic BHJ solar cells physics model	7
2.1.1 Metal-Insulator-Metal (MIM) model.....	7
2.1.2 Basic equations	8
2.1.3 Generation and recombination.....	9
2.1.4 Boundary conditions	10
2.2 Fabrication of organic BHJ solar cells.....	10
2.3 Characterization of organic BHJ solar cells.....	15
2.3.1 Refractive index measurement.....	15
2.3.2 Current-voltage and capacitance-voltage measurements.....	15
2.3.3 External quantum efficiency measurements	16

2.3.4 Mobility measurements.....	17
Chapter 3. Photon absorption and exciton generation.....	19
3.1 Introduction.....	19
3.2 Multi-layer thin-film interference model.....	20
3.3 Refractive index.....	24
3.4 Optical electrical field profile.....	25
3.5 Total absorption of AM1.5.....	27
3.6 Exciton generation.....	28
Chapter 4. Exciton diffusion.....	29
4.1 Introduction.....	29
4.2 Theory: determine the exciton diffusion efficiency by measuring J-V curves.....	30
4.3 Exciton generation rate, J-V curve, and exciton diffusion efficiency under AM1.5 illumination.....	33
4.4 Breakdown mechanism study by varying the temperature.....	37
4.5 Summary.....	41
Chapter 5. Polaron pair dissociation.....	42
5.1 Introduction.....	42
5.2 Onsager-Braun model.....	42
5.3 Polaron pair dissociation probability.....	44
5.4 Summary.....	48
Chapter 6. Free polaron collection.....	49
6.1 Introduction.....	49
6.2 Transient photoconductivity.....	51

6.3 Forward-to-zero transient current response	54
6.3.1 introduction	54
6.3.2 The theory for transient current response	55
6.3.3 Experiment results and discussion	58
6.4 Electrical-field-dependent photoresponse	59
6.5 Free polaron collection efficiency for four types of polymer:PCB ₆₁ M solar cells ..	63
6.6 Thermal annealing effect on mobility and lifetime	68
6.7 Summary	72
Chapter 7. Numerical simulation	74
7.1 Introduction and methodology	74
7.1.1 Introduction	74
7.1.2 Device model and numerical method	75
7.2 Simulation results for P3HT:PC ₆₁ BM solar cells	80
7.3 Simulation results for P3HTT-DPP-10%:PC ₆₁ BM solar cells	85
7.4 Simulation results for P3HTT-TP:PC ₆₁ BM solar cells	90
7.5 Simulation results for P3HT-BTD:PC ₆₁ BM solar cells	94
7.6 Discussion and summary	99
Chapter 8. Overview, summary, and future work.....	100
8.1 Overview of efficiencies	100
8.2 Summary	103
8.3 Future work	107
8.3.1 Enhancement of absorption by fluorescence structure design	107

8.3.2 Relationship between energetic disorder and fill factor by numerical simulation	108
8.3.3 Morphology effect on P3HTT-DPP-10%: PCB ₆₁ M P3HTT-TP: PCB ₆₁ M and P3HTT-BTD: PCB ₆₁ M solar cells performance	109
Reference	110
Appendix A: Publications	120

LIST OF FIGURES

Figure 1-1. Two approaches to heterojunction solar cells.	2
Figure 1-2. A typical current versus voltage curve of a solar cell under illumination.	4
Figure 2-1. A typical BHJ solar cell structure, which consists of an anode (Indium Tin Oxide (ITO)) layer, a Poly(3,4-ethylenedioxythiophene) poly(styrenesulfonate) (PEDOT) layer, a polymer:fullerene layer and a cathode (Al) layer.	7
Figure 2-2. (a) Schematic of the energy levels (b) Device model in flat band condition for a poly(3-hexylthiophene) (P3HT): phenyl-C ₆₁ -butyric acid methyl ester (PC ₆₁ BM)..	7
Figure 2-3. The charge generation and recombination process.	9
Figure 2-4. Structures of P3HT, P3HTT-DPP-10%, P3HTT-TP and P3HTT-BTD polymers.....	11
Figure 3-1. Absorption of poly (3-hexylthiophene) (P3HT), which is a typical semiconducting polymer, and poly (3-hexylthiophene-thiophene-diketopyrrolopyrrole-10%) (P3HTT-DPP-10%), a donor-acceptor copolymer, and single crystalline silicon. .	19
Figure 3-2. The solar cell consists of a stack of m thin-film layers. Light is incident on the substrate from the left, with intensity I_0 and travels to the right. Each layer j (j=1, 2, ..., m) has a thickness d_j . The optical electric field inside each layer is described as E^+ for waves traveling from left to right and E^- for waves traveling from right to left.	20
Figure 3-3. The whole structure considering the substrate.	22
Figure 3-4. (a) Refractive index η and (b) Extinction coefficient κ of four polymer:PC ₆₁ BM thin films.....	25

Figure 3-5. Optical electrical field inside the (a) P3HT:PC ₆₁ BM, (b)P3HTT-DPP-10%: PC ₆₁ BM , (c) P3HTT-TP:PC ₆₁ BM and (d) P3HTT-BTD: PC ₆₁ BM solar cells at 630nm. In this figure, region I, II, III and VI represent 280nm ITO layer, 40nm PEDOT:PSS layer, active layer (polymer: PC ₆₁ BM) and 100nm Al layer, respectively.	26
Figure 3-6. Absorption of four polymer: PC ₆₁ BM thin films.	27
Figure 4-1. Exciton generation rate for (a) P3HT:PC ₆₁ BM, (b)P3HTT-DPP-10%: PC ₆₁ BM , (c) P3HTT-TP:PC ₆₁ BM and (d) P3HTT-BTD: PC ₆₁ BM solar cells.	33
Figure 4-2. (a) J - V curves and (b) J versus electric field, E , curves for solar cells under AM1.5 illumination.	35
Figure 4-3. (a) J - V curves and (b) J - E curves for solar cells under a 532nm laser illumination.	38
Figure 4-4. (a) Dark current and (b) Photo current for P3HT:PCB ₆₁ M solar cells.	38
Figure 4-5. (a) Dark current and (b) Photo current for P3HTT-DPP-10%:PCB ₆₁ M solar cells.	39
Figure 4-6 (a) dark current and (b) photo current for P3HTT-TP:PCB ₆₁ M solar cells. ...	40
Figure 4-7. (a) Dark current and (b) Photo current for P3HTT-BTD:PCB ₆₁ M solar cells.	40
Figure 5-1. C-V curves for (a) P3HT:PC ₆₁ BM, (b)P3HTT-DPP-10%: PC ₆₁ BM , (c) P3HTT-TP:PC ₆₁ BM and (d) P3HTT-BTD: PC ₆₁ BM solar cells.	46
Figure 5-2. Polaron pair dissociation probability for four different polymer:PC ₆₁ BM solar cells.	47
Figure 6-1. A typical circuit for measuring transient photoresponse.	51

Figure 6-2. Transient photocurrent at different applied voltages for a P3HT/PC ₆₁ BM solar cell at room temperature.	53
Figure 6-3. $\tau_{1/e}$ as a function of internal voltage.	54
Figure 6-4. (a) Basic switching circuit apparatus and (b) typical current and voltage switching characteristics.	55
Figure 6-5. Measurement circuit to characterize the transient behavior of BHJ devices.	55
Figure 6-6. Current and voltage switching characteristics of a P3HT:PCBM device.	58
Figure 6-7. Photo current versus applied bias and internal electric field.....	61
Figure 6-8. Transient photoconductivity for a P3HT/PCBM solar cell at room temperature. (a) Transient photoresponse at different internal electric field. (b) The sweep out time is determined by the intersection of two linear fitting lines.	61
Figure 6-9. Probability of geminate pair separation versus internal electric field.....	62
Figure 6-10. Transient photocurrent response of (a) P3HT:PC ₆₁ BM, (b) P3HTT-DPP-10%:PC ₆₁ BM, (c) P3HTT-TP:PC ₆₁ BM and (d) P3HTT-BTD:PC ₆₁ BM solar cells at different applied bias.....	64
Figure 6-11. V_{oc} vs. light intensity (I) at room temperature.....	65
Figure 6-12. The transient lifetimes for different polymer:PC ₆₁ BM solar cells at different applied bias.	66
Figure 6-13. Transient photoconductivity measurement for sweep out time. The black lines are transient photoresponse at -2V and the red lines are linear fitting for the black curves. The intersection of two red lines is the sweep out time point.	67
Figure 6-14. Dark current densities (J) in 55:45 wt. % blends of P3HT:PCBM devices as a function of annealing temperature (a) electron-only device and (b) hole-only device. .	70

Figure 6-15. (a) Typical current and voltage switching characteristics of a P3HT:PCBM solar cell and (b) lifetime as a function of annealing temperature.....	71
Figure 7-1. An equivalent circuit for a real solar cell.	78
Figure 7-2. Photon generation rate for P3HT:PC ₆₁ BM solar cells.	81
Figure 7-3. Comparison between experimental data and simulation results for P3HT:PC ₆₁ BM solar cells.	82
Figure 7-4. Electric potential, electric field, recombination rate and current densities at short circuit condition.	83
Figure 7-5. Electric potential, electric field, recombination rate and current densities at open circuit condition.	83
Figure 7-6. Electric potential, electric field, recombination rate and current densities at maximum power condition.	84
Figure 7-7. Electric field at different applied bias for P3HT:PC ₆₁ BM solar cells.....	85
Figure 7-8. Photon generation rate for P3HTT-DPP-10%:PC ₆₁ BM solar cells.....	86
Figure 7-9. Comparison between experiment data and simulation results for P3HTT-DPP-10%:PC ₆₁ BM solar cells.	87
Figure 7-10. Electric potential, electric field, recombination rate and current densities at short circuit condition.	88
Figure 7-11. Electric potential, electric field, recombination rate and current densities at open circuit condition.	88
Figure 7-12. Electric potential, electric field, recombination rate and current densities at maximum power condition.	89

Figure 7-13. Electric field at different applied bias for P3HTT-DPP-10%:PC ₆₁ BM solar cells.	89
Figure 7-14. photon generation rate for P3HTT-TP:PC ₆₁ BM solar cells.	90
Figure 7-15. Comparison between experiment data and simulation results for P3HTTP:PC ₆₁ BM solar cells.	92
Figure 7-16. Electric potential, electric field, recombination rate, and current densities at short circuit condition.	92
Figure 7-17. Electric potential, electric field, recombination rate, and current densities at open circuit condition.	93
Figure 7-18. Electric potential, electric field, recombination rate, and current densities at maximum power condition.	93
Figure 7-19. Electric field at different applied bias for P3HTT-DPP-10%:PC ₆₁ BM solar cells.	94
Figure 7-20. Photon generation rate for P3HT:PC ₆₁ BM solar cells.	95
Figure 7-21. Comparison between measured (black curve) and simulated current-voltage curves with (red dots) and without (blue curve) R _s and R _{sh} for P3HTT-BTD:PC ₆₁ BM solar cells.	96
Figure 7-22. Electric potential, electric field, recombination rate, and current densities at short circuit condition.	97
Figure 7-23. electric potential, electric field, recombination rate and current densities at open circuit condition.	97
Figure 7-24. Electric potential, electric field, recombination rate and current densities at maximum power condition.	98

Figure 7-25. Electric field at different applied bias for P3HTT-BTD:PC ₆₁ BM solar cells.	
.....	98
Figure 8-1. (a) EQE and (b) IQE for four types of polymer:PC ₆₁ BM solar cells.	102
Figure 8-2. BHJ solar cells with back fluorescence converter (a) a typical BHJ device with a back fluorescence converter (b) a converted BHJ device with a back fluorescence converter.	108

LIST OF TABLES

Table 2-1. Photovoltaic properties of P3HT, P3HTT-DPP-10%, P3HTT-TP and P3HTT-BTD with PC ₆₁ BM as an acceptor.	11
Table 3-1. Photovoltaic properties and absorption efficiency of P3HT, P3HTT-DPP-10%, P3HTT-TP and P3HTT-BTD with PC ₆₁ BM as an acceptor.	24
Table 4-1. Exciton diffusion efficiency of P3HT:PC ₆₁ BM, P3HTT-DPP-10%: PC ₆₁ BM, P3HTT-TP: PC ₆₁ BM and P3HTT-BTD: PC ₆₁ BM solar cells.	36
Table 5-1. Parameters used in the Onsager-Braun model calculation for P3HT:PC ₆₁ BM and P3HTT-DPP-10%:PC ₆₁ BM solar cells.	44
Table 5-2. Parameters used in the Onsager-Braun model calculation for P3HTT-TP:PC ₆₁ BM and P3HTT-BTD:PC ₆₁ BM solar cells.	44
Table 6-1. Photovoltaic properties and free polaron collection characteristics of four types of polymer:PC ₆₁ BM solar cells.	68
Table 7-1. Simulation parameters for P3HT:PC ₆₁ BM solar cells.	81
Table 7-2. Simulation parameters for P3HTT-DPP-10%:PC ₆₁ BM solar cells.	86
Table 7-3. Simulation parameters for P3HT:PC ₆₁ BM solar cells.	90
Table 7-4. Simulation parameters for P3HTT-BTD:PC ₆₁ BM solar cells.	95
Table 8-1. Efficiency summary for four polymer:PC ₆₁ BMS cells at 640nm.	100

LIST OF SYMBOLS AND ACRONYMS

α	Absorption coefficient
ε_0	Permittivity of free space
ε_r	Relative permittivity (dielectric constant)
μ_0	Zero-field mobility
$\mu_{n,p}$	Free polaron mobilities
λ	Wavelength
η_a	Absorption efficiency
η_{cc}	free polaron collection efficiency
η_{cd}	Polaron pair dissociation efficiency
η_{ed}	Average exciton diffusion efficiency
η_{eqe}	External quantum efficiency
η_{iqe}	Internal quantum efficiency
ψ	Electric potential
a_0	Initial distance between polaron pairs
c	The speed of the light in vacuum
d	Thickness of the active layer
h	Planck's constant
k	Boltamann's constant
k_r	Polaron pair recombination rate
k_{diss}	Polaron pair dissociation rate
k_f	Polaron pair decay rate

k_{rec}	Recombination coefficient
$n = \eta + i\kappa$	Complex refractive index
n	Negative free polaron density
p	Positive free polaron density
q	Elementary charge
t_r	Free polaron average recombination time
t_r	Free polaron sweep-out time
A	Area
C	Capacitance
$D_{n,p}$	Free polaron diffusion coefficients
ΔE_{HL}	Energy difference between HOMO of the donor and LUMO of the acceptor
E	Electric field
E_B	Polaron pair binding energy
E_{trap}	Difference between the trap energy level and the intrinsic Fermi level
FF	Fill factor
G	Free polaron generation rate
G_{PP}	Polaron pair generation rate
$G_{exciton}$	Exciton generation rate
J_1	Bessel function of order one
$J_{n(p)}$	Negative/positive free polaron current density
J_{sc}	Short-circuit current density
N_{HOMO}	Density of state of donor HOMO level
N_{LUMO}	Density of state of acceptor LUMO level

P_{diss}	Polaron pair dissociation probability
PCE	Power conversion efficiency
R	Free polaron recombination rate
R_s	Series resistance
R_{sh}	Shunt resistance
T	Temperature
X	Polaron pair density
$U_{n(p)}$	Negative/positive free polaron net generation rate
V_a	Applied voltage
V_{oc}	Open-circuit voltage

Chapter 1. Introduction

1.1 Motivation

In the past two decades there has been renewed interest in solar energy, as a source of renewable energy. The total solar energy absorbed by Earth's atmosphere, oceans and land masses is enormous: $\sim 3.86 \times 10^{24}$ J per year [1]. In 2008, this was four orders of magnitude higher than the total world primary energy consumption in one year [2]. Photovoltaics (PV), as a method of harvesting sunlight and converting it into electricity, provide a potential way of producing clean energy.

In the PV market, different types of solar cells are characterized by different efficiencies and cost [3]. Multijunction concentrators, single-junction GaAs, crystalline Si, multicrystalline Si, copper indium gallium selenide (CIGS), and organic photovoltaics (OPV) are the primary types of cells, with highest efficiencies of $37.5 \pm 1.3\%$, $28.8 \pm 0.9\%$, $25.0 \pm 0.5\%$, $20.4 \pm 0.5\%$, $19.6 \pm 0.6\%$, and $10.0 \pm 0.3\%$, respectively. The most widely used commercial cells are fabricated from inorganic semiconductors, because of their higher efficiency and stability. On the other hand, organic solar cells are attractive because of their ease of processing, mechanical flexibility, and potential for fabrication of low-cost large-areas cells [4, 5].

The bulk heterojunction (BHJ) structure device, one type of organic solar cell, has recently achieved $10.0 \pm 0.3\%$ power conversion efficiency [3]. The breakthroughs in OPV performance have stimulated intensive research on the device physics of organic solar cells [6-8] and synthesis of new organic compounds [9, 10]. Meanwhile, there is

still room for further improvement since the thermodynamic efficiency limit estimated for single junction binary blend bulk heterojunction (BHJ) solar cell is 22% [11] with realistic estimates of the ultimate achievable efficiency for binary blend BHJ solar cells between 10 – 12% [12, 13] and 14 – 15% is in case of organic tandem solar cells[12, 14].

1.2 Device physics: charge transfer processes

The heterojunction solar cells can be realized in two approaches, as it's shown in Fig.1-1. The bi-layer heterojunction structure consists of two active layers: acceptor layer and donor layer, while a bulk heterojunction solar cell is formed by one active layer with donor properties and acceptor properties together. Compared with the bi-layer heterojunction structure, the charge transfer at the donor-acceptor interface of a BHJ solar cell is facilitated because more donor-acceptor interfaces are created and the length scale of the donor and acceptor phases are on the order of the exciton diffusion length.

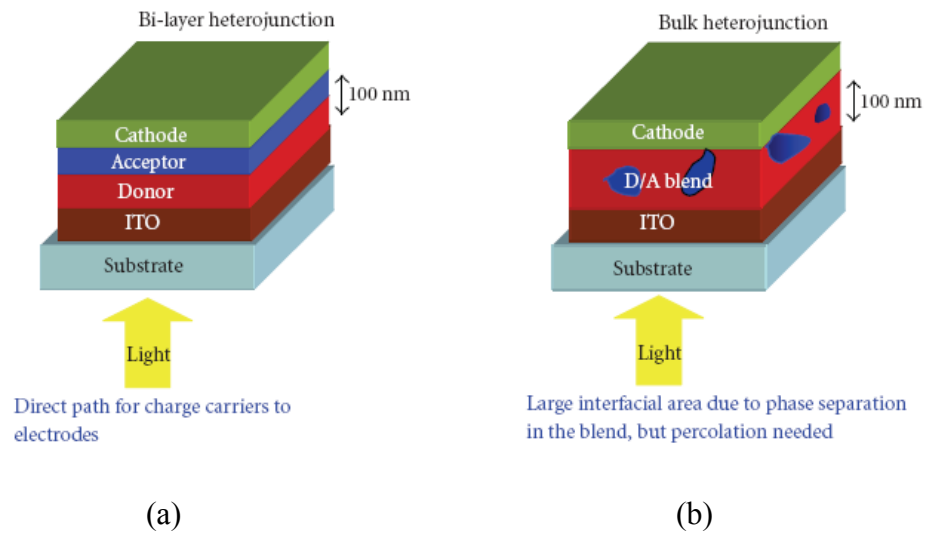


Figure 1-1. Two approaches to heterojunction solar cells.

In BHJ devices, the operation of a bulk heterojunction solar cell can be summarized in four basic steps: (a) photon absorption and exciton generation, (b) exciton diffusion to the donor/acceptor interface, (c) polaron pair dissociation and (d) free polaron collection [15, 16]. In order to improve the efficiency of this type of solar cell, it is important to know the loss mechanisms associated with each of these sequential effects and to determine the extent to which each limits the efficiency. This work will focus on analyzing charge transport and loss mechanisms in BHJ solar cells. Several possible methods to improve the power conversion efficiency are also suggested.

1.3 Photovoltaic characteristics

The power conversion efficiency (PCE) of organic solar cells is defined as $\eta = (J_{sc} \cdot V_{oc} \cdot FF) / P_{in}$, where J_{sc} is the short-circuit current density, V_{oc} is the open-circuit voltage, FF is the fill factor and P_{in} is input power in the form of solar radiation. Consequently, simultaneous optimization of the above mentioned parameters is necessary to maximize the solar cell efficiency.

Open circuit voltage (V_{oc})

The open circuit voltage is the voltage at which the current is zero. In organic solar cells, V_{oc} of the solar cell can be roughly approximated as the difference between the highest occupied molecular orbital (HOMO) level of the donor and the lowest unoccupied molecular orbital (LUMO) of the acceptor [17] even though other factors are found to influence the V_{oc} [7, 18, 19]. It can be expressed as [20, 21]

$$V_{oc} = \frac{\Delta E_{HL}}{q} - \frac{kT}{q} \ln\left(\left(\frac{k_r}{k_{diss}}\right) \frac{k_{rec} N_{HOMO} N_{LUMO}}{J_x / a_0}\right) \quad (1-1)$$

where ΔE_{HL} is the energy difference between HOMO of the donor and LUMO of the acceptor; k_r and k_{diss} are the polaron pair recombination and dissociation rates, respectively; k_{rec} is the recombination coefficient; N_{HOMO} and N_{LUMO} are donor HOMO and acceptor LUMO edge densities of states; J_X is exciton current density that reaches the heterojunction; and a_0 is the initial distance between polaron pairs.

Short circuit current density (J_{sc})

Short circuit current is the current for which the voltage drops to zero, which is illustrated a point a in Fig. 1-2. In organic BHJ solar cells, the short circuit current is strongly related to the four steps to generate current discussed above.

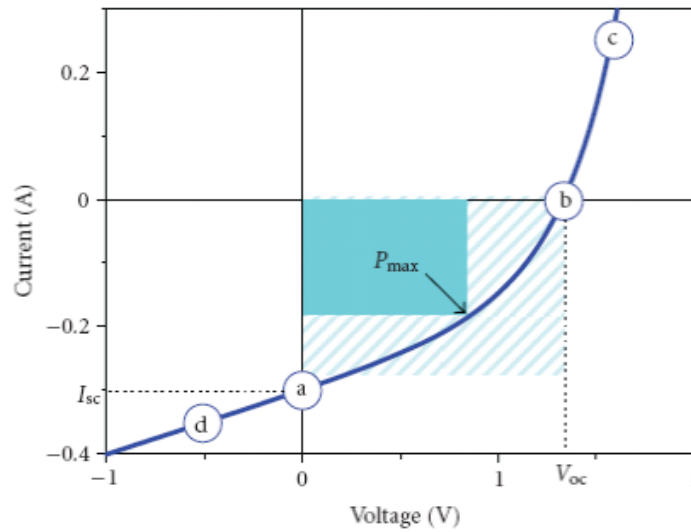


Figure 1-2. A typical current versus voltage curve of a solar cell under illumination.

Fill factor (FF)

The fill factor (FF) is defined as the ratio of the actual maximum power delivered by the solar cell to the product of I_{sc} and V_{oc} . Ideally, the FF should be unity, but losses due to transport and recombination result in values between 0.2 and 0.7 for organic

photovoltaic devices [5]. The value of FF on the other hand can be attributed to the active layer morphology [22, 23] and charge transport through the bulk [24].

Series resistance (R_s) and shunt resistance (R_{sh})

The series resistance and shunt resistance are two other important parameters that can affect the power conversion efficiency by influencing the fill factor of the solar cells.

The series resistance is from ohmic loss, which could be estimated from the current-voltage curve slope at large forward voltage where the current flow is not longer limited by the internal carrier recombination but by the potential drop [25]. It's well known that a high series resistance reduces the fill factor, thus reducing cell efficiency [26, 27]. For BHJ solar cells, the series resistance consists of two parts: contact resistance and bulk resistance. Because the bulk resistance is high, the series resistance of a BHJ can achieve $20 \text{ } \Omega \text{ cm}^2$ and the loss due to I^2R is $\sim 30\%$ of the total output power [28]. Optimizing the active layer thickness and the annealing temperature during the fabrication could lower the contact resistance, as well as the bulk resistance [29].

The shunt resistance is from leakage current and could be extracted as the slope of the illuminated I-V curve at J_{sc} . It's well known that a low shunt resistance reduces the fill factor, thus reducing cell efficiency. The R_{sh} typically comes from leakage currents. In practice, the shunt resistance has much less effect than the series resistance [26].

1.4 Thesis goal and organization

The primary focus of this work is to study the photocurrent limitation mechanisms on organic bulk heterojunction solar cells. By applying complementary simulation tools and experiment techniques, the efficiency of each charge transport step was determined

for four different polymer/phenyl-C61-butyric acid methyl ester (PC₆₁BM) BHJ solar cells.

The dissertation is divided into eight chapters. Chapter 1 introduces the motivation and goals of this dissertation. Chapter 2 provides the fundamentals of organic BHJ solar cells, including device physics and models, device fabrication and characterization methods. Chapter 3 to Chapter 6 analyze the charge transport efficiency for absorption, exciton diffusion, exciton dissociation and free polaron transport of BHJ solar cells, respectively. For each step, four different polymer/ PC₆₁BM solar cells are measured and compared. In Chapter 4, the breakdown mechanisms are also investigated based on the current density versus voltage at large reverse bias. In Chapter 6, the thermal annealing effects on mobility and free polaron recombination lifetime are also discussed in order to give a better understanding of recombination mechanisms. Numerical simulations are presented in Chapter 7. The free polaron distribution, electrical field and potential are analyzed under dark condition, short-circuit condition and open-circuit condition. The conclusion and the future works are discussed in Chapter 8.

Chapter 2. Fundamentals of organic bulk heterojunction (BHJ) solar cells

2.1 Organic BHJ solar cells physics model

2.1.1 Metal-Insulator-Metal (MIM) model

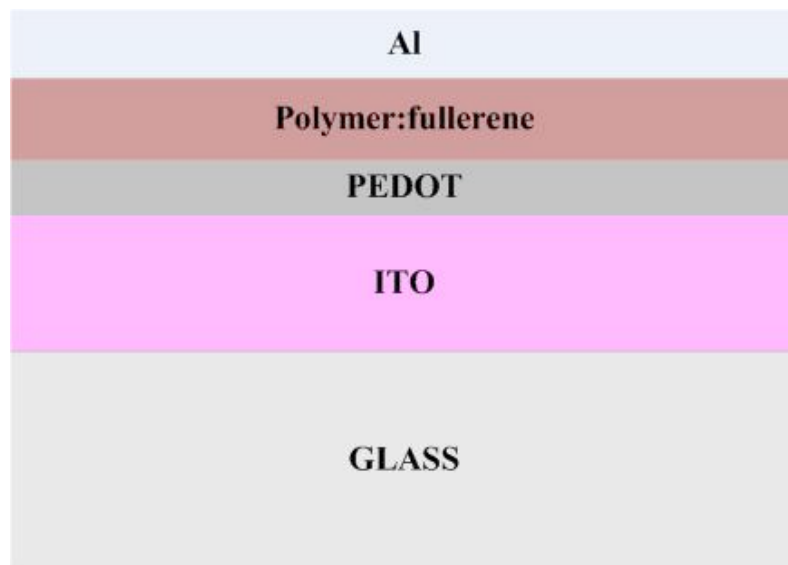


Figure 2-1. A typical BHJ solar cell structure, which consists of an anode (Indium Tin Oxide (ITO)) layer, a Poly(3,4-ethylenedioxythiophene) poly(styrenesulfonate) (PEDOT) layer, a polymer:fullerene layer and a cathode (Al) layer.

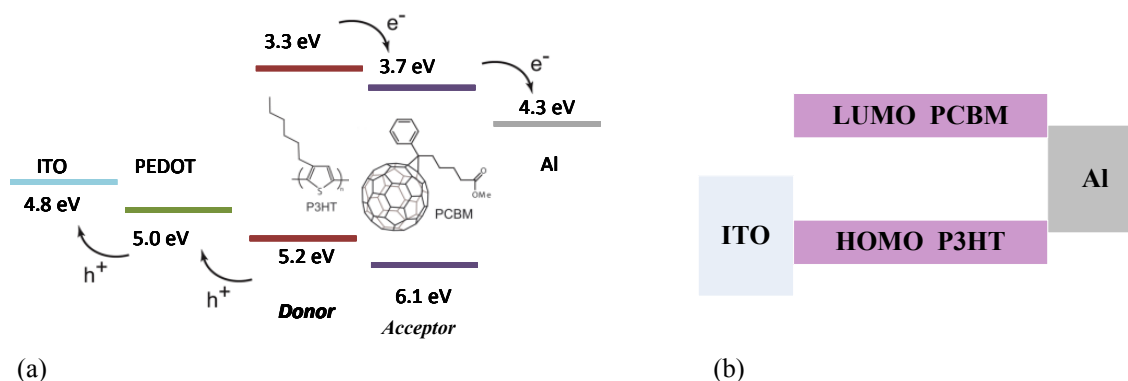


Figure 2-2. (a) Schematic of the energy levels (b) Device model in flat band condition for a poly(3-hexylthiophene) (P3HT): phenyl-C61-butyric acid methyl ester (PC₆₁BM).

A typical BHJ solar cell structure is shown in Fig. 2-1. It can be described as a MIM (metal-insulator-metal) structure (Fig. 2-2) [30]. The metals are represented by their Fermi levels, whereas the valence and conduction bands of the semiconductor correspond to the lowest unoccupied molecular orbital (LUMO) level of the acceptor and highest occupied molecular orbital (HOMO) level of the donor.

2.1.2 Basic equations

The basic equations [30] used in this model are the Poisson equation

$$\frac{\partial^2 \psi(x)}{\partial x^2} = \frac{q}{\epsilon_0 \epsilon_r} [n(x) - p(x)], \quad (2-1)$$

where q is the elementary charge, ϵ_0 is permittivity of free space, ϵ_r is relative permittivity, $\psi(x)$ is the potential and $n(x)$, $p(x)$ are the negative and positive free polaron densities, respectively. The current continuity equations can be written as

$$\frac{\partial}{\partial x} J_n(x) = q U_n(x), \quad (2-2a)$$

$$\frac{\partial}{\partial x} J_p(x) = -q U_p(x), \quad (2-2b)$$

where $J_{n(p)}(x)$ is the negative(positive) free polaron current density and $U_{n(p)}(x)$ is the negative(positive) free polaron net generation rate.

In order to solve the above equations, a set of current density equations are given below

$$J = J_p + J_n, \quad (2-3)$$

$$J_p = -q \mu_p p E - q D_p \frac{dp}{dx}, \quad (2-4a)$$

$$J_n = -q \mu_n n E + q D_n \frac{dn}{dx}, \quad (2-4b)$$

where $D_{n,p}$ are the carrier diffusion coefficients and $\mu_{n,p}$ are the carrier mobilities.

2.1.3 Generation and recombination

The charge generation and recombination process is shown in Fig. 2-3. As we described in the chapter 1, the excitons are first generated when photons are absorbed. Some of excitons will diffuse to the donor-acceptor interface and become a polaron pair. The bound polaron pair will either decay to the ground state with a decay rate k_f or dissociate into free polarons with a dissociation rate k_{diss} . The dissociation probability is $P_{diss}=k_{diss}/(k_{diss}+k_f)$. The free polarons will either be collected or reform polaron pairs. [30]

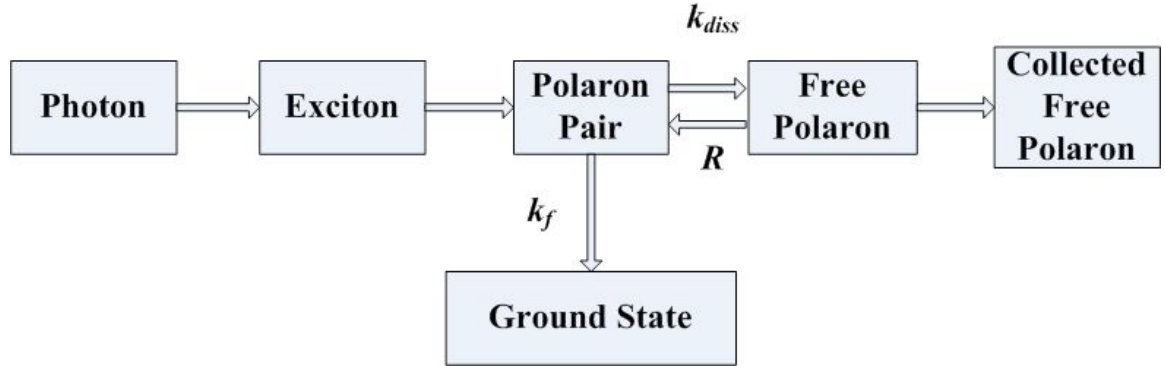


Figure 2-3. The charge generation and recombination process.

From the process above, the continuity equations for polaron pair and positive polaron are written as

$$\frac{dX}{dt} = G_{pp} - k_f X - k_{diss} X + R, \quad (2-5a)$$

$$\frac{dn}{dt} = \frac{1}{q} \frac{\partial}{\partial x} J_n + k_{diss} X - R, \quad (2-5b)$$

where $X(\text{cm}^{-3})$ is the concentration of polaron pair, $n(\text{cm}^{-3})$ is the concentration of positive polaron, G_{PP} is the polaron pair generation rate, which is related to photon absorption and exciton diffusion and R is the free polaron recombination rate.

2.1.4 Boundary conditions

In order to solve Eq. 2-1 – Eq. 2-4, it is necessary to specify the carrier densities and potential at both contacts as follows

$$n(0) = N_{LUMO}, \quad (2-6a)$$

$$p(0) = N_{LUMO} \exp\left(-\frac{\Delta E_{HL}}{kT/q}\right), \quad (2-6b)$$

$$p(d) = N_{HOMO}, \quad (2-6c)$$

$$n(d) = N_{HOMO} \exp\left(-\frac{\Delta E_{HL}}{kT/q}\right), \quad (2-6d)$$

$$\psi(d) - \psi(0) = \Delta E_{HL} - V_a, \quad (2-7)$$

where N_{LUMO} and N_{HOMO} are the effective density of states of the donor HOMO level and acceptor LUMO level, respectively. ΔE_{HL} is the energy difference between the HOMO energy of the donor and the LUMO energy of the acceptor. k is Boltzmann's constant and V_a is the applied voltage

2.2 Fabrication of organic BHJ solar cells

Polymer choice

Recently, Thompson et al. demonstrated a new class of low bandgap donor-acceptor poly(3-hexylthiophene) (P3HT) based semi-random polymers with broad and intense absorption profiles and PCE approaching 6% [30-33]. As they are shown in Fig.2-4, the incorporation of a small percentage of acceptor units into the polymer backbone is

observed to significantly decrease the optical bandgap, which results in strong absorption from the visible to the near infrared but at the same time important properties of P3HT such as semicrystallinity and high hole mobility are retained.[31] Although all of these polymers exhibit strong and broad absorption of the photon flux, the measured short-circuit current densities of optimized polymer:fullerene BHJ solar cells exhibit a wide range of values from 1.5 to 16.5 mA/cm².

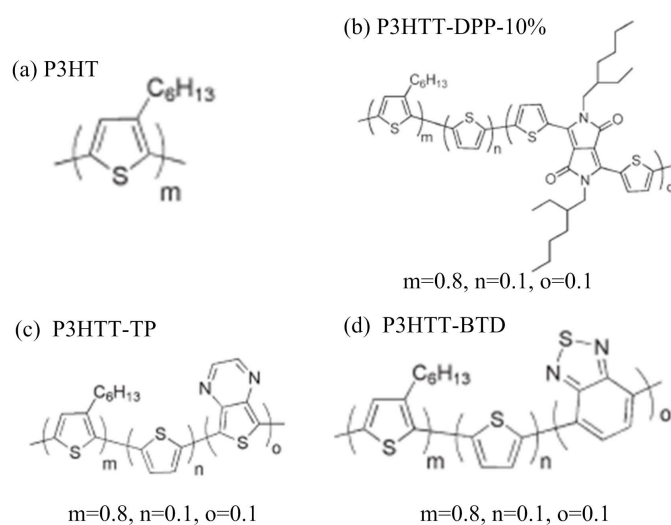


Figure 2-4. Structures of P3HT, P3HTT-DPP-10%, P3HTT-TP and P3HTT-BTD polymers

Table 2-1. Photovoltaic properties of P3HT, P3HTT-DPP-10%, P3HTT-TP and P3HTT-BTD with PC₆₁BM as an acceptor.

	Thickness	J_{sc}	V_{oc}	FF	PCE
	(nm) ^a	(mA/cm ²) ^b	(V)		(%)
P3HT:PC ₆₁ BM	85	8.07	0.577	0.58	2.70
P3HTT-DPP-10%:PC ₆₁ BM	100	9.99	0.579	0.54	3.14
P3HTT-TP:PC ₆₁ BM	64	1.90	0.373	0.33	0.24
P3HTT-BTD:PC ₆₁ BM	180	2.27	0.566	0.36	0.46

^a Measured by profilometer. ^b Not mismatch corrected.

In particular, benzothiadiazole (BTD) and thienopyrazine (TP) based polymers (P3HTT-BTD and P3HTT-TP) have significantly lower short-circuit current densities (J_{sc}) than P3HT and poly(3-hexylthiophene–thiophene–diketopyrrolopyrrole (P3HTT-DPP-10%) in BHJ solar cells, as shown in Table 2-1. It is of great interest and importance to understand the origin of such drastic performance differences in order to establish future design strategies for efficient semi-random copolymers.

Fabrication of organic BHJ solar cells

The structure of a typical BHJ solar cell is shown in Fig.2-1. BHJ solar cells in a conventional device configuration ITO(280nm)/PEDOT:PSS(40nm)/polymer:PC₆₁BM/Al(100nm) were fabricated in air. Here, four different polymers that were synthesized by University of Southern California Barry C. Thompson group were used. The polymers are P3HT, poly(3-hexylthiophene–thiophene–diketopyrrolopyrrole (P3HTT-DPP-10%), benzothiadiazole (BTD) and thienopyrazine (TP) based polymers (P3HTT-BTD and P3HTT-TP). [31, 32]

The P3HT: PC₆₁BM devices were prepared using the following procedure: P3HT and PC₆₁BM (American Dye Source Inc. supplier) were dissolved and stirred separately in chlorobenzene overnight. Then, when fully dissolved, the two solutions were mixed forming a 55:45 (P3HT:PCBM) wt% solution at a concentration of 10 mg/ml for P3HT and 8.18 mg/ml for PCBM. ITO-coated glass substrates were first cleaned with acetone and isopropyl alcohol and subsequently air-dried. A 40 nm-thick, highly-conductive Poly(3,4-ethylenedioxythiophene):poly(styrenesulfonate) (PEDOT:PSS) (H. C Starck supplier) layer was then spin-coated on the ITO-coated glass substrate. After baking the PEDOT:PSS under vacuum at 120° for 50 minutes, spin-casting was used to deposit the

blend solution. Then a 100 nm Al layer was deposited as the top electrode using a thermal evaporation deposition system. Finally, the sample was annealed in vacuum for 30 minutes.

For P3HTT-DPP-10%: PC₆₁BM solar cells, separate solutions of P3HTT-DPP-10% and PC₆₁BM were prepared in dichlorobenzene solvent. The solutions were stirred for 24 hours at 50-70 °C to form a homogeneous mixture. Mixture solution in dichlorobenzene containing 10mg/ml P3HTT-DPP-10% and 13.5mg/ml PC₆₁BM was then stirred at 50-70 °C for at least 12 hours. After that, P3HTT-DPP-10%: PC₆₁BM was spin cast from the mixture solution on the 40nm PEDOT coated ITO glass. After placing the devices in the nitrogen cabinet for 20 minutes, the devices were placed in the thermal evaporator and a 100nm Al layer was deposited. No thermal annealing following fabrication is required.

For P3HTT-TP:PC₆₁BM and P3HTT-BTD:PC₆₁BM solar cells, separate solutions of polymer and PC₆₁BM were prepared in dichlorobenzene solvent. The solutions were stirred for 24 hours at 70-90 °C to form a homogeneous mixture. Mixture solutions in the desire ratios were then stirred at 70-90 °C for at least 12 hours. After that, the P3HTT-TP: PC₆₁BM layer was spin cast from a solution in dichlorobenzene containing 7mg/ml P3HTT-TP and 5.53mg/ml PC₆₁BM on the 40nm PEDOT coated ITO glass. The P3HTT-BTD: PC₆₁BM layer was spin cast from a solution in dichlorobenzene containing 7mg/ml P3HTT-BTD and 35mg/ml PC₆₁BM on the 40nm PEDOT coated ITO glass. Then the devices were placed in the vacuum cabinet for 30 minutes at 100 °C and cooled down to the room temperature prior to electrode deposition. At the final stage, a 100nm Al layer is deposited. No thermal annealing is carried out for P3HTT-TP: PC₆₁BM, while 10mins 100 °C thermal annealing under vacuum is needed for P3HTT-BTD: PC₆₁BM solar cells.

Encapsulation of organic BHJ solar cells

It is well known that the organic based solar cells degrade very fast under normal environmental conditions. This is due to their limited resistance to oxygen, moisture, elevated temperatures and light [33-36]. Since it takes at least five days to finish all the experimental characterization, it becomes very important to encapsulate the solar cells after the fabrication.

The encapsulation procedure is shown in Fig. 2-5. On the top of the aluminum contact, an ultraviolet (UV) cured epoxy (DELO-Katiobond LP655) layer is applied first. The reason why we choose this product is because this UV cured epoxy is demonstrated to be flexible and transparent enough to protect the sensitive chemicals in the devices from humidity and oxygen [37]. After the epoxy is applied, a 0.9mm-thick cover glass is put on the epoxy to further isolate the air. At last, the device is cured in a UV lamp with $50\text{mW}/\text{cm}^2$ intensity for 10mins.

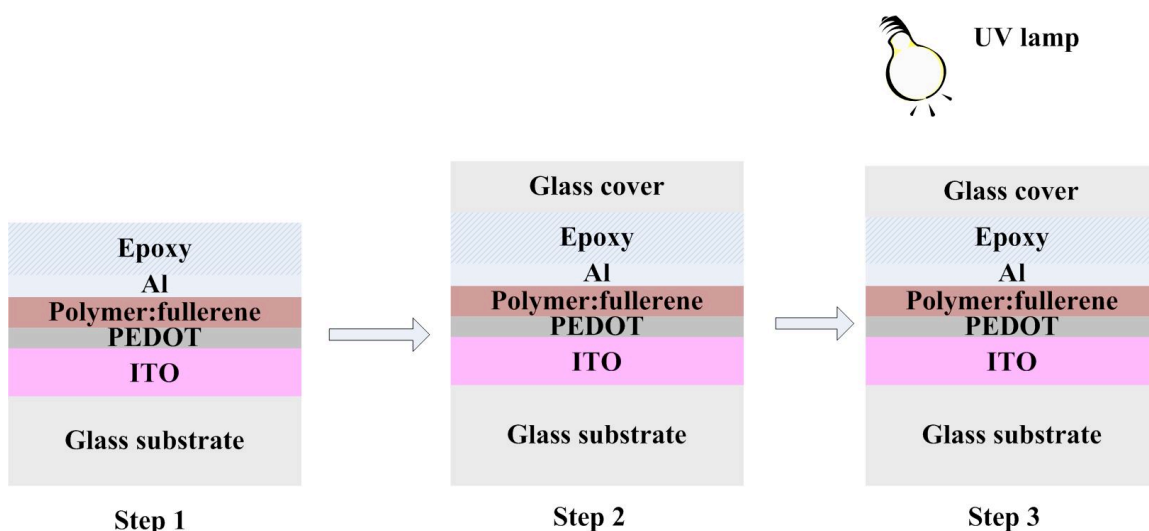


Figure 2-5. Encapsulation procedure for solar cells.

2.3 Characterization of organic BHJ solar cells

2.3.1 Refractive index measurement

The complex refractive index $n = \eta + i\kappa$ is usually measured by variable angle spectroscopic ellipsometry. Here, η is the dielectric constant, indicating the phase speed of the light in a material. κ is the extinction coefficient, revealing the amount of absorption loss when the electromagnetic wave propagates through the material. Since a single measurement is insufficient to measure thickness and both components of n , multiple angle-of-incidence and multiple-wavelength measurements are performed. For BHJ films, the fitting of the spectroscopic ellipsometry data is difficult because numerous numerical assumptions are necessary and optical birefringence must be accounted for. Ellipsometric fitting techniques fail for thin films with strong absorption and high surface roughness [38].

In order to overcome these difficulties, a Pekin Elmer Lambda 950 UV/VIS spectrometer is used to extract the refractive index. A thin film blend is first spin coated on a glass. Then the film thickness is measured with a Dektak Stylus Profiler. After that, the transmission and reflection of the film on glass and the glass are characterized by the spectrometer. By knowing the thickness, transmission and reflection, the refractive index is finally extracted by the transfer-matrix-theory [39], which will be discussed in Chapter 3.

2.3.2 Current-voltage and capacitance-voltage measurements

The current-voltage characterization of the device consists of a dark current measurement, an AM1.5 photocurrent measurement, a transient photocurrent

measurement, and a forward-to-zero transient current response measurement. The dark current of a solar cell is the current when a voltage is applied in the absence of light. The AM1.5 photocurrent of a solar cell is the current when a voltage is applied under the standard AM1.5 solar spectrum. Both were measured with a Keithley source meter and an ORIEL Sol1A solar simulator using the four-terminal sensing method. The dark and photocurrents are useful to determine the efficiency of the solar cells, as well as other characteristics such as recombination and breakdown. In order to analyze the breakdown mechanisms, a Janis Model ST-100-FTIR low-temperature probe station is used to measure dark current and photocurrent in different temperatures. This probe station has three windows that allow the light to shine on the devices. The transient photocurrent measurement and the forward-to-zero transient current response measurement were used to characterize the free polaron recombination lifetime, which will be discussed in chapter 6.

The capacitance-voltage is measured with an HP 4275A multi-frequency LCR meter. The open-circuit and short-circuit calibrations are performed prior to the measurements of the solar cells. The capacitance-voltage measurement is used to extract the dielectric constant of the blend.

2.3.3 External quantum efficiency measurements

The external quantum efficiency (EQE) is the ratio of the number of free carriers collected to the number of photons incident on the solar cell. It indicates the amount of current that the cell will produce when irradiated by photons at a specific wavelength. The EQE is measured using a 1kW Xenon arc lamp, a monochromator, a chopper, a lock-in amplifier and a reference silicon photodiode. The lock-in amplifier measures the

photocurrent of the device. The photocurrent response of the calibrated silicon photodiode to the same light source is also measured. To calculate the external quantum efficiency of the device the ratio of the device photoresponse to that of the calibrated sensor is multiplied by the known external quantum efficiency of the silicon reference.

2.3.4 Mobility measurements

The transport of free polarons in organic semiconductors is realized by a hopping transport mechanism. The Marcus model[40, 41] and the Miller-Abrahams[42] model provide insight into how to calculate the hopping rates and macroscopic properties of charge transport in such disordered systems. The theoretical value of charge mobility can be derived by Monte Carlo simulations[43] or hopping master equations[44]. Charge mobilities can also be determined by various experimental techniques, such as time of flight (TOF)[41-43], space charge limited current (SCLC)[45-47], and source-drain current versus gate voltage in field effect transistors (FETs)[48, 49]. Several factors, such as molecular packing, temperature, and electric field influence the charge mobility as well.[50, 51]

In this dissertation, SCLC is utilized to measure the hole and electron mobilities. To fabricate “hole-only” devices, palladium was evaporated as the top contact for an ITO/PEDOT:PSS/ P3HT:PCBM structure.[46] For “electron-only” devices, in order to suppress hole injection in P3HT, a 1nm LiF/80nm Al layer was used as both top and bottom contacts. The 1nm LiF layer enables the work function of Al to be lowered to 2.8 eV[52]. For the electron only and hole only devices, the SCL current is approximated by[50]

$$J = \frac{9}{8} \varepsilon_0 \varepsilon_r \mu_0 \frac{V_a^2}{d^3}, \quad (2-8)$$

where J is the current density; ε_0 is the permittivity of free space; ε_r is the relative permittivity of the material; μ_0 is the zero-field mobility; V is the applied voltage; and d is the thickness of the active layer.

Chapter 3. Photon absorption and exciton generation

3.1 Introduction

When photons with energy above the absorption edge are incident on the cells, some of them will be absorbed. Usually, the absorption band of polymers is not as broad as that of inorganic semiconductors because of their relatively narrow energy bands. Therefore, the so-called donor-acceptor approach[53, 54] and donor-acceptor copolymer[31, 32] are often used to broaden the spectral absorption. However, the spectral absorption is still not as broad as that in silicon, which is illustrated in Fig.3-1. It is clear that absorption is still one of the primary challenges to achieve higher efficiency. Therefore, it is important to know the absorption of organic BHJ solar cells.

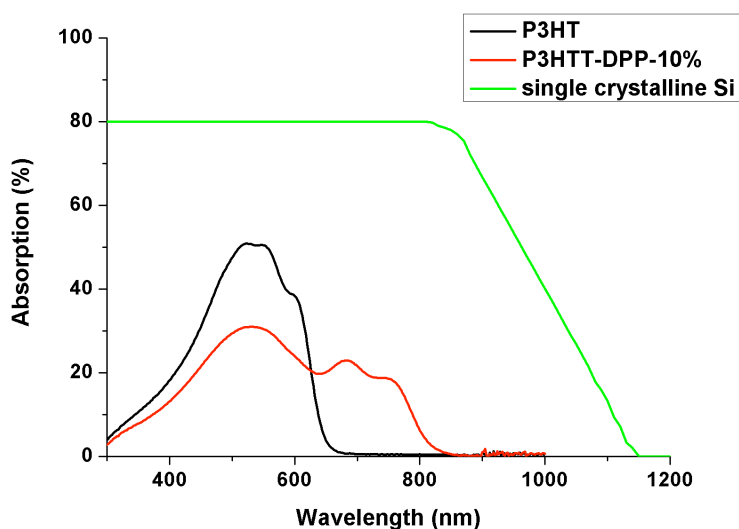


Figure 3-1. Absorption of poly (3-hexylthiophene) (P3HT), which is a typical semiconducting polymer, and poly (3-hexylthiophene-thiophene-diketopyrrolopyrrole-10%) (P3HTT-DPP-10%), a donor-acceptor copolymer, and single crystalline silicon.

The absorption of a thick layer of material is usually calculated by transmission and reflection, which are measured with a spectrometer. However, for a BHJ solar cell, there are additional considerations. As shown in Fig. 3-2, a BHJ solar cell consists of several thin film layers having dimensions on the order of the wavelength of light; therefore the effect of optical interference cannot be ignored. Here, we apply the optical transfer-matrix-theory model[39] on organic BHJ solar cells to get the optical electrical field and absorption at a single wavelength. Then, the total absorption percentages for AM1.5 global photon flux are calculated by integration.

3.2 Multi-layer thin-film interference model

The optical transfer-matrix-theory was first introduced by Heavens[39] and was recently applied to organic BHJ solar cells.[55-57]

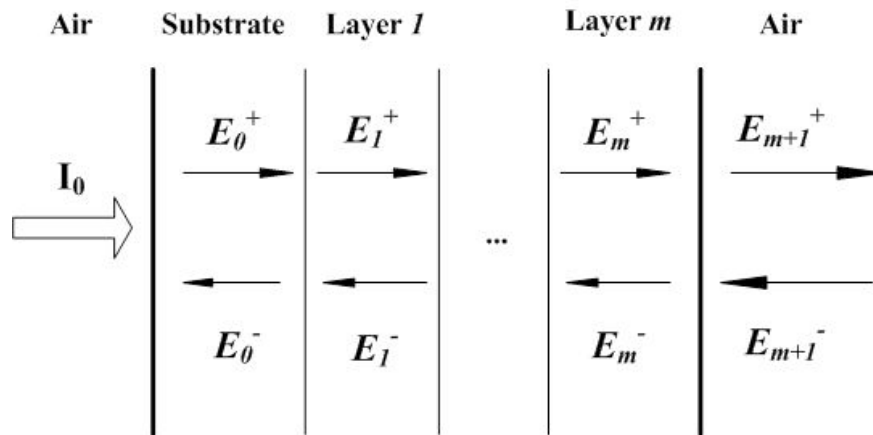


Figure 3-2. The solar cell consists of a stack of m thin-film layers. Light is incident on the substrate from the left, with intensity I_0 and travels to the right. Each layer j ($j=1, 2, \dots, m$) has a thickness d_j . The optical electric field inside each layer is described as E^+ for waves traveling from left to right and E^- for waves traveling from right to left.

As shown in Fig. 3-2, the device consists of a transparent substrate and a stack of m thin-film layers, each of which is described by its complex refractive index $n = \eta + i\kappa$ and

thickness d . A matrix that characterizes the interface between layer j and k can be written as

$$I_{jk} = \begin{bmatrix} (n_j + n_k) / 2n_j & (n_j - n_k) / 2n_j \\ (n_j - n_k) / 2n_j & (n_j + n_k) / 2n_j \end{bmatrix} . \quad (3-1)$$

Similarly, the layer matrix characterizing the propagation through layer j is described by

$$L_j = \begin{bmatrix} e^{-i\xi_j d_j} & 0 \\ 0 & e^{i\xi_j d_j} \end{bmatrix}, \quad (3-2)$$

where $\xi_j = 2\pi n_j / \lambda$ and λ is the wavelength. Therefore, the optical electric field for the total system can be written as

$$\begin{bmatrix} E_0^+ \\ E_0^- \end{bmatrix} = S \begin{bmatrix} E_{m+1}^+ \\ E_{m+1}^- \end{bmatrix}, \quad (3-3)$$

where S , the total transfer matrix, can be expressed as

$$S = \begin{bmatrix} S_{11} & S_{12} \\ S_{21} & S_{22} \end{bmatrix} = \left(\prod_{v=1}^m I_{(v-1)v} L_v \right) \cdot I_{m(m+1)} . \quad (3-4a)$$

In order to calculate the optical electric field in layer j , S can be divided into two subsets,

$$\begin{aligned} S &= S'_j L_j S''_j \\ &= \begin{bmatrix} S'_{j11} & S'_{j12} \\ S'_{j21} & S'_{j22} \end{bmatrix} L_j \begin{bmatrix} S''_{j11} & S''_{j12} \\ S''_{j21} & S''_{j22} \end{bmatrix} . \end{aligned} \quad (3-4b)$$

Next, we need to define complex reflection and transmission coefficients for layer j in terms of the matrix elements.

$$\begin{aligned} r'_j &= \frac{S'_{j21}}{S'_{j11}}, & t'_j &= \frac{1}{S'_{j11}}, \\ r''_j &= \frac{S''_{j21}}{S''_{j11}}, & t''_j &= \frac{1}{S''_{j11}}. \end{aligned} \quad (3-5)$$

Combining Eqs. 3-4 and 3-5, we obtain

$$t_j^+ = \frac{E_j^+}{E_0^+} = \frac{t_j'}{1 - r_j' - r_j'' e^{i2\xi_j d_j}},$$

$$t_j^- = \frac{E_j^-}{E_0^+} = t_j^+ r_j'' e^{i2\xi_j d_j}.$$
(3-6)

Therefore the total optical electric field in layer j is given by

$$E_j(x) = E_j^+(x) + E_j^-(x) = t_j^+ [e^{i\xi_j x} + r_j'' e^{i\xi_j (2d_j - x)}] E_0^+.$$
(3-7)

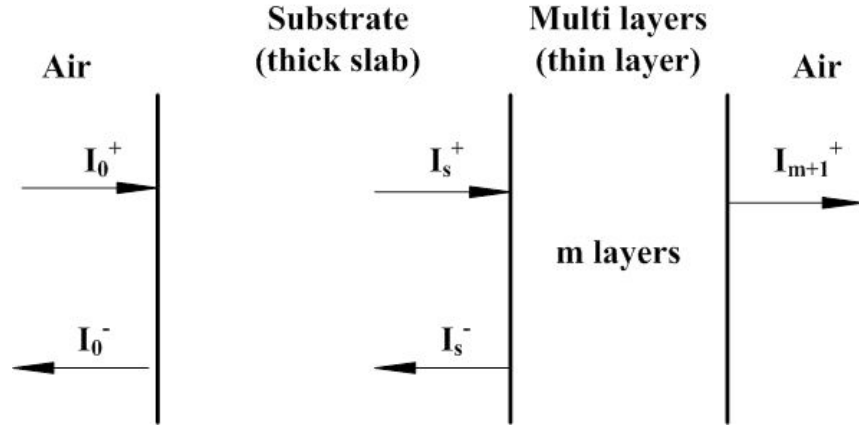


Figure 3-3. The whole structure considering the substrate.

Now, consider the substrate effect. The whole structure can be seen as a thick slab and a thin film, as shown in Fig.3-3. The transmission of the films on glass is

$$T = \frac{I_{m+1}^+}{I_0^+} = \frac{I_{m+1}^+}{I_s^+} \frac{I_s^+}{I_0^+}$$

$$= \frac{\eta_{m+1}}{\eta_0} |t_{m+1}^+|^2 \Re(T_s e^{-\alpha_s d_s} + T_s e^{-\alpha_s d_s} R_m R_s + \dots T_s e^{-\alpha_s d_s} R_m^n R_s^n) \quad , \quad (3-8a)$$

$$= \frac{\eta_{m+1}}{\eta_0} |t_{m+1}^+|^2 \Re\left(\frac{T_s e^{-\alpha_s d_s}}{1 - R_m R_s e^{-2\alpha_s d_s}}\right)$$

where R is the reflectance of the multilayer stack t_j^- ; R_s and T_s are the reflectance and transmittance of the substrate; and α_s is the absorption coefficient of the substrate; and the reflection of the films on glass is

$$R = \frac{I_0^-}{I_0^+} = T_s^2 e^{-2\alpha_s d_s} R_m + T_s^2 e^{-2\alpha_s d_s} R_m^2 R_s + \dots T_s^2 e^{-2\alpha_s d_s} R_m^{n+1} R_s^n$$

$$= \frac{T_s^2 e^{-2\alpha_s d_s} R_m}{1 - R_m R_s e^{-2\alpha_s d_s}} \quad , \quad (3-8b)$$

Therefore, the intensity of light incident on the interface between the substrate and the multilayer structure, I_s , can be calculated based on [55, 58], which is expressed as

$$I_s^+ = I_0 \frac{T_s e^{-\alpha_s d_s}}{1 - R_m R_s e^{-2\alpha_s d_s}} = I_0 T_{\text{int}} \quad (3-8c)$$

By combining Eq. 3-7 and Eq. 3-8, the light intensity at a distance x within layer j can be expressed as

$$I_j(x) = \frac{1}{2} c \epsilon_0 \eta_j |E_j|^2$$

$$= \frac{1}{2} c \epsilon_0 \eta_j \left| t_j^+ [e^{i\xi_j x} + r_j'' e^{i\xi_j (2d_j - x)}] E_0^+ \right|^2$$

$$= \frac{\eta_j}{\eta_s} I_s^2 \left| t_j^+ [e^{i\xi_j x} + r_j'' e^{i\xi_j (2d_j - x)}] \right|^2 \quad , \quad (3-9)$$

$$= \frac{\eta_j}{\eta_s} I_0 T_{\text{int}}^2 \left| t_j^+ \right|^2 \{ e^{-\alpha_j x} + \rho_j''^2 e^{-\alpha_j (2d_j - x)} + 2\rho_j'' e^{-\alpha_j d_j} \cos[4\pi n_j (d_j - x) / \lambda + \delta_j''] \}$$

where $n_s = \eta_s + i\kappa_s$ is the refractive index of the substrate, ρ_j'' and δ_j'' are the argument and the phase of r_j'' , and $\alpha_j = 4\pi\kappa_j/\lambda$ is the absorption coefficient. Then the absorption intensity I_a and absorption efficiency η_a in layer j are described as

$$I_a = \int_j \alpha_j I_j(x) dx \quad , \quad (3-10)$$

and

$$\eta_a = \frac{\int \alpha_j I_j(x) dx}{I_0} . \quad (3-11)$$

3.3 Refractive index

Table 3-1. Photovoltaic properties and absorption efficiency of P3HT, P3HTT-DPP-10%, P3HTT-TP and P3HTT-BTD with PC₆₁BM as an acceptor.

	Thickness (nm) ^a	η_a (%) at 630nm	η (%) for AM1.5	J_{sc} (mA/cm ²) ^d	PCE (%)
P3HT:PC ₆₁ BM	85	10.8	11	8.07	2.70
P3HTT-DPP-10%:PC ₆₁ BM	100	51.0	18	9.99	3.14
P3HTT-TP:PC ₆₁ BM	64	35.9	16	1.90	0.24
P3HTT-BTD:PC ₆₁ BM	180	43.6	13	2.27	0.46

^a Measured by profilometer. ^b Not mismatch corrected

In order to determine the absorption, the refractive index is first extracted by a simplified optical matrix-transfer-theory model with the substrate and a one layer film. As explained in chapter 2.3.1, the absorption and reflection of the glass and blend on glass were measured. The thicknesses of the layers are shown in Table 3-1. Using Eqs. 3-8a and 3-8b, a system of nonlinear equations with two variables blend refractive index η and κ is established, which it's shown as

$$T_{measure}(\lambda) = T_{calculated}(\eta, \kappa, \lambda) , \quad (3-12a)$$

$$R_{measure}(\lambda) = R_{calculated}(\eta, \kappa, \lambda) , \quad (3-12b)$$

where $T_{measure}$ and $R_{measure}$ are the measured transmission and reflection of the films on glass, respectively. $T_{calculated}$ and $R_{calculated}$ are the calculated transmission and reflection

from Eq. 3-8a and Eq. 3-8b. By solving the equations by using MATLAB, the refracted index components η and κ as a function of the wavelength were extracted, as shown in Fig. 3-4.

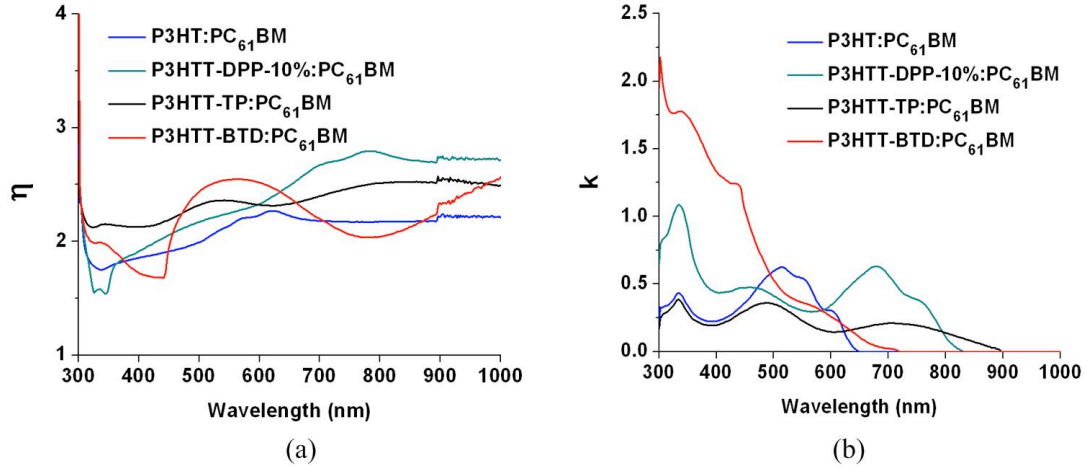


Figure 3-4. (a) Refractive index η and (b) Extinction coefficient κ of four polymer:PC₆₁BM thin films.

3.4 Optical electrical field profile

After obtaining the refractive index, the optical electric field profile is calculated based on Eq. 3-7. Plots of electric field profiles for the four types of cells studied in this work are shown in Fig. 3-5. In Fig. 3-5, regions I, II, III and VI represent 280nm ITO layer, 40nm PEDOT:PSS layer, active layer (polymer: PC₆₁BM) and 100nm Al layer, respectively. As expected, the optical electrical field exhibits spatial peaks and nulls rather than a simple exponential decay in the active layer. The light interference is so strong in this multi-thin-layer structure that the Fabry-Perot cavity effect cannot be neglected. The Al layer reflects light back to the active layer to enhance absorption. Fig. 3-4 only shows the optical electrical field at 630nm. I have also simulated the optical

electrical field at other wavelength from 280nm to 1000nm with 2nm step for all four types of solar cells.

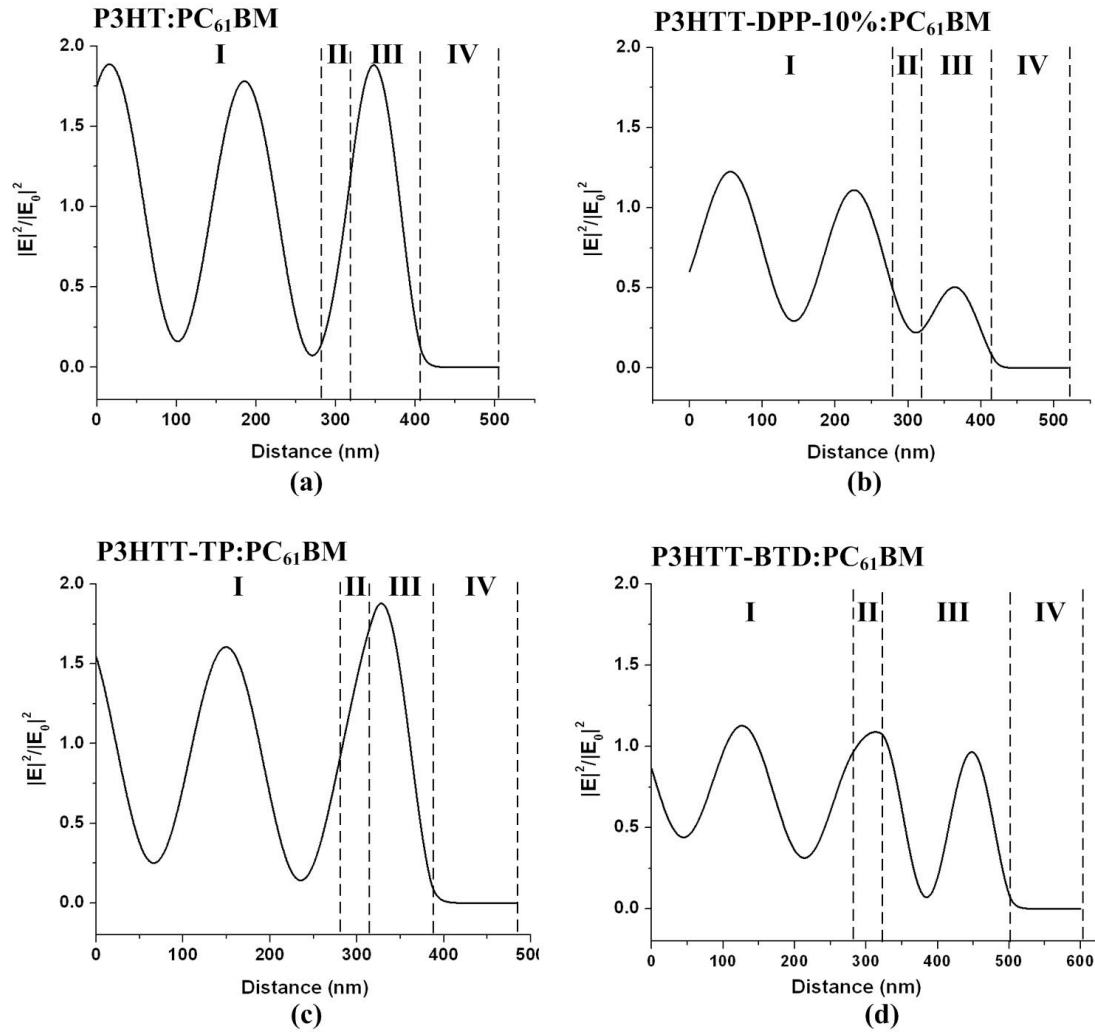


Figure 3-5. Optical electrical field inside the (a) P3HT:PC₆₁BM, (b)P3HTT-DPP-10%:PC₆₁BM, (c) P3HTT-TP:PC₆₁BM and (d) P3HTT-BTD:PC₆₁BM solar cells at 630nm. In this figure, region I, II, III and VI represent 280nm ITO layer, 40nm PEDOT:PSS layer, active layer (polymer: PC₆₁BM) and 100nm Al layer, respectively.

3.5 Total absorption of AM1.5

Based on the optical electric field intensity inside the active layer, the full spectrum absorption or the photon absorption percentage η_a at each wavelength was calculated using Eq. 3-11 and is depicted in Fig. 3-6.

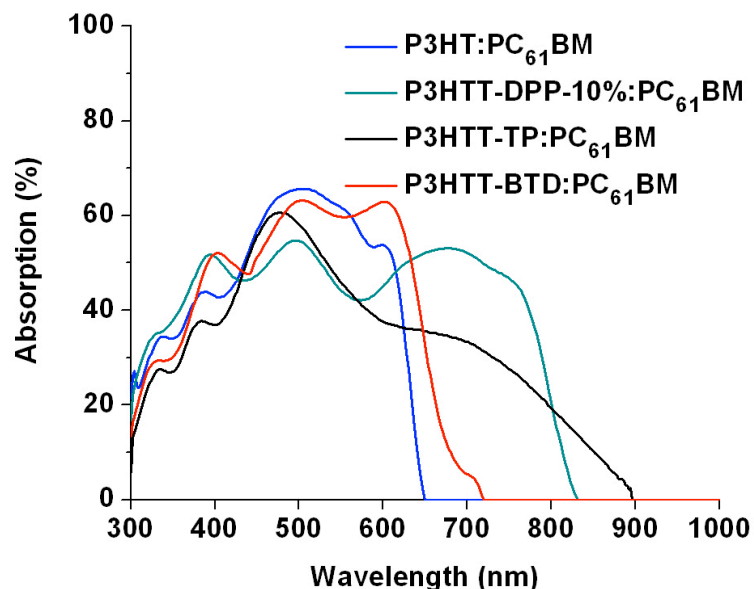


Figure 3-6. Absorption of four polymer: PC₆₁BM thin films.

As can be seen, the other three semi-random polymer:PC₆₁BM thin films exhibit significantly broader absorption spectra compared to P3HT:PC₆₁BM. P3HTT-DPP-10%:PC₆₁BM and P3HTT-TP:PC₆₁BM blends exhibit two peaks, while P3HT:PC₆₁BM and P3HTT-BTD:PC₆₁BM have only one peak. The short-wavelength band (~ 500 nm) is due to π - π^* transitions and the long-wavelength band (~ 700 nm) is attributed to intramolecular charge transfer (ICT).[59] The peak near 350 nm is a result of the PC₆₁BM absorption.[32] Also, vibronic shoulders at 600 and 750 nm are present in the P3HT:PC₆₁BM and P3HTT-DPP-10%:PC₆₁BM films, which is a general indication of

interchain vibrational absorption induced by a high degree of ordering and strong interchain interactions.[60] No vibronic shoulders are present in the P3HTT-TP:PC₆₁BM and P3HTT-BTD:PC₆₁BM thin films possibly indicating a less ordered nature of the films.

The total absorption percentages of AM1.5 global photon flux is calculated based on the equation $\eta = \frac{\int \eta_a(\lambda) N(\lambda) d\lambda}{\int N(\lambda) d\lambda}$, where $N = R / (hc / \lambda)$ is the number of photons per second at λ , $R(W/m^2/nm)$ is AM1.5 spectral irradiance at λ , and η_a is the photon absorption percentage at λ . By integrating the number of photons at each wavelength, the total absorption percentages of global photon flux are calculated to be $\sim 11\%$, 18% , 16% and 13% for P3HT:PC₆₁BM, P3HTT-DPP-10%:PC₆₁BM, P3HTT-TP:PC₆₁BM and P3HTT-BTD:PC₆₁BM, respectively. All the important numbers are listed in Table 3-1.

3.6 Exciton generation

After photons are absorbed, strongly Coulomb-bound electron-hole pairs are created in singlet exciton states. Unlike in inorganic semiconductors, the exciton binding energy in conjugated polymers is high, so the thermal energy at room temperature is not sufficient to dissociate the excitons into free charge carriers. Therefore, they need to diffuse to a donor/acceptor interface where the interface enables dissociation. [15, 16] In this study, we assume 100% of the absorbed photons will give rise to excitons

Chapter 4. Exciton diffusion

4.1 Introduction

After excitons are generated, they need to diffuse to the donor-acceptor interface in order to get sufficient energy to dissociate. However, excitons only diffuse a short distance before they recombine. It follows that the domains should ideally be comparable to the diffusion length in order to maximize the number of excitons that reach the interface [61]. Spectrally resolved photoluminescence quenching (SR-PLQ) is a convenient and accurate method to measure the exciton diffusion length of organic materials used for solar cells [62]. Experimentally, the exciton diffusion length for donor polymers is ~ 5 - 15 nm [61, 63, 64] and ~ 40 nm for acceptor fullerene C_{60} [65], while another typical acceptor $PC_{61}BM$, has an exciton diffusion length of only 5 nm [66]. The domain size of donor and acceptor material is typically determined by the solution concentration, spin coating speed and thermal annealing temperature [67-69]. However, for some polymers such as $PC_{61}BM$ the diffusion length is so short it is difficult to achieve a good match to the dimension of the domains. Therefore, it is important to know the exciton diffusion efficiency for the materials used in BHJ solar cells.

Exciton diffusion efficiency η_{ed} is defined as the ratio of the number of excitons that diffuse to the donor/acceptor interface to the number of excitons generated inside the cells. In this chapter, exciton diffusion efficiency is investigated using current density versus voltage (J - V) measurements at large reverse bias. The efficiencies for four polymers combined with $PC_{61}BM$ are listed and compared. Under high reverse bias, the current exhibits a significant decrease for fields greater than $E=6 \times 10^7$ V/m, which is

contrary to the voltage independent behavior predicted by the Onsager-Braun model[70]. The current drop is analyzed in terms of the breakdown mechanisms, and the tunneling effect is found to be the dominate breakdown mechanism in most devices.

4.2 Theory: determine the exciton diffusion efficiency by measuring J-V curves

As discussed in Chapter 2, the exciton diffusion efficiency can be determined using the exciton and free polaron continuity equations, which can be written as

$$\frac{dX}{dt} = G_{PP} - k_f X - k_{diss} X + R, \quad (2-5a)$$

and

$$\frac{dn}{dt} = \frac{1}{q} \frac{\partial}{\partial x} J_n + k_{diss} X - R. \quad (2-5b)$$

Recall that $X(\text{cm}^{-3})$ is the concentration of polaron pair, $n(\text{cm}^{-3})$ is the concentration of positive polaron, G_{PP} is the polaron pair generation rate, which is related to photon absorption and exciton diffusion and R is the free polaron recombination rate. Under the equilibrium condition, $dX/dt=0$ and $dn/dt=0$, which yields

$$G_{PP} - k_f X = k_{diss} X - R, \quad (4-1a)$$

and

$$\frac{1}{q} \frac{\partial}{\partial x} J_n = -k_{diss} X + R. \quad (4-1b)$$

As stated in Chapter 2, $k_{diss}=[P_{diss}/(1-P_{diss})]k_f$. Then, Eq. 4-1b becomes

$$\begin{aligned} \frac{1}{q} \frac{\partial}{\partial x} J_n &= (1 - P_{diss})R - P_{diss} G_{PP} \\ &= (1 - P_{diss})R - P_{diss} \eta_{ed} G_{exciton} \end{aligned} \quad (4-1c)$$

where $G_{exciton}$ is the exciton generation rate, which is equal to the photon absorption rate under the assumption that all the absorbed photons create excitons. Here, we also assume η_{ed} is the average exciton diffusion efficiency, which is independent of the depth x inside the active layer.

The electric field inside an organic BHJ solar cell can be approximated as

$$E = |V_{oc} - V_a|/d, \quad (4-2)$$

where V_a is the applied voltage, V_{oc} is the open circuit voltage and d is the thickness of the active layer[71]. We want to note that this equation is only valid when $V_a < 0$. When $V_a > 0$, the electric field is not uniformly distributed anymore inside the active layer. For more details, please see Chapter 7 Fig. 7-6, Fig. 7-13, Fig. 7-19 and Fig. 7-25. Typically, under the large reverse bias, the electric field can reach $\sim 10^8$ V/m and the polaron pair dissociation probability is $\sim 1^*$.

*Please see Chapter 5 for more details.

Under these conditions equation 4-1c becomes

$$\frac{1}{q} \frac{\partial}{\partial x} J_n = -\eta_{ed} G_{exciton}. \quad (4-3)$$

By integrating the distance x from 0 to the active layer thickness, l , we get

$$\left\{ \begin{array}{l} J_n(0) = 0 \\ J_n(l) = -q\eta_{ed} \int_{x=0}^l G_{exciton}(x) dx \end{array} \right. \quad (4-4a)^*$$

Similarity, the current density for the positive free polaron at the boundary is given by

$$\left\{ \begin{array}{l} J_p(0) = -q\eta_{ed} \int_{x=0}^l G_{exciton}(x)dx \\ J_p(l) = 0 \end{array} \right. \quad (4-4b)^*$$

* $J_n(0)$ and $J_p(l)$ are calculated from numerical simulation, which is described in Chapter 7.

Therefore, the current density $J=J_p+J_n$ under the high reverse bias is equal to

$$-q\eta_{ed} \int_{x=0}^l G_{exciton}(x)dx \quad (4-4c)$$

and the exciton generation rate is given by

$$G_{exciton}(x) = \int \frac{\alpha_j(\lambda)I_j(x,\lambda)}{I_0(\lambda)} \times N(\lambda)d\lambda, \quad (4-5)$$

where α_j is the absorption coefficient of active layer j , $I_j(x,\lambda)$ is the light intensity of active layer j at location x and wavelength λ , $N = R / (hc / \lambda)$ is the number of photons per second at λ , and $R(W/m^2/nm)$ is the spectral irradiance. Combining Eq. (3-9), Eq. (4-4c), Eq. (4-5) and the measured J-V curve, the exciton diffusion efficiency can be extracted.

4.3 Exciton generation rate, J-V curve, and exciton diffusion efficiency under AM1.5 illumination

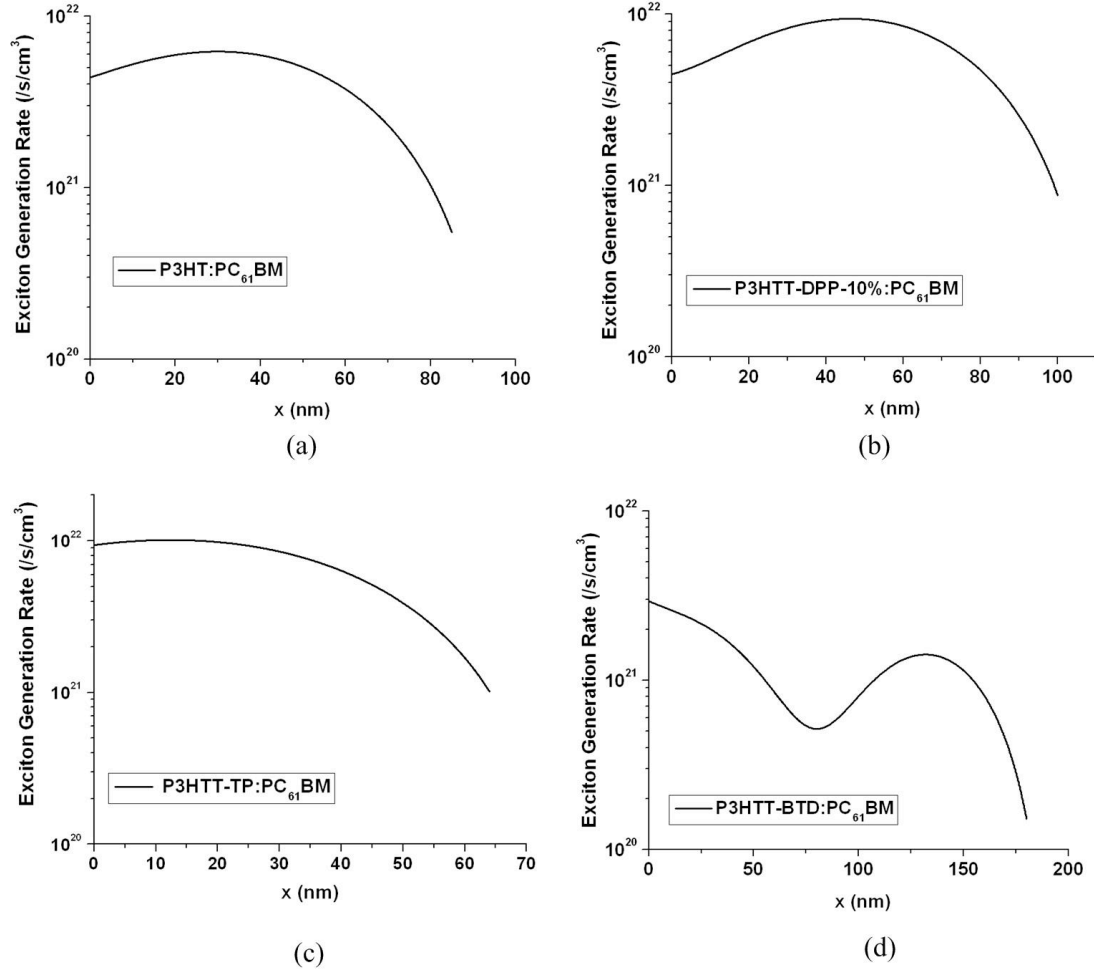
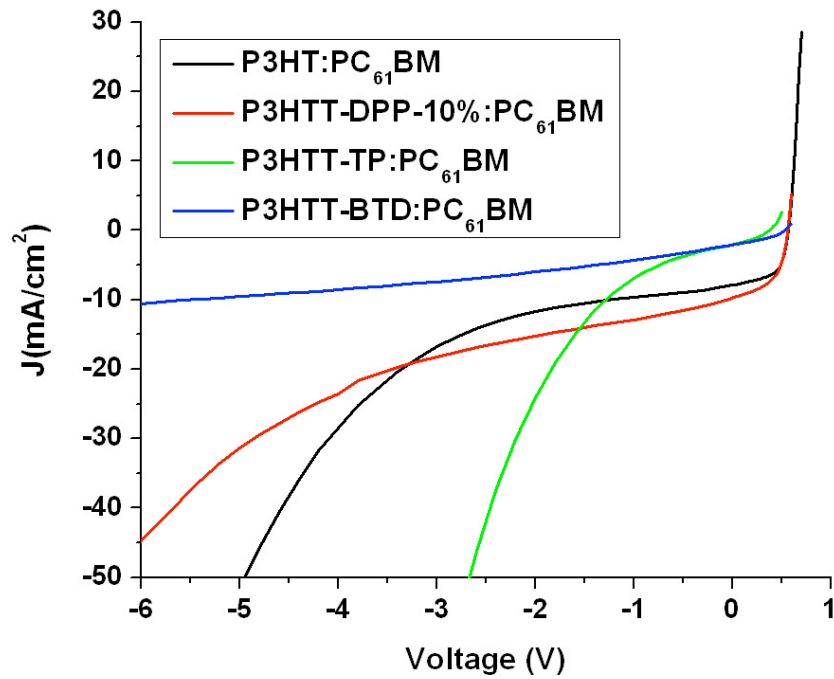


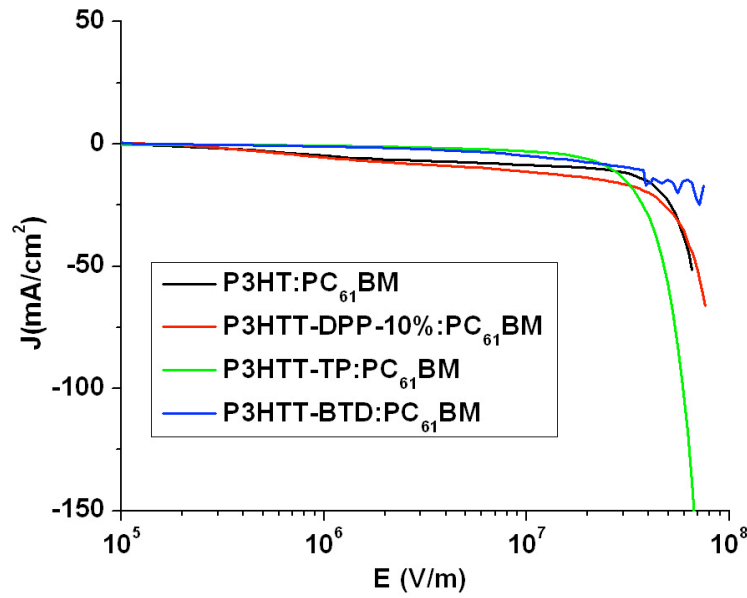
Figure 4-1. Exciton generation rate for (a) P3HT:PC₆₁BM, (b)P3HTT-DPP-10%: PC₆₁BM , (c) P3HTT-TP:PC₆₁BM and (d) P3HTT-BTD: PC₆₁BM solar cells.

The exciton generation rates as a function of depth x for four different solar cells were calculated under AM1.5 one sun condition and are shown in Fig. 4-1. Fig. 4-2(a) shows the J-V curves for the four types of solar cells in Fig. 4-1. Fig.4-2(b) plots the current density in term of the electrical field $E=|V_{oc}-V_a|/d$ inside of the devices. Initially the current density decreases slightly with increasing electric field. However, the current

decreases dramatically after the electric field reaches $\sim 2 \times 10^7 \text{ V/m}$. For P3HTT-BTD: PC₆₁BM devices, the current becomes very unstable after the electric field reaches $\sim 2 \times 10^7 \text{ V/m}$. We also observed that the I-V curve of P3HTT-BTD: PC₆₁BM solar cells can not be reproduced once the cells are applied by voltage of -7V. The Onsager-Braun model[70] predicts constant current density after the electric field is sufficient for the polaron pair dissociation probability to reach unity. However, as shown here, we observe a breakdown characteristic. We note, however, that different devices on the same wafer exhibit different breakdown voltages due to variations in fabrication. The plots shown here are the characteristics a typical device.



(a)



(b)

Figure 4-2. (a) J - V curves and (b) J versus electric field, E , curves for solar cells under AM1.5 illumination.

There are three effects that contribute to breakdown [26]: (1) thermal instability, (2) tunneling, and (3) avalanche multiplication. Thermal instability is typically due to the positive feedback of the temperature and the current. Owing to heat dissipation caused by the reverse current at high electric field, the junction temperature increases. This temperature increase, in turn, increases the reverse current relative to its value at lower voltages. The thermal instability is important at room temperature, but becomes less important compared with the other two mechanisms at very low temperatures. Tunneling effect is a quantum-mechanical phenomenon by which carriers can tunnel through a potential barrier if this barrier is sufficiently thin. This thin barrier is usually induced by a large electric field. Tunneling can occur at the p-n junction or at the contacts. The tunneling current of a p-n junction is described as

$$J_t = \frac{\sqrt{2m^*} q^3 E V_R}{4\pi^2 \hbar^2 \sqrt{E_g}} \exp\left(-\frac{4}{3} \frac{\sqrt{2qm^*} \phi_B^{3/2}}{\hbar E}\right), \quad (4-6)$$

where m^* is the effective mass of the material, V_R is carrier velocity, \hbar is Planck constant and ϕ_B is the barrier height. The breakdown voltage due to the tunneling effect has a negative temperature coefficient; i.e., the breakdown voltage decreases with increasing temperature. Avalanche breakdown is a phenomenon that can occur in both insulator and semiconductor materials. It occurs when the carriers in the transition region are accelerated by the electric field to excite additional free carriers through impact ionization. Compared to the tunneling effect, avalanche breakdown is characterized by a positive temperature coefficient. To determine which mechanism dominates, the photocurrent was measured at different temperatures. Due to equipment limitations in our lab, the measurements were only conducted using a Helium-Neon laser source, which will be described in section 4.4.

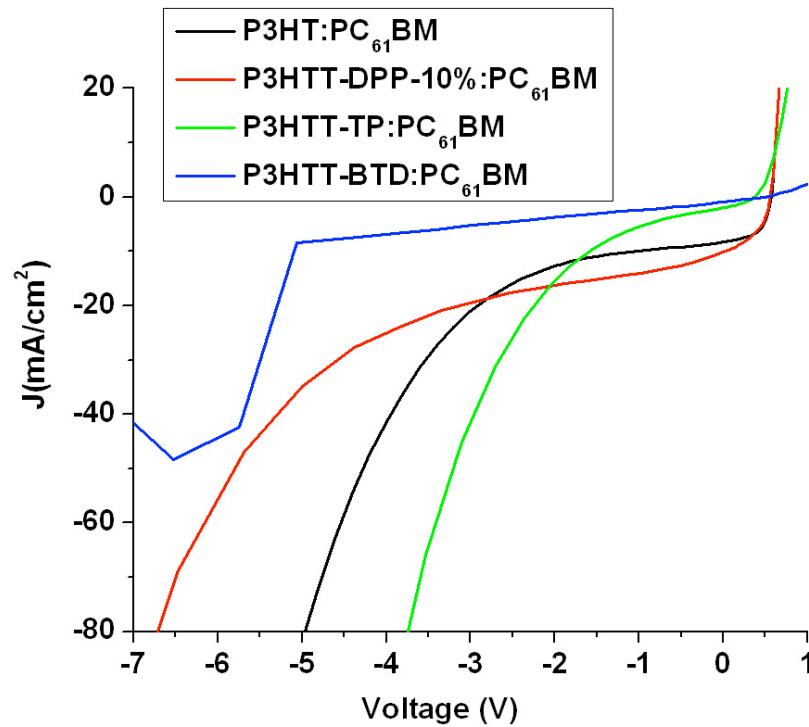
Table 4-1. Exciton diffusion efficiency of P3HT:PC₆₁BM, P3HTT-DPP-10%: PC₆₁BM, P3HTT-TP: PC₆₁BM and P3HTT-BTD: PC₆₁BM solar cells.

	η_{ed} (%) for AM1.5	J_{sc} (mA/cm ²)	PCE (%)
P3HT:PC ₆₁ BM	100	8.07	2.70
P3HTT-DPP-10%:PC ₆₁ BM	100	9.99	3.14
P3HTT-TP:PC ₆₁ BM	33.8	1.90	0.24
P3HTT-BTD:PC ₆₁ BM	69.6	2.27	0.46

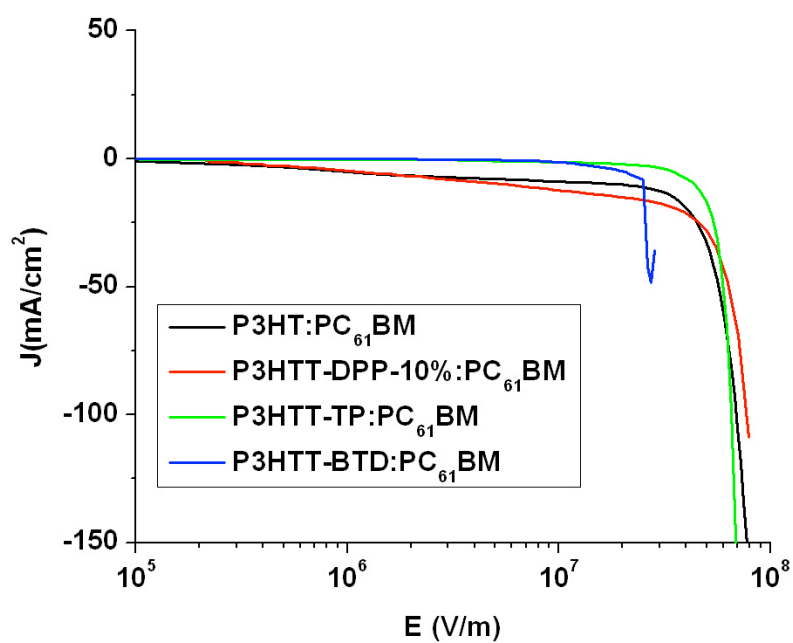
Considering the validation of Eq. 4-4c and the breakdown effect, the current density of Eq. 4-4c is extracted at $E=1 \times 10^7$ V/m. The exciton diffusion efficiency for these materials is presented in Table 4-1.

4.4 Breakdown mechanism study by varying the temperature

Figure 4-3 shows the J-V and J-E curve for four different devices under a 532 nm laser illumination. By tuning the intensity of the light source, the short circuit current density is set to match the J_{sc} under AM1.5 condition at room temperature. These curves are similar to the plots in Fig. 4-2.



(a)



(b)

Figure 4-3. (a) J - V curves and (b) J - E curves for solar cells under a 532nm laser illumination.

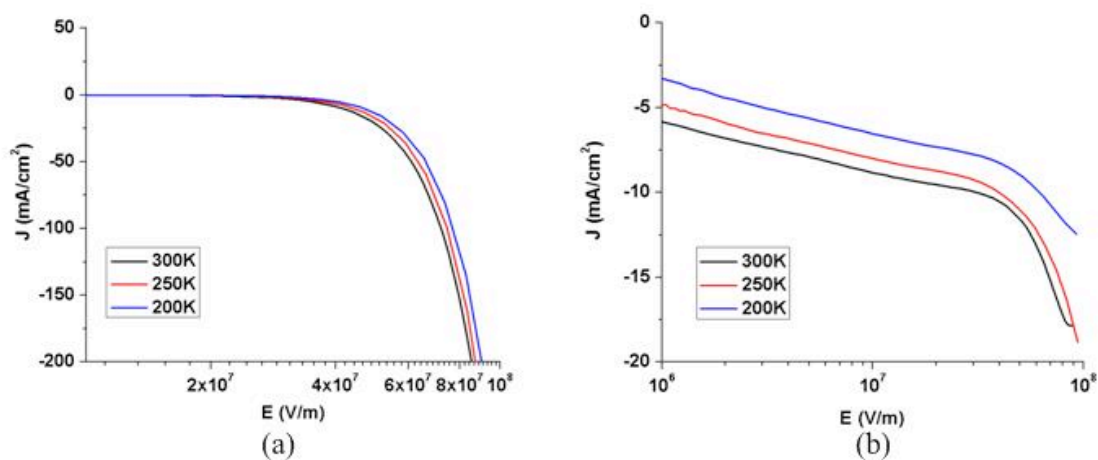


Figure 4-4. (a) Dark current and (b) Photo current for P3HT:PCB61M solar cells.

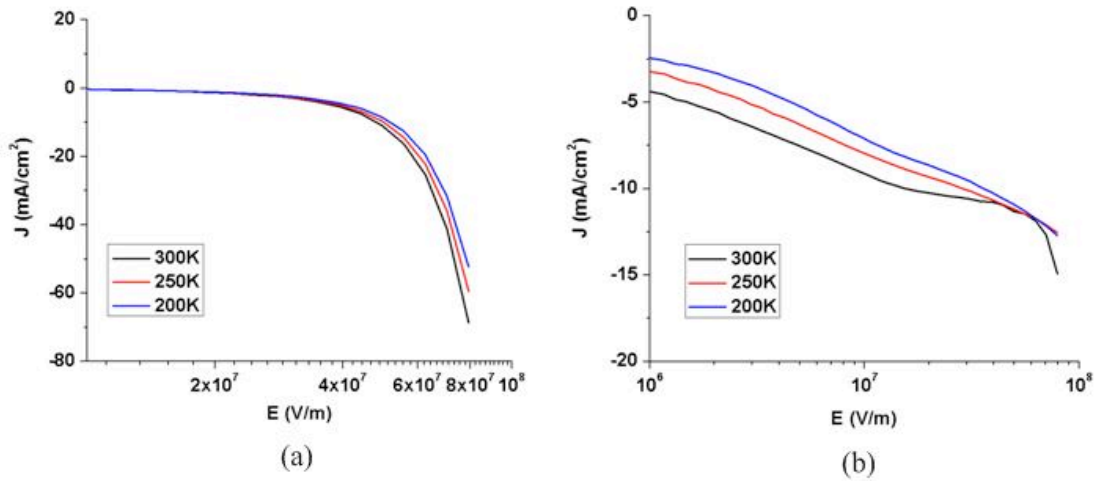


Figure 4-5. (a) Dark current and (b) Photo current for P3HTT-DPP-10%:PCB₆₁M solar cells.

In order to analyze the breakdown mechanisms, four types of devices were tested at three different temperatures 200K, 250K and 300K. To differentiate tunneling and impact ionization breakdown, the dark and photo currents were both measured. These are shown in Fig.4-4 to Fig.4-7. Here, the photocurrent is the difference between the total current and the dark current. For P3HT:PCB₆₁M and P3HTT-TP:PCB₆₁M solar cells, the dark current drops by a factor of 200 times for electric field $> 6 \times 10^7$ V/m, while the photocurrent drops by only a factor of 5. The slow drop of photocurrent indicates that impact ionization is not significant. For both curves at the same current density, the higher the temperature the lower is the electric field. The negative temperature coefficient of the p-n junction and the sharp dark current breakdown indicate strong tunneling[26], which is due to the ultra thin active layer of the solar cell structure. The simulation results in chapter 7 show that the electrical field near the contact is even higher, which also enhances the tunneling current between metal and semiconductor contact. For P3HTT-DPP-10%:PCB₆₁M solar cells, impact ionization appears insignificant because

the photocurrent drops linearly at high electrical field region. However, tunneling still dominates since the dark current drops 60 times. For P3HTT-BTD:PCB₆₁M solar cells, the reason for the breakdown is unclear. We observed that the J-V curve could not be recovered after applying an electric field of 6×10^6 V/m. The curves exhibit big gaps between 300K and 250K due to the device deterioration. The characterization was terminated at $\sim 6 \times 10^6$ V/m, otherwise no data could have been obtained at 200K.

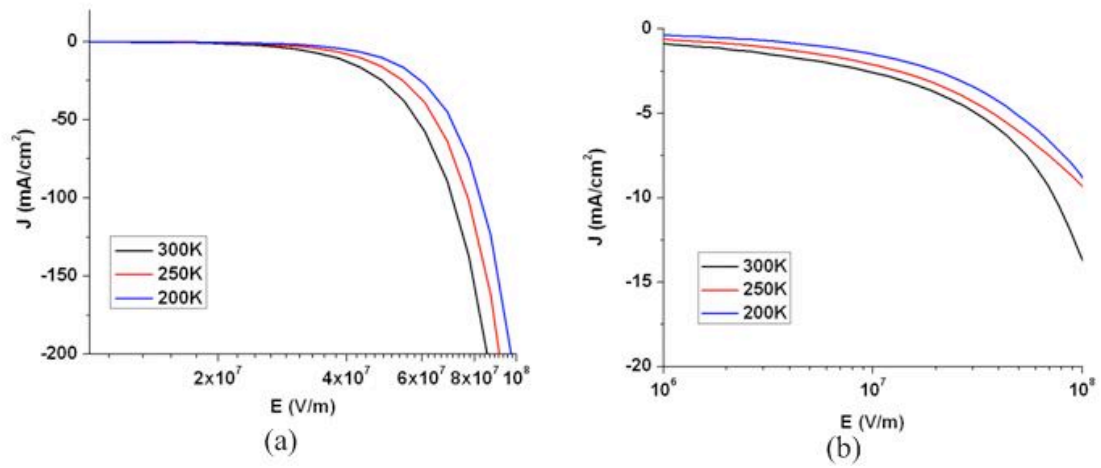


Figure 4-6 (a) dark current and (b) photo current for P3HTT-TP:PCB₆₁M solar cells.

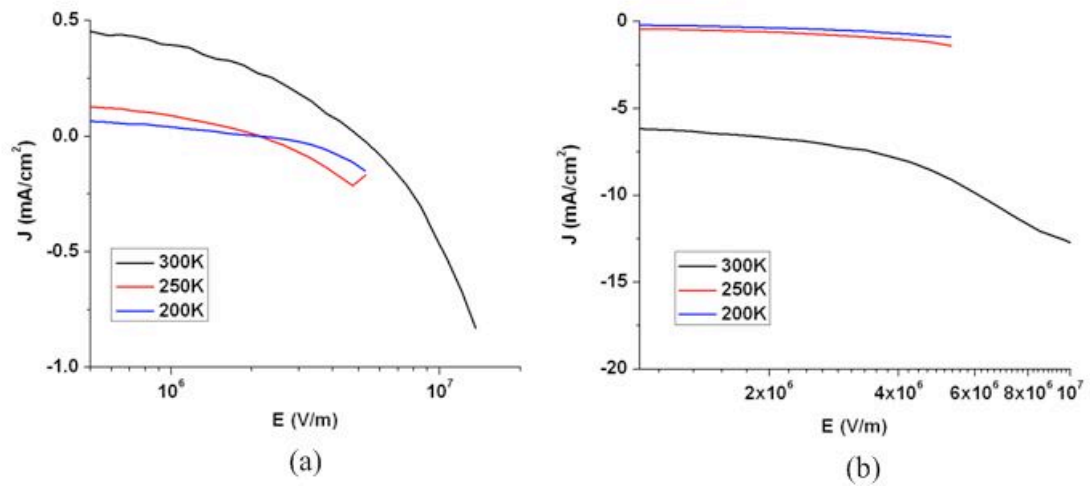


Figure 4-7. (a) Dark current and (b) Photo current for P3HTT-BTD:PCB₆₁M solar cells.

4.5 Summary

In this Chapter, exciton diffusion efficiency is analyzed by using J-V measurements at large reverse bias. The efficiencies for four polymers with PC₆₁BM are presented. Under large reverse bias, the current shows a large drop after the electric field reaches $E=6\times 10^7$ V/m. This is contrary to the field-independent current predicted by the Onsager-Braun model. The current drop is analyzed in terms of the breakdown mechanisms, and the tunneling effect is found to be the dominate breakdown mechanism in most devices.

Chapter 5. Polaron pair dissociation

5.1 Introduction

After the excitons reach the donor/acceptor interface, they do not directly dissociate into free charge carriers. Instead, first a bound polaron, also referred to as pair charge transfer (CT) complexes or geminate pairs will be formed. This is a crucial intermediate step between exciton dissociation and free charge generation [72-76]. At the interface, the CT complexes will either dissociate into free polarons or recombine. V. D. Mihailetschi and et al.[77] found that for the poly(2-methoxy-5-(3',7'-dimethyloctyloxy)-p-phenylene vinylene) (OC₁C₁₀-PPV):PC₆₁BM blend at room temperature only 60% of the generated geminate pairs dissociated and contributed to the short-circuit current. M. Limpinsel and et al.[78] calculated that the dissociation efficiency of geminate pairs in the bulk was 40%-60% for P3HT:PC₆₁BM at zero field. Geminate pair dissociation is still considered as a major loss mechanism for BHJ solar cells.

In this chapter, the well-established Onsager-Braun model [70] is introduced first. Then, the polaron pair dissociation efficiency is analyzed with the Onsager-Braun model for four different polymers combined with PC₆₁BM to form solar cells.

5.2 Onsager-Braun model

The Onsager-Braun model [70] describes a balance between CT recombination and dissociation rates. The net generation rate, G , for free charges can be expressed as[70, 77, 78]

$$G(T, E) = G_{\max} P_{\text{diss}}(T, E), \quad (5-1)$$

$$P_{diss}(T, E) = \frac{k_{diss}(E)}{k_{diss}(E) + k_f}, \quad (5-2)$$

where G_{max} is the maximum polaron pair generation rate, $P_{diss}(T, E)$ is the probability for free charge creation at the donor-acceptor interface, $k_{diss}(E)$ is the dissociation rate of a bound geminate pair, and k_f is the decay rate of the pair to the ground state. This model yields the following expression for the rate

$$k_d(E) = k_R \frac{3}{4\pi a_0^3} e^{-E_B/kT} \frac{J_1(2\sqrt{-2b})}{\sqrt{-2b}}, \quad (5-3)$$

where a_0 is the initial separation distance of the geminate pair at the interface, $E_B = q/(4\pi\epsilon_0\epsilon_r a_0)$ is the polaron pair binding energy, J_1 is the Bessel function of order one. The term b can be expressed as $b = e^3 E / 8 \pi \epsilon_0 \epsilon_r k^2 T^2$, where e is the charge of an electron, E is the internal electric field, ϵ_0 is permittivity of free space, ϵ_r is relative permittivity, k is the Boltzmann constant, and T is absolute temperature. k_R is given by Langevin[79]: $k_R = q \langle \mu \rangle / \epsilon_0 \langle \epsilon_r \rangle$, where $\langle \mu \rangle$ is the spatially averaged sum of electron and hole mobilities and $\langle \epsilon_r \rangle$ is the spatially averaged dielectric constant. As a result, Eq. 5-2 should be integrated over a distribution of separation distances

$$P(T, E) = N_F \int_0^\infty P(x, T, E) F(x) dx, \quad (5-4)$$

where $P(x, T, E)$ is the probability that free charges are generated at a separation distance, x , temperature, T , and electric field, E . $F(x)$ is the distribution function of donor-acceptor separation and N_F is a normalization factor for the function $F(x)$. The normalization factors for different distribution functions $F(x)$ are given by:

$$(1) \text{ Delta distribution-} \quad F(x) = \delta(x - a_0), \quad N_F = 1; \quad (5-5a)$$

$$(2) \text{ Gaussian distribution-} \quad F(x) = r^2 e^{-r^2/a_0^2}, \quad N_F = \frac{4}{\pi^{1/2} a_0^3}; \quad (5-5b)$$

$$(3) \text{ Exponential distribution-} \quad F(x) = e^{-x^2/a_0}, \quad N_F = \frac{1}{a_0}; \quad (5-5c)$$

$$(4) x^2 \text{ Exponential distribution-} \quad F(x) = x^2 e^{-x/a_0}, \quad N_F = \frac{1}{2a_0^3}. \quad (5-5d)$$

5.3 Polaron pair dissociation probability

Based on the model, the polaron pair dissociation probability was simulated using MATLAB. Here, we use the delta function distribution since it has been found to be consistent with measured J-V curves and binding energies [78, 80]. The fitting parameters used in the Eq. 5-2 are listed in Table 5-1 and Table 5-2.

Table 5-1. Parameters used in the Onsager-Braun model calculation for P3HT:PC₆₁BM and P3HTT-DPP-10%:PC₆₁BM solar cells.

	P3HT:PC ₆₁ BM	P3HTT-DPP-10%:PC ₆₁ BM
ε_r	3.4	3.4
k_f (1/s)	5×10^5	6×10^5
a_0 (nm)	1.9	1.9
μ (cm ² V ⁻¹ s ⁻¹)	2.4×10^{-4}	2.3×10^{-4}
E_B (eV)	0.223	0.223
η_{cd} (%)	91	85

Table 5-2. Parameters used in the Onsager-Braun model calculation for P3HTT-TP:PC₆₁BM and P3HTT-BTD:PC₆₁BM solar cells.

	P3HTT-TP:PC ₆₁ BM	P3HTT-BTD:PC ₆₁ BM
ϵ_r	3.0	3.4
k_f (1/s)	7.1×10^5	5×10^6
a_0 (nm)	1.8	1.9
μ (cm ² V ⁻¹ s ⁻¹)	2.5×10^{-4}	2.1×10^{-4}
E_B (eV)	0.266	0.223
η_{cd} (%)	53	27

The mobility was measured by the space charge limited current (SCLC) method [81] as described in chapter 2. The relative dielectric constant ϵ_r was extracted from the geometrical capacitance of the solar cells. Figure 5-1 shows the C-V curves for four types of solar cells. Typically, the capacitance-voltage curves are characterized by three regions [82, 83]. At reverse bias where $V \ll V_{bi}$ (region I), the active layer is totally depleted and therefore the measured capacitance is constant and corresponds to the geometrical capacitance $C_{geo} = \epsilon \epsilon_r A / d$. In the low forward bias region where $V < V_{bi}$ (region II), the capacitance exhibits a bias dependence Mott-Schoottky behavior [84]

$$C^{-2} = \frac{2(V_{bi} - V)}{A^2 q \epsilon \epsilon_r N_A}, \quad (5-6)$$

where A is the area of the device and N_A is the concentration of acceptor impurities. With further increase in forward bias (region III), the capacitance decreases again due to injection.

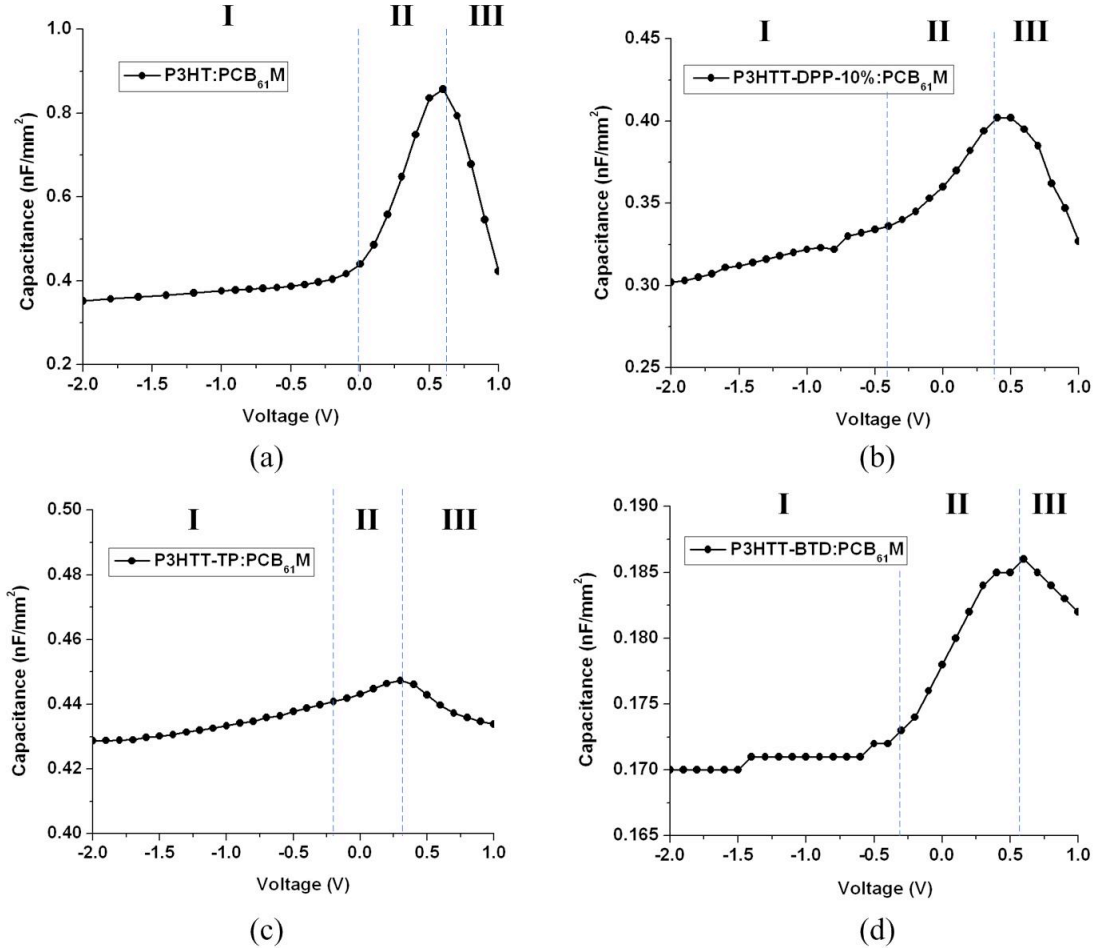


Figure 5-1. C-V curves for (a) P3HT:PC₆₁BM, (b)P3HTT-DPP-10%: PC₆₁BM , (c) P3HTT-TP:PC₆₁BM and (d) P3HTT-BTD: PC₆₁BM solar cells.

The initial separation of polaron pair a , for P3HT is set to 1.9nm [78]. Based on the grazing-incidence X-ray diffraction (GIXRD) results [31, 32], the P3HTT-DPP-10% and P3HTT-BTD show the similar interchain distance as P3HT. Therefore the initial separations of polaron pair for them are both set to 1.9nm. For P3HTT-TP, on the other hand, seems to be completely amorphous by GIXRD study. As a comparison with three other polymers, we set the initial separations of polaron pair as 1.8nm. Polaron pair (geminate pair) decay time k_f was extracted from J - V curves [45]. As can be seen, the decay rate of the geminate pair to the ground state is a little higher for P3HTT-

TP:PC₆₁BM and P3HTT-BTD:PC₆₁BM than for the materials P3HT:PC₆₁BM and P3HTT-DPP-10%:PC₆₁BM. At the same time, the initial separation length of the geminate pairs and the geminate pair binding energies are similar for polymer:fullerene pairs and correlate well with previously published data [8, 80, 85].

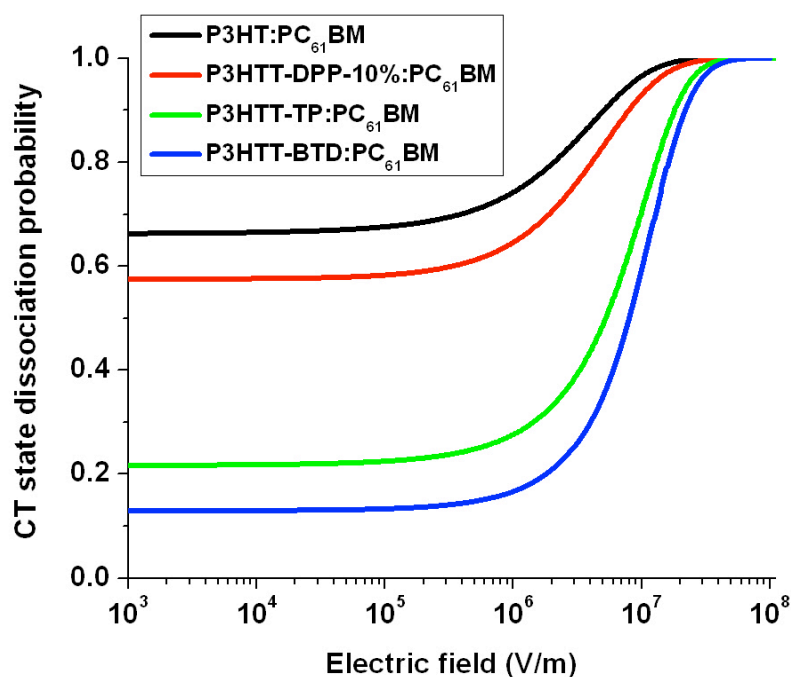


Figure 5-2. Polaron pair dissociation probability for four different polymer:PC₆₁BM solar cells.

The simulated polaron pair dissociation probability as a function of electric field at room temperature is shown in Fig. 5-2 and the calculated geminate pair dissociation probabilities at short-circuit condition are listed in Table 5-1 (η_{cd}). As can be seen, P3HT:PC₆₁BM and P3HTT-DPP-10%:PC₆₁BM solar cells have significantly higher geminate pair dissociation efficiency to form free polarons than P3HTT-TP:PC₆₁BM and especially P3HTT-BTD:PC₆₁BM OPVs. Since the initial separation lengths of geminate

pairs and geminate pair binding energies for all polymer:fullerene pairs are found to be similar, the faster recombination of the geminate pairs to the ground state for TP- and BTD-based solar cells is determined to be responsible for drop of η_{cd} . We note, that the molecular weights (M_n) of all the polymers are similar (15,000 – 20,000 g/mol), which eliminates M_n differences as an explanation for the differences in lifetime of the geminate pairs [86].

5.4 Summary

In this Chapter, polaron pair dissociation efficiency is analyzed using the well known Onsager-Braun model. At short circuit condition, η_{cd} is 91%, 85%, 53% and 27% for P3HT:PC₆₁BM, P3HTT-DPP-10%:PC₆₁BM, P3HTT-TP:PC₆₁BM and P3HTT-BTD:PC₆₁BM solar cells, respectively. The big variance arises from the difference in polaron pair decay rates. However, the underlying physical mechanisms for the different decay rates necessitates further study. The capacitance characteristics are also tested and analyzed. For four different polymer:PC₆₁BM solar cells, C-V curves exhibit similar behavior, which verified the available C-V theory for BHJ solar cells.

Chapter 6. Free polaron collection

6.1 Introduction

Once the free charges are generated by dissociation of bound polarons at a donor/acceptor interface, they will either be collected by the electrodes through diffusion or drift, or recombine by one of a variety of mechanisms. In this chapter, we focus on the analysis of free polaron collection efficiency. The free polaron collection efficiency (η_{cc}) [87], can be described as the ratio of the free polaron collection rate, R_c , to the free polaron generation rate, R_r , which can be expressed as:

$$\eta_{cc} = \frac{R_c}{R_c + R_r} = \frac{1/t_{sw}}{1/t_{sw} + 1/t_r} = \frac{1}{1 + t_{sw}/t_r}, \quad (6-1)$$

where t_r is the average recombination lifetime and t_{sw} is the sweep-out time. t_{sw} is determined by the internal voltage V_{int} , the free polaron mobility μ , and the thickness of the drift region d , which is

$$t_{sw} = \frac{d^2}{n\mu V_{int}}, \quad (6-2)$$

where n can be 1 or 2, depending on whether or not free polarons are generated throughout the whole device.

The sweep out time can be measured by the time of flight (TOF) [88-90] method or the transient photoconductivity method [71]. For TOF, the films have to be several micrometers thick to ensure that some of the polarons are generated within a small space near the surface of the device and then traverse the whole bulk heterojunction region. However, making the films thick may alter the device characteristics to the extent of negating the applicability of the measured t_{sw} . Transient photoconductivity, on the other

hand, has the advantage that measurements can be made on thin films. For visible wavelengths, free polarons are created relatively uniformly throughout a ~ 100 nm-thick solar cell. For this case, n in Eq. 6-2 is equal to 2.

Recombination lifetimes, on the other hand, should be a characteristic of the material and relatively independent of film thickness. Usually, the recombination mechanism is classified into two categories. The first is referred to as geminate recombination [91], which means the recombining free polarons were both created by the same exciton. The other process, non-geminate recombination, involves free polarons that were created by different excitons. There are several types of non-geminate recombination mechanisms, such as band-to-band recombination, monomolecular recombination through a Shockley-Read-Hall (SRH) interface, and reverse-diffuse [reverse-diffuse or reverse-diffusion?] recombination through contacts [92]. The approaches to determine recombination lifetimes include time-resolved vibrational spectroscopy [93, 94], impedance spectroscopy [95, 96], transient photoconductivity [71], and forward-to-reverse transient response [97]. To date, however, there is a wide discrepancy (100 ns to 10 ms) between the lifetimes measured with these different techniques.

In order to provide insight into the recombination lifetime, I have used three different measurement techniques, transient photoconductivity, forward-to-zero transient-current response, and electrical field dependent photoresponse. Measurements on P3HT:PCB₆₁M solar cells show that these three measurement techniques yield consistent results. I have used transient photoconductivity to characterize the recombination lifetimes for four types of polymer: PCB₆₁M solar cells because the sweep out time and

the recombination time constant can be obtained simultaneously. The free polaron collection efficiencies of these materials are also calculated and compared.

I have also investigated thermal annealing effects on mobility and lifetime. For organic BHJ solar cells, thermal annealing plays an important part in the device fabrication and performance since it can improve nanoscale morphology of the interpenetrating donor-acceptor networks, crystallinity of the polymer, and transport across the interface between the bulk heterojunction material and the aluminum electrode [98]. However, the mechanisms by which annealing affect charge transport are not fully understood. In this chapter, mobility and recombination life times of free polarons, as determined by SCLC and the transient technique [97], respectively, were measured at different annealing temperatures in P3HT:PCBM devices.

6.2 Transient photoconductivity

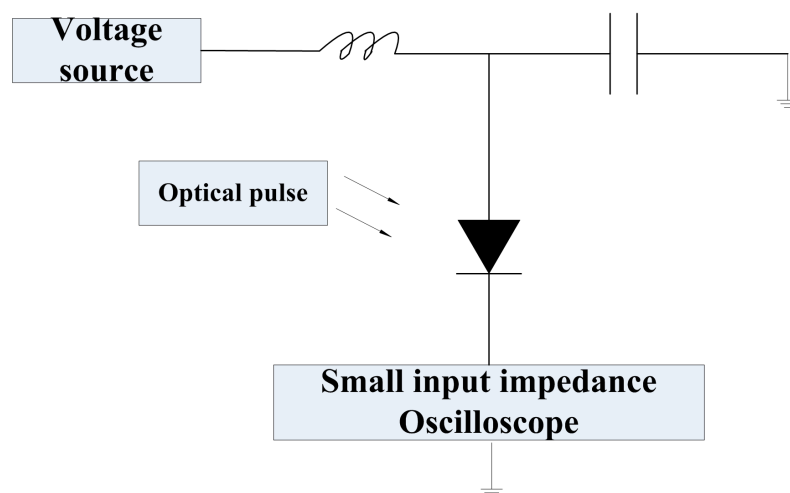


Figure 6-1. A typical circuit for measuring transient photoresponse.

Transient photoconductivity is a common technique used to study the competition between sweep-out and recombination of free charges in low mobility materials [99-102]. A typical circuit for measuring phototransient response is shown in Fig. 6-1. Under constant voltage an optical pulse is incident on the test material at a fix frequency. Then, the transient photoresponse is measured with an oscilloscope.

In order to get accurate results, several conditions need to be satisfied. First, the circuit RC time constant, $\tau = RC$, should be smaller than the device response. The capacitance of BHJ devices is usually very large, e.g., in the nF range for a typical 4 mm² device. Increasing the film thickness or decreasing the device area can reduce the capacitance. However, since a thicker device may have different properties than a typical solar cell structure, decreasing the area is more suitable. Second, the amount of charge generated should be carefully considered. On one hand, it should be small enough so that space-charge effects do not change the internal field significantly, i.e., the injected charge q should satisfy the condition $q \ll CV$. On the other hand, q should be large enough for good signal to noise response.

S. R. Cowan et al. have developed and applied this method to the two-carrier transient photocurrent in BHJ solar cells [71]. They measured the carrier response times, $\tau_{1/e}$, defined as the point of 1/e signal decay, for the fast and the slow carriers. In each case, the response time decreases with increasing internal voltage, i.e., high electric field, and saturates at low electric field. Since the decay of the carrier density is determined by recombination when the internal electric field approaches zero, the recombination lifetime can be defined as the carrier response time $\tau_{1/e}$ in the saturation region at low

electric field. Here, we have not differentiated between fast and slow carriers, but assume the current flow reflects the total number of carriers.

In this work, the optical source was a 640 nm diode laser driven with 10 ns pulses at 1 kHz repetition rate. We measured the transient photoconductivity from -0.5 V to 0.4 V in order to see both sweep out and recombination characteristics. Fig. 6-2 shows a typical transient photoresponse for a P3HT/PC₆₁BM solar cell. The response time, $\tau_{1/e}$, was determined and then plotted versus the internal voltage in Fig. 6-3. In the high internal voltage region, $\tau_{1/e}$ increases as voltage decreases. This is due to the fact that the response time is dominated by the sweep-out time t_{sw} . In the low internal voltage region, the voltage dependence is greatly diminished as the internal voltage approaches zero and recombination dominates. The recombination lifetime for free polarons is estimated to be $\sim 1.2 \mu\text{s}$.

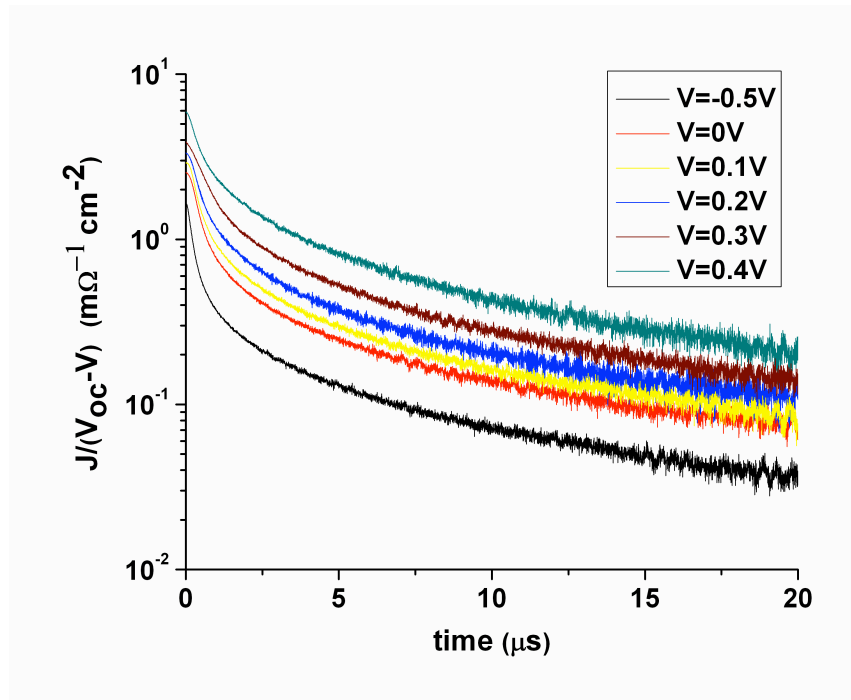


Figure 6-2. Transient photocurrent at different applied voltages for a P3HT/PC₆₁BM solar cell at room temperature.

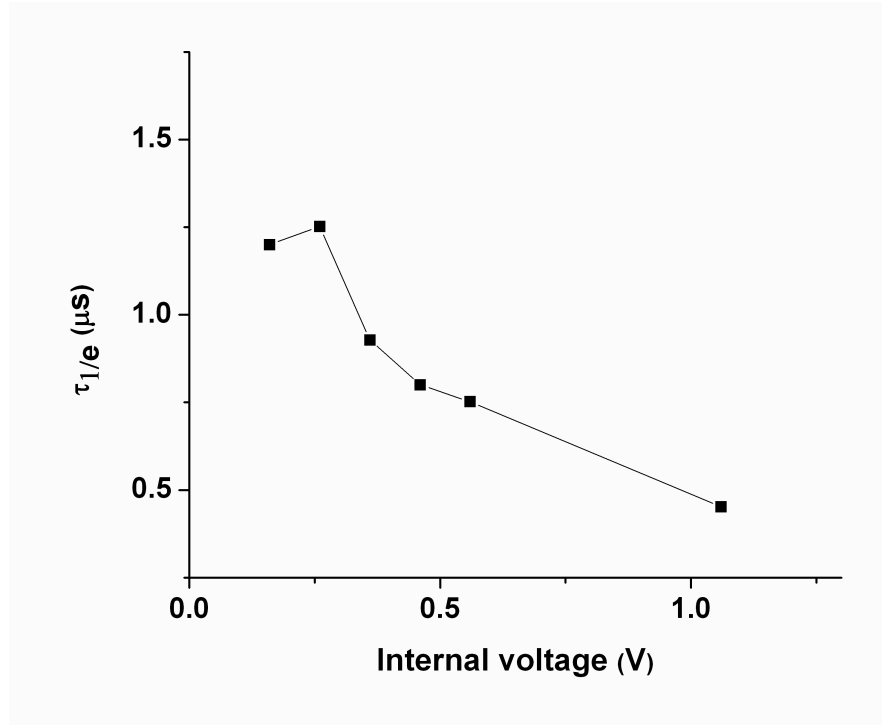


Figure 6-3. $\tau_{1/e}$ as a function of internal voltage.

6.3 Forward-to-zero transient current response

6.3.1 introduction

The forward-to-zero transient response technique is a widely used method to measure minority carrier lifetime in inorganic devices. It can also be extended to measurement of the free polaron recombination lifetime in BHJ solar cells. In contrast to the forward-to-reverse transient response technique, the internal electrical field is near zero and, after switching, almost all the excess carriers will recombine prior to being collected by the electrodes. A typical switching circuit for this type of measurement is shown in Fig. 6-4(a). For $t < 0$, a forward current, I_F , flows in the device. At $t = 0$, the

switch is thrown to the right with initial reverse current, I_R . Fig. 6-4 (b) illustrates the current and voltage switching characteristics of an organic diode.

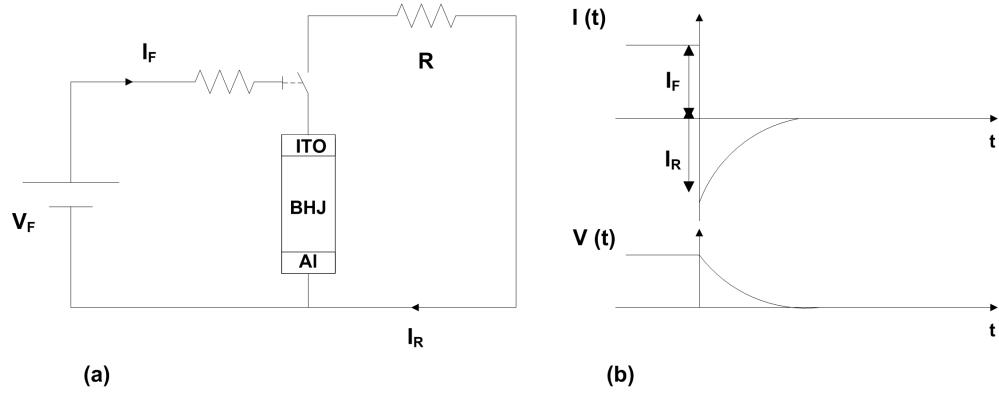


Figure 6-4. (a) Basic switching circuit apparatus and (b) typical current and voltage switching characteristics.

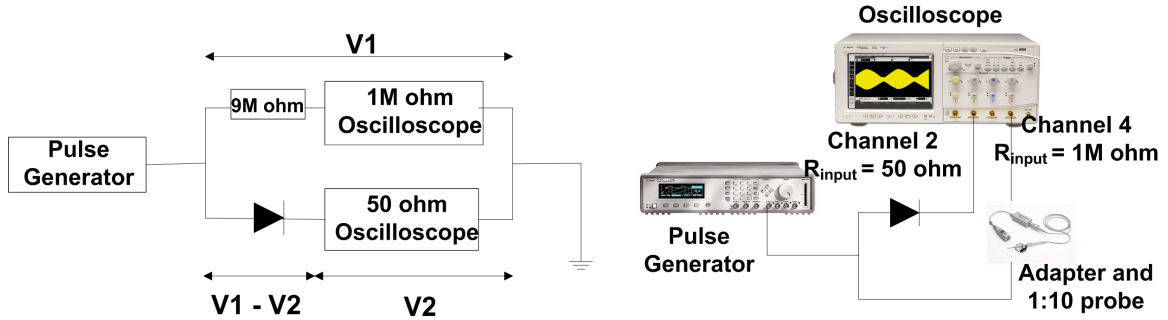


Figure 6-5. Measurement circuit to characterize the transient behavior of BHJ devices.

6.3.2 The theory for transient current response

The transient response can be determined by solving the continuity equations,

$$\frac{\partial p(x,t)}{\partial t} = G_p - U_p - \frac{1}{q} \nabla J_p \quad (6-3)$$

$$\frac{\partial n(x,t)}{\partial t} = G_n - U_n + \frac{1}{q} \nabla J_n, \quad (6-4)$$

where p and n are the positive and negative polaron densities, respectively; G_p and G_n are the positive and negative polaron generation rates that originate from external sources such as optical excitation; and $U_n = Vn/\tau_n$ and $U_p = Vp/\tau_p$ are the recombination rates for positive and negative polarons.

In order to solve the above equations, we use the following current density equations [4]

$$J = J_p + J_n, \quad (2-3)$$

$$J_p = -q\mu_p pE - qD_p \frac{dp}{dx}, \quad (2-4a)$$

$$J_n = -q\mu_n nE + qD_n \frac{dn}{dx}, \quad (2-4b)$$

$$\nabla J_p = -(q\mu_p p \frac{\partial E}{\partial x} + q\mu_p E \frac{\partial p}{\partial x}) - qD_p \frac{\partial^2 p}{\partial x^2}, \quad (6-5a)$$

$$\nabla J_n = -(q\mu_n n \frac{\partial E}{\partial x} + q\mu_n E \frac{\partial n}{\partial x}) + qD_n \frac{\partial^2 n}{\partial x^2}. \quad (6-5b)$$

It is also necessary to define the recombination rates. Different from inorganic solar cells, the current of organic solar cells is attributed to the majority carrier, i.e., free polarons. This is equivalent to the high-level injection case in an inorganic solar cell. It follows that the lifetimes of the positive and negative polarons are the same. Therefore, the recombination rate can be expressed as:

$$U_p = (p - p_0)/\tau_p = Vp/\tau, \quad (6-6a)$$

$$U_n = (n - n_0)/\tau_n = Vn/\tau. \quad (6-6b)$$

An explicit expression for t_l (the time interval from $t = 0$ to the time when the voltage on the BHJ device drops to zero) can be obtained using a charge-control model.

In the dark, G_p and G_n are zero. The total charge carrier Q in the device at time t is given by the integral

$$Q(t) = qA \int (\Delta p(x, t) - \Delta n(x, t)) dx \quad (6-7)$$

which is obtained by subtracting Eq. 6-4 from Eq. 6-3, multiplying by qA , and integrating x over the thickness of the active region. After the current is switched to the reversed mode, Eq. 6-4 becomes

$$\begin{aligned} & \frac{qA \int \partial p(x, t) dx}{\partial t} - \frac{qA \int \partial n(x, t) dx}{\partial t} \\ &= \frac{qA \int (\Delta p(x, t) - \Delta n(x, t)) dx}{\tau} - \frac{qA}{q} \int (\nabla J_p + \nabla J_n) dx \\ &= \frac{qA \int (\Delta p(x, t) - \Delta n(x, t)) dx}{\tau} \\ & \quad - \frac{qA}{q} \int \left(-(q\mu_p p \frac{\partial E}{\partial x} + q\mu_p E \frac{\partial p}{\partial x}) - qD_p \frac{\partial^2 p}{\partial x^2} \right. \\ & \quad \left. + (-q\mu_n n \frac{\partial E}{\partial x} + q\mu_n E \frac{\partial n}{\partial x}) + qD_n \frac{\partial^2 n}{\partial x^2} \right) dx \\ &= \frac{qA \int (\Delta p(x, t) - \Delta n(x, t)) dx}{\tau} \\ & \quad - A \left((-q\mu_p p E - qD_p \frac{dp}{dx}) + (-q\mu_n n E + qD_p \frac{dn}{dx}) \right) \end{aligned} \quad (6-8)$$

Substituting Eq. 6-7 into Eq. 6-8, yields

$$\frac{dQ}{dt} = \frac{Q}{\tau} - I_R(t). \quad (6-9)$$

Eq. 6-9 is essentially the same as that used to calculate the minority carrier lifetime for inorganic semiconductor devices [22]. The solution to this first-order nonhomogeneous linear differential equation is

$$Q(t) = e^{-\frac{t}{\tau}} \left(-\int e^{\frac{t}{\tau}} I_R(t) dt + C \right). \quad (6-10)$$

With initial condition $Q(0) = I_F \tau$ and the boundary condition $Q(t_l) = 0$, the recombination lifetime for free polarons can be determined.

6.3.3 Experiment results and discussion

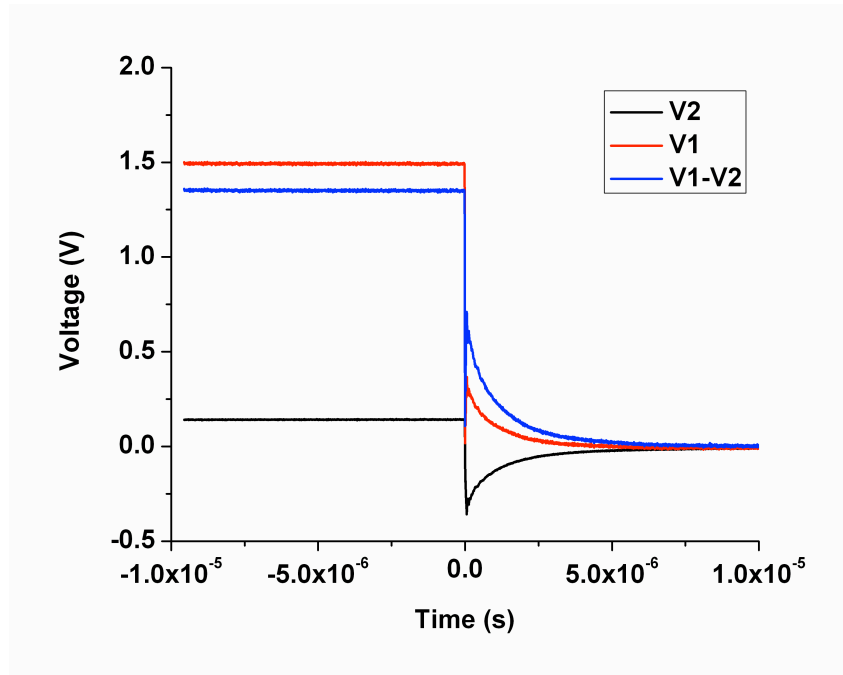


Figure 6-6. Current and voltage switching characteristics of a P3HT:PCBM device.

The switching circuit of Fig. 6-4 was implemented with an Agilent Infinium DSO81004B Oscilloscope and an Agilent 81110A pulse generator. The bandwidth of the oscilloscope is 10 GHz with sample rate up to 40 GS/s. The input impedance of each channel of the oscilloscope is 50Ω. With an Agilent E2697A adapter, the input

impedance of the oscilloscope can be transformed to 1 M Ω . The measurement circuit is shown in Fig 6-5. A 100 Hz square wave was generated by the pulse generator and applied to the parallel circuit. The rise and fall times of the square wave are both 2 ns. The current flow through the BHJ device was detected by the 50 Ω input channel. The voltage on the BHJ solar cell is the voltage difference between V1 and V2 (Fig. 6-5). The current and voltage switching characteristics of a P3HT:PCBM solar cell are shown in Fig. 6-6. Using Eq. 6-10, the recombination lifetime was estimated to be 1 μ s to 4 μ s.

6.4 Electrical-field-dependent photoresponse

The spectral external quantum efficiency, η_e , is an important characteristic of a solar cell. The higher the quantum efficiency, the larger will be the short circuit current. External quantum efficiency is the ratio of the number of charge carriers collected by the solar cell to the number of incident photons at a specific wavelength. It can be expressed as a product of efficiencies,

$$\eta_e = \eta_a \eta_{ed} \eta_{cd} \eta_{cc} . \quad (6-4)$$

Here, η_a is photon absorption efficiency, which is the ratio of the number of absorbed photons to the total number of incident photons. η_{ed} is the exciton diffusion efficiency, i.e., the ratio of the number of excitons that diffuse to a donor-acceptor interface to the number of absorbed photons; η_{cd} is the geminate pair dissociation efficiency; and η_{cc} is the free polaron collection efficiency. The external quantum efficiency can be written in terms of the responsivity, R , as

$$\eta_e = \frac{R \cdot h\nu}{q} = \left(\frac{h\nu}{qP_i} \right) \cdot I, \quad (6-5)$$

where P_l is the incident optical power. Combining Eq. 6-4 and Eq. 6-5, yields

$$\eta_a \eta_{ed} \eta_{cd} \eta_{cc} = \left(\frac{h\nu}{qP_l} \right) \cdot I . \quad (6-6)$$

The electrical-field-dependent method utilizes measurements of responsivity at different bias voltages and thus different internal electric fields (E_{int}). For the same device and same incident light level at a specific wavelength, η_a , P_l , and $h\nu$ should be independent of E_{int} . Since there are no reports that exciton generation and diffusion strongly rely on internal electric field, here we ignore the electric field influence on η_{ed} . It follows that

$$\frac{\eta_{cd1} \eta_{cc1}}{\eta_{cd2} \eta_{cc2}} = \frac{I_1}{I_2} , \quad (6-7)$$

where I_1 and I_2 are photocurrent values at different bias (E_{int}) values. Combining Eq. 6-6 and Eq. 6-7, the average recombination lifetime can be expressed as

$$t_r = \frac{I_2 t_{sw2} - I_1 t_{sw1} \frac{\eta_{cd2}}{\eta_{cd1}}}{I_1 \frac{\eta_{cd2}}{\eta_{cd1}} - I_2} . \quad (6-8)$$

In order to determine the recombination lifetime, it is necessary to determine three quantities: the measured photocurrent ratio, the sweep out lifetimes, and the geminate pair dissociation efficiency.

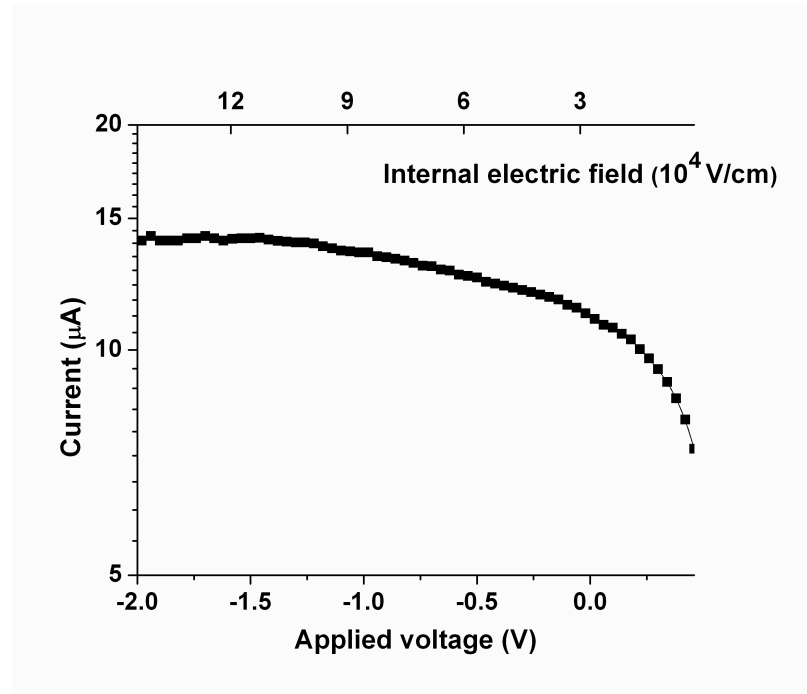


Figure 6-7. Photo current versus applied bias and internal electric field.

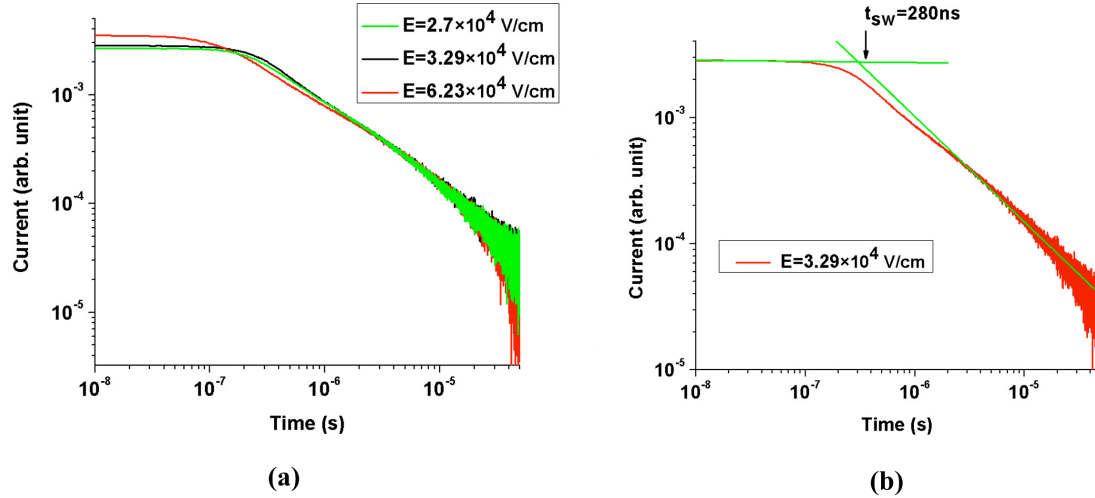


Figure 6-8. Transient photoconductivity for a P3HT/PCBM solar cell at room temperature. (a) Transient photoresponse at different internal electric field. (b) The sweep out time is determined by the intersection of two linear fitting lines.

The measured photocurrent response was realized with a tunable Helium-Neon laser and a lock-in amplifier. The wavelength was 632 nm and the chopper frequency was 310

Hz. The photocurrent versus bias and internal electric field (E) are shown in Fig. 6-7. From the current-voltage characteristic, V_{oc} was found to be 0.47 V.

The sweep-out time was measured by transient photoconductivity. The optical source was a 640 nm diode laser that was pulsed at 1 kHz. An Agilent Infiniium DSO81004B Oscilloscope was used to detect the photocurrent. The transient responses at different electrical fields are shown in Fig. 6-8(a). The sweep-out time is determined from the intersection of two linear fits as illustrated in Fig. 6-8(b) [88-90]. Using this approach, the sweep out time was estimated to be 150ns, 280ns and 320ns for internal electric fields of $6.23 \cdot 10^4$ V/cm, $3.29 \cdot 10^4$ V/cm and $2.7 \cdot 10^4$ V/cm, respectively.

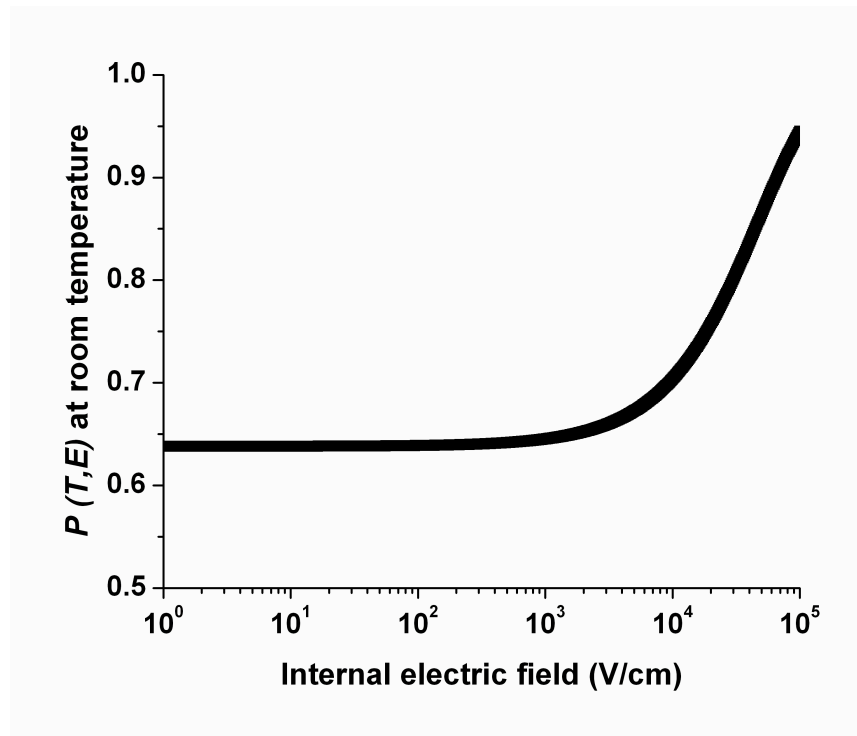


Figure 6-9. Probability of geminate pair separation versus internal electric field.

The geminate pair dissociation efficiency is calculated using the Onsager-Braun model [70] for field-dependent geminate pair dissociation, as described in the Chapter 5.

The parameters used in the model are shown in Table 5-1. Figure 6-9 shows a plot of polaron pair dissociation probability versus internal electric field. Combining the data in Fig. 6-7 and Fig. 6-9, the recombination lifetime is found in the range of $\sim 1\text{-}4\ \mu\text{s}$.

In summary, the transient photoconductivity, forward-to-reverse transient response, and variable field techniques, yield consistent free polaron recombination lifetime $\sim 1\text{-}4\ \mu\text{s}$ for P3HT:PC₆₁BM solar cells. Considering its simplicity and accuracy, transient photoconductivity was selected to characterize the sweep out time and recombination time for four types of polymer: PC₆₁BM solar cells.

6.5 Free polaron collection efficiency for four types of polymer:PCB₆₁M solar cells

In order to characterize the recombination lifetime, voltages from 0 V to a voltage near V_{oc} was applied to each device. The transient photocurrent response for the four types of polymer: PC₆₁BM solar cells are shown in Fig. 6-1. An over-shoot at the rising edge was observed in P3HTT-DPP-10%:PC₆₁BM, P3HTT-TP:PC₆₁BM, and P3HTT-BTD:PC₆₁BM solar cells but not for the P3HT:PC₆₁BM solar cells. The peaks reflect the imbalanced transport in amorphous materials. This could be attributed to trapping or the inherently big difference between electron and hole mobility-lifetime products in these material systems, which perturbs the internal electric field inside the devices[103].

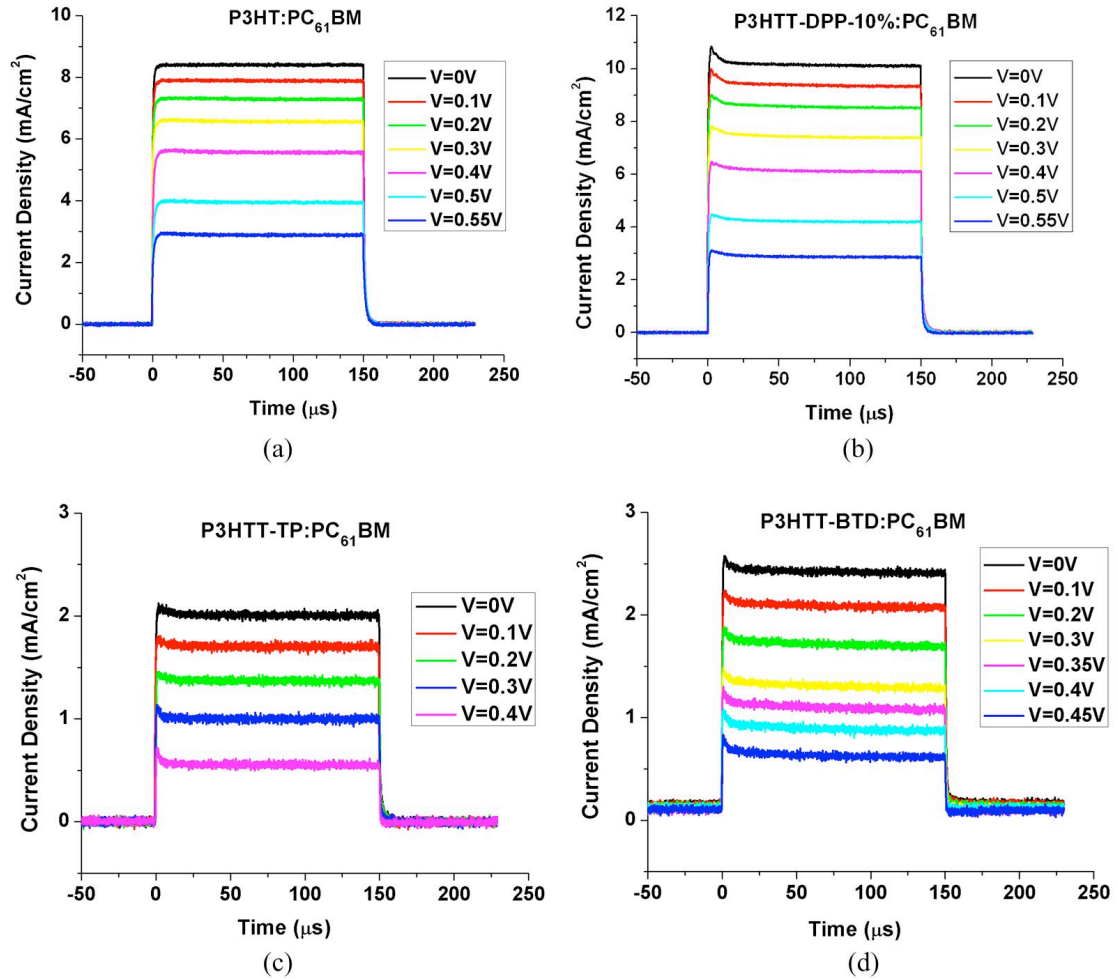


Figure 6-10. Transient photocurrent response of (a) P3HT:PC₆₁BM, (b) P3HTT-DPP-10%:PC₆₁BM, (c) P3HTT-TP:PC₆₁BM and (d) P3HTT-BTD:PC₆₁BM solar cells at different applied bias.

To determine if traps dominate, we also extracted the ideality factors (n) from V_{oc} versus light intensity (I) at room temperature [20]. The light source we use is an AM1.5 solar simulator and different light intensities are realized by the neutral density filter. As shown in Fig. 6-11, V_{oc} changes linearly with $\log_{10}(I)$ and the ideality factor is extracted from fitting the slope = nkT/q . The diode ideality factor phenomenologically describes the exponentiality of the diode dark current in forward bias. In the ideal case (no recombination), n is unity [26]. We observe that $n \gg 1$ for P3HTT-TP:PC₆₁BM, which is

consistent with deep-level trapping in the material [104]. High ideality factors are a characteristic signature of increased recombination loss or increased disorder the electronic states [105]. For P3HTT-BTD:PC₆₁BM solar cells, we observe $n < 1$, which can be due to Auger recombination via trapping sites [26]. For P3HTT-DPP-10%:PC₆₁BM, both ideality factor $n \approx 1$ and longer lifetime indicate that trapping is not significant. Although we still see the over-shoot in the transient photocurrent measurement, this could possibly be due to other factors, such as exciton-exciton annihilation, which still needs more investigation.

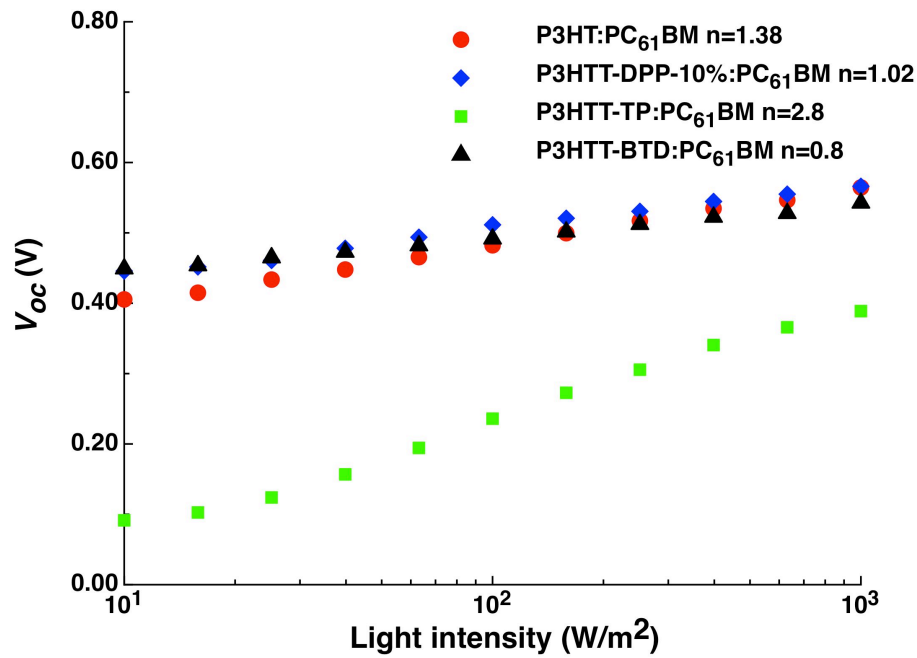


Figure 6-11. V_{oc} vs. light intensity (I) at room temperature.

The recombination time was determined from the $1/e$ decay response time of the transient photocurrent [71, 87]. The transient lifetimes are plotted in Fig. 6-12 versus internal voltage. For P3HT:PC₆₁BM and P3HTT-DPP-10%:PC₆₁BM, the response time, $\tau_{1/e}$, decreases as internal voltage increases in the high internal voltage region. This is due

to the fact that the response time is dominated by the sweep-out time under high electrical field. For lower internal voltage, the voltage dependence is greatly diminished. As the internal voltage approaches zero, recombination dominates and the recombination lifetime for free charges is estimated to be $\sim 0.9 \mu\text{s}$ and $\sim 0.8 \mu\text{s}$ for P3HT:PC₆₁BM and P3HTT-DPP-10%:PC₆₁BM solar cells, respectively. For P3HTT-TP:PC₆₁BM and P3HTT-BTD:PC₆₁BM, the transient response is overwhelmed by the trap-mediated dynamic interplay between the hole extraction and thermionic injection near the contacts [106]. Under low forward bias, the transient response is almost constant owing to the relatively small distortion of the electric field. As the applied voltage increases, charge injection dominates, which is responsible for the subsequent decrease in the transient response. In this case, the recombination lifetime for free charges is $\sim 500 \text{ ns}$ for P3HTT-TP:PC₆₁BM and P3HTT-BTD:PC₆₁BM solar cells.

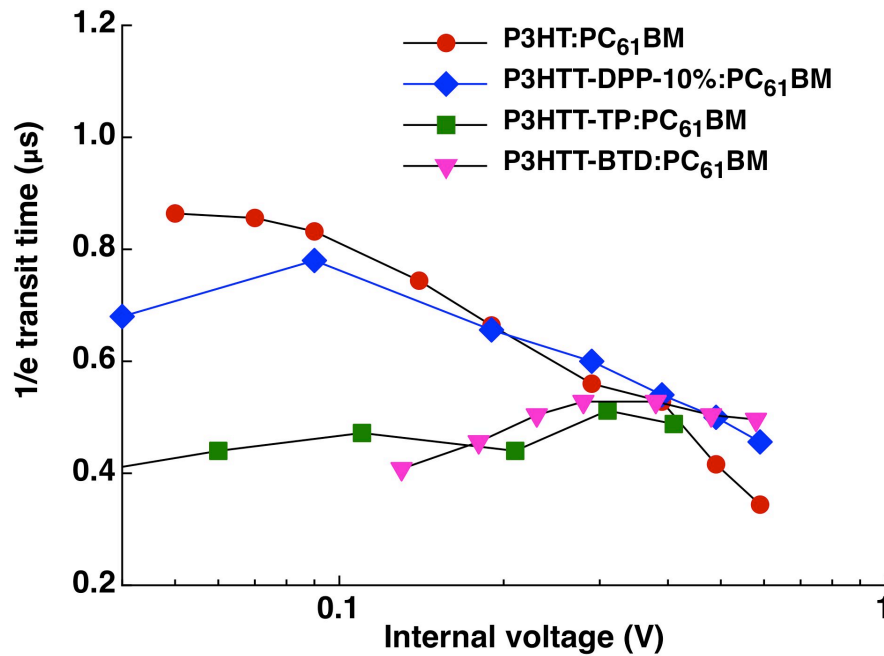


Figure 6-12. The transient lifetimes for different polymer:PC₆₁BM solar cells at different applied bias.

The sweep out time is measured at -2V. From Fig. 6-13, we can see that the sweep out time is extracted from the intersection of the linear fitting lines. Therefore, the sweep out times are 220ns, 270ns, 130ns and 220ns for P3HT:PC₆₁BM, P3HTT-DPP-10%:PC₆₁BM, P3HTT-TP:PC₆₁BM and P3HTT-BTD:PC₆₁BM solar cells, respectively. The charge collection efficiencies then are calculated based on Eq. 6-1, which is shown in Table 6-1. We can see that the short lifetime of free polarons, which reflects the trapping recombination, will affect the polaron collection. This will, in turn, degrade the short circuit current density and the fill factor.

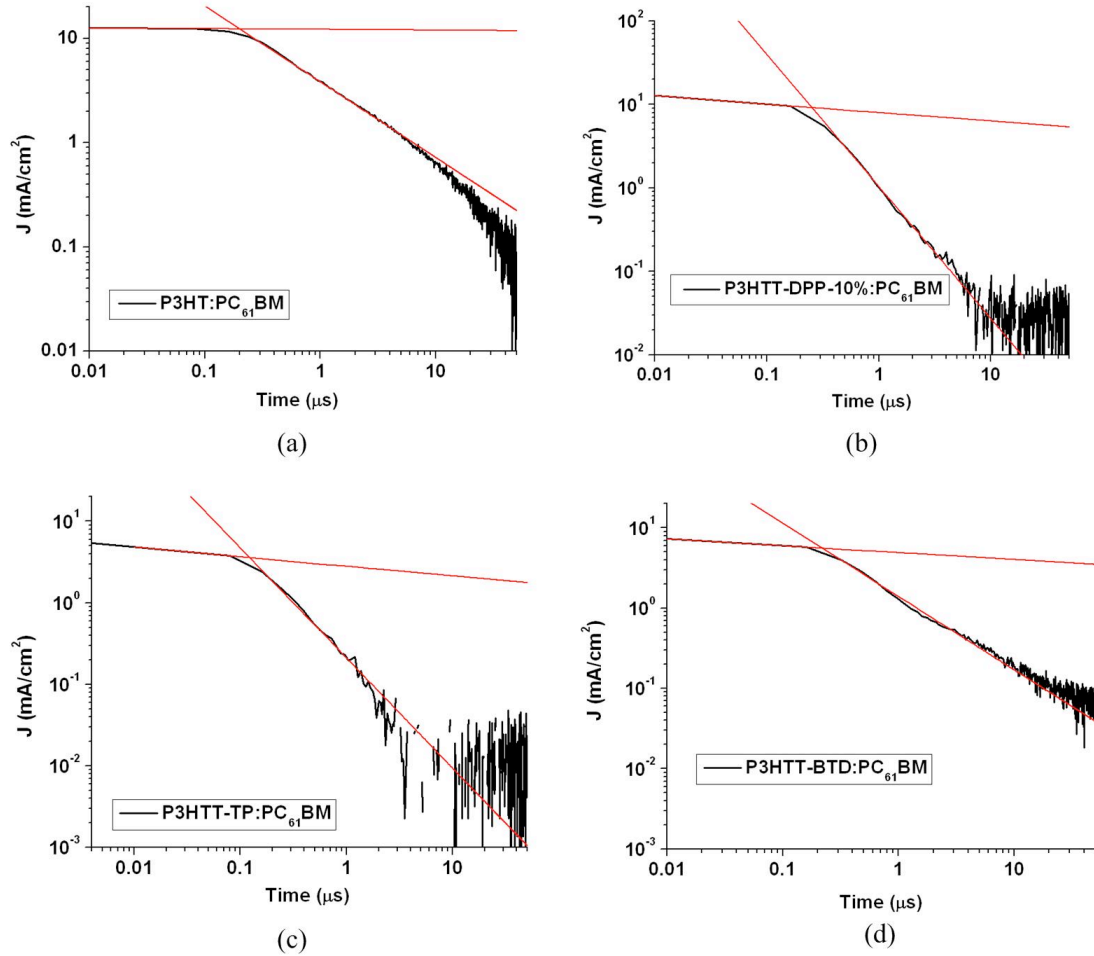


Figure 6-13. Transient photoconductivity measurement for sweep out time. The black lines are transient photoresponse at -2V and the red lines are linear fitting for the black curves. The intersection of two red lines is the sweep out time point.

Table 6-1. Photovoltaic properties and free polaron collection characteristics of four types of polymer:PC₆₁BM solar cells

	t_{sw} (ns)	t_r (ns)	η_{cc} (%)	J_{sc} (mA/cm ²) ^b	FF
P3HT:PC ₆₁ BM	220	900	82.0	8.07	0.58
P3HTT-DPP-10%:PC ₆₁ BM	250	800	76.2	9.99	0.54
P3HTT-TP:PC ₆₁ BM	130	500	79.4	1.90	0.33
P3HTT-BTD:PC ₆₁ BM	220	500	69.4	2.27	0.36

6.6 Thermal annealing effect on mobility and lifetime

For organic BHJ solar cells, thermal annealing plays an important part in the device fabrication and performance. Free charge transport has traditionally been characterized in terms of diffusion and drift lengths[4, 26, 107]

$$L_{drift} = \mu\tau E, \quad (6-9a)$$

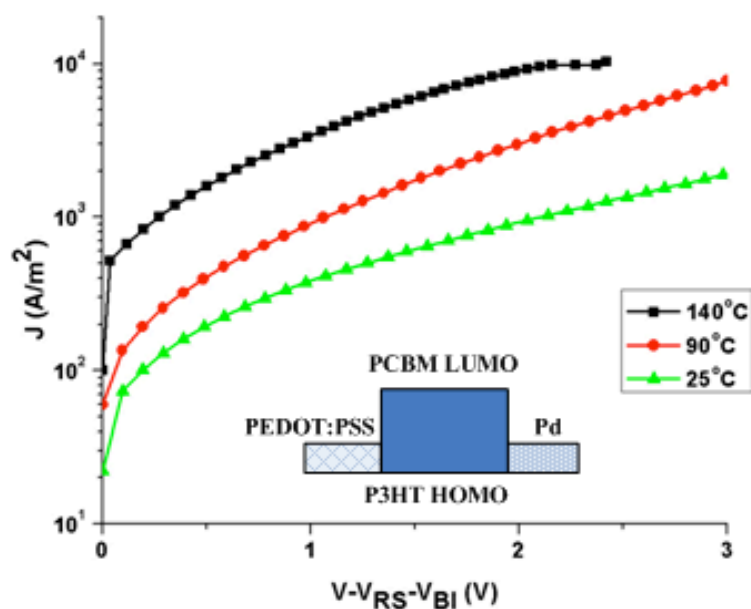
$$L_{diffusion} = \sqrt{D\tau} = \sqrt{\frac{kT}{q}} \mu\tau, \quad (6-9b)$$

where μ is the mobility; τ is the lifetime; E is the internal electric field; D is the diffusion coefficient; and k is the Boltzmann constant. Therefore, the product $\mu\tau$ is a very important characterization parameter. In order to study the thermal annealing effects on charge transport in organic BHJ solar cells, the mobility and lifetime of free charges, as determined by SCLC and transient response technique[97], respectively, were measured for different annealing temperatures in P3HT:PCBM devices.

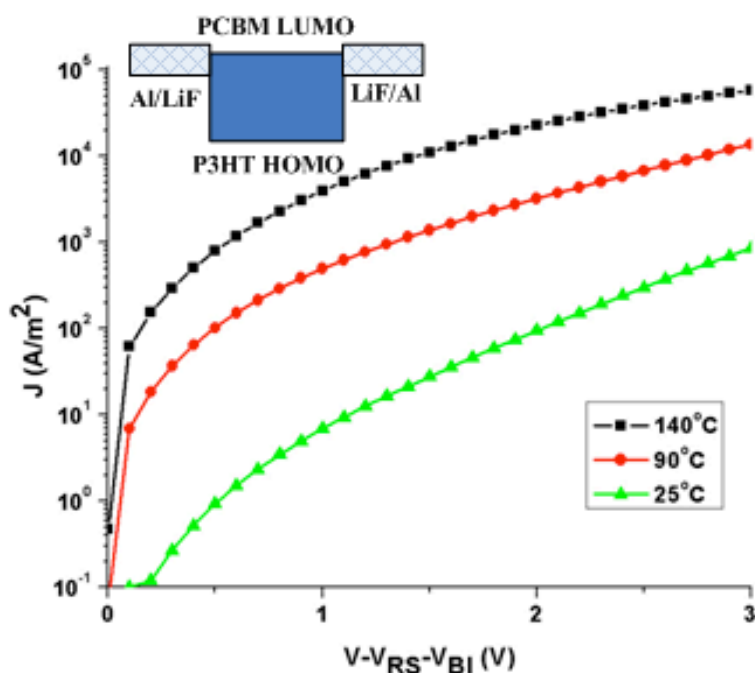
For mobility measurements, to fabricate “hole-only” devices, palladium was evaporated as the top contact for an ITO/ PEDOT:PSS/ P3HT:PCBM structure [46]. For “electron-only” devices, in order to suppress hole injection in P3HT, 1nm LiF/80nm Al layer was used as both top and bottom contacts. The 1nm LiF layer enables the work function of Al to be lowered to 2.8 eV[52]. The structures for hole-only and electron-only devices are shown in the inset of Fig.6-14. As mentioned in chapter 2, the SCL current is approximated by [50]

$$J = \frac{9}{8} \epsilon_0 \epsilon_r \mu_0 \frac{V_a^2}{d^3}, \quad (2-8)$$

where J is the current density; ϵ_0 is the permittivity of free space; ϵ_r is the relative permittivity of the material; μ_0 is the zero-field mobility; V_a is the applied voltage; and L is the thickness of the active layer. The mobilities of electrons and holes were calculated using Eq. 2-8 and are plotted in Fig. 6-14 versus temperature. Both hole and electron mobilities increase with annealing temperature from room temperature up to 140 °C. The increased hole mobility results from the crystallization of P3HT and increased size of the P3HT and PCBM domains [54]. In addition, as temperature increases, the melting of P3HT side-chains allows PCBM molecules to diffuse and form nanocrystalline domains of pure PCBM which results in enhanced electron transport [108]. For annealing temperature above 140 °C, both hole and electron mobility sharply decrease owing to the fact that the fibrils of P3HT decompose into small grains along the fibril axis and the formation of large PCBM aggregates, respectively.

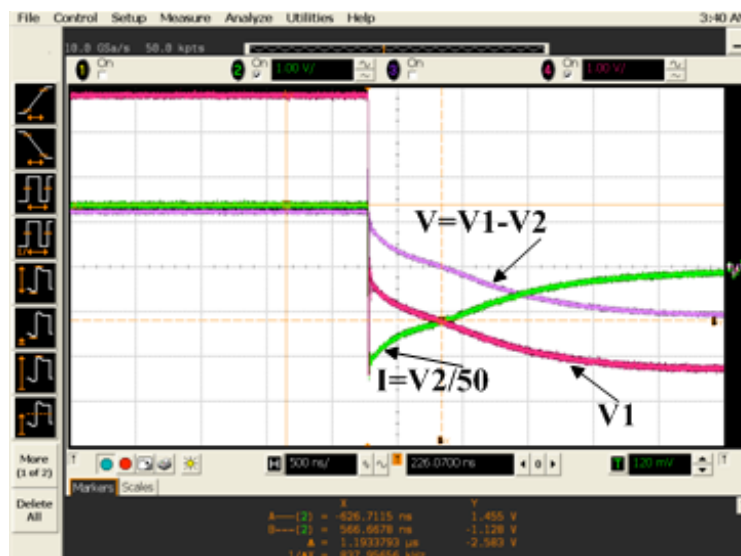


(a)

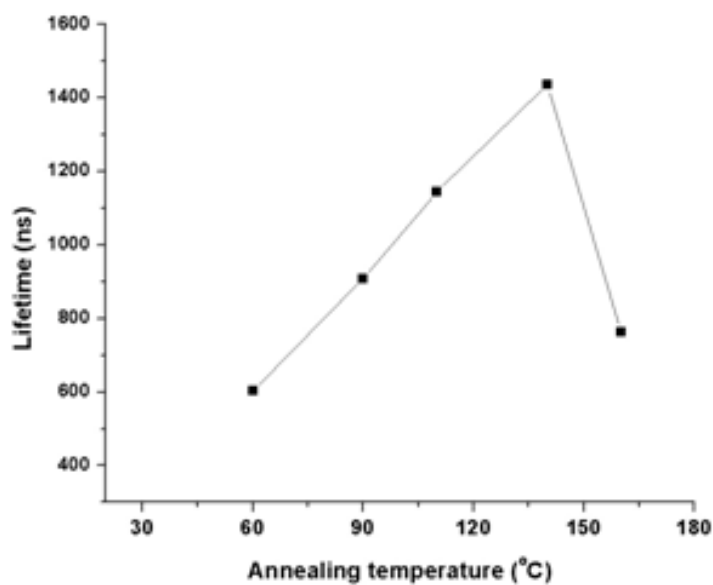


(b)

Figure 6-14. Dark current densities (J) in 55:45 wt. % blends of P3HT:PCBM devices as a function of annealing temperature (a) electron-only device and (b) hole-only device.



(a)



(b)

Figure 6-15. (a) Typical current and voltage switching characteristics of a P3HT:PCBM solar cell and (b) lifetime as a function of annealing temperature.

In order to obtain the free charge recombination lifetime, the forward to reverse transient behavior without illumination was measured. Typical current and voltage

switching characteristics of a P3HT:PCBM solar cell are shown in Fig. 6-15 (a) and the calculated lifetime is plotted versus anneal temperature in Fig. 6-15 (b). The peak of the free polaron lifetime occurs near an annealing temperature of 140 °C. Recombination is a primary determinant of free charge lifetimes in organic solar cells. Since the annealing temperature affects crystallization and morphology of the blend, the recombination rate should also be influenced. The lifetime dependence on annealing temperature may be caused by the change of SRH interfacial states, which process was recently demonstrated to be the dominant recombination process [92, 109] in BHJ solar cells. Using the measured mobility and lifetime results in Figs. 14 and 15, respectively, the mobility-lifetime product is estimated to be $\sim 10^{-9} - 10^{-10} \text{ cm}^2/\text{V}$ for 140 °C annealing temperature. This number is close to $10^{-10} \text{ cm}^2/\text{V}$ that Street et al. [92] obtained using the transient photoconductivity method.

6.7 Summary

In this chapter, three techniques were developed to characterize the free polaron recombination lifetime. These techniques are transient photoconductivity, forward-to-zero transient-current response, and electric field dependent photoresponse techniques. Measurements on P3HT:PCB₆₁M solar cells show that these three measurement techniques yield consistent results. The recombination lifetime for a P3HT:PCB₆₁M solar cell is estimated to be $\sim 1\text{-}4\mu\text{s}$.

Owing to its simplicity and accuracy the transient photoconductivity method was used to characterize the recombination lifetime for four types of polymer: PCB₆₁M solar cells. The recombination lifetimes are 900ns, 800ns, 500ns and 500ns for P3HT:PC₆₁BM,

P3HTT-DPP-10%:PC₆₁BM, P3HTT-TP:PC₆₁BM and P3HTT-BTD:PC₆₁BM solar cells, respectively. For P3HTT-TP:PC₆₁BM and P3HTT-BTD:PC₆₁BM solar cells, the shorter recombination lifetimes reflect the possibility of deep trapping inside the BHJ solar cells. This was confirmed by light intensity dependent Voc measurements. The non-unity ideality factor is consistent with deep trap assisted SRH recombination in P3HTT-TP:PC₆₁BM solar cells, and trap assisted Auger recombination in P3HTT-BTD:PC₆₁BM solar cells. The free polaron collection efficiencies of these solar cell materials have been calculated and compared.

In order to better understand the thermal annealing effect on charge transport, recombination lifetime and mobility for P3HT:PC₆₁BM solar cells were measured for different thermal annealing temperatures. 140°C was shown to be the optimum annealing temperature, since that temperature yields the highest mobility-lifetime product.

Chapter 7. Numerical simulation

7.1 Introduction and methodology

7.1.1 Introduction

At present, there are two widely used device modeling approaches that are used to simulate the characteristics of solar cells [110]: the mesoscopic approach using a Monte Carlo simulator and the macroscopic approach that uses a drift-diffusion model. The Monte Carlo model takes the nanoscale morphology into consideration, but its capabilities are limited to simulation of a few important factors such as exciton dissociation. The substantial computation resources required for the Monte Carlo model limit its utility as a comprehensive predictor of device performance. The drift-diffusion model, on the other hand, is a powerful tool to simulate macroscale parameters, such as V_{oc} , J_{sc} , carrier concentration, and electric potentials, but it fails to adequately account for nanoscale morphology. In this chapter, we focus on analyzing the macroscale parameters using the drift-diffusion model.

The Koster model [30] is a fundamental drift-diffusion numerical model for calculating current-voltage characteristics of polymer:fullerene bulk heterojunction solar cells. It addresses the role of contacts, drift, and diffusion of charge carriers as well as charge carrier generation, and recombination. However, there are several factors that are not considered in this model, e.g., non-uniform photon absorption, non-geminate recombination, and the effect of series resistance, R_s , and shunt resistance, R_{sh} , on fill factor and solar cell power conversion efficiency. In the literature, only one or two factors

are adjusted to the Koster model [55, 110, 111] because other parameters are not well known due to the lack of experimental data.

In this chapter, non-uniform photon absorption, exciton diffusion, non-geminate recombination, and the effects of R_s and R_{sh} are incorporated into the Koster model based on our measurements. Current-voltage curves are simulated for P3HT:PC₆₁BM, P3HTT-DPP-10%:PC₆₁BM, P3HTT-TP:PC₆₁BM and P3HTT-BTD:PC₆₁BM solar cells. The electric field, potential energies, positive polaron and negative polaron current densities, and recombination rates are analyzed under dark, short circuit, and open circuit conditions. Comparison is made and discussed between measured results and simulations.

7.1.2 Device model and numerical method

Device simulation without considering R_s and R_{sh}

As mentioned in Chapter 2, an organic BHJ solar cell can be approximated as an MIM structure. The basic equations used in the simulation are the Poisson equation, and continuity equations for polaron pairs and free polarons. To obtain a unique solution, the boundary conditions for free polaron density and electrical potential need to be specified. It's assumed that the contact between electrodes and the active layer is ohmic. Using Boltzmann statistics, the free polaron densities at the interface between electrodes and the active layer are

$$n(0) = N_{LUMO}, \quad (2-6a)$$

$$p(0) = N_{LUMO} \exp\left(-\frac{\Delta E_{HL}}{kT/q}\right), \quad (2-6b)$$

$$p(d) = N_{HOMO}, \quad (2-6c)$$

$$n(d) = N_{HOMO} \exp\left(-\frac{\Delta E_{HL}}{kT/q}\right), \quad (2-6d)$$

where N_c and N_v are the effective density of states of LUMO level and HOMO level, respectively. E_{gap} is the energy level difference between LUMO and HOMO. Meanwhile, the boundary condition for electrical potential is

$$\psi(d) - \psi(0) = E_{gap} - V_a, \quad (2-7)$$

where V_a is the applied voltage. The numerical simulation has been carried out using Silvaco TCAD organic tools, which utilizes the Newton nonlinear iteration strategy.

In order to characterize the non-uniform exciton generation, the transfer matrix method has been applied on to the organic BHJ solar cells as detailed in Chapter 3. The exciton generation rate $G_{exciton}(\text{cm}^{-3} \text{ s}^{-1})$ as a function of depth is extracted from

$$G_{exciton}(x) = \int \eta_a(x, \lambda) N(\lambda) d\lambda, \quad (7-1)$$

where $\eta_a(x, \lambda)$ is the absorption percentage at a single wavelength at depth x and $N(\lambda)$ is the number of incident photons at a specific wavelength per second. The simulated exciton generation rate was calculated using MATLAB and then imported to the Silvaco C interpreter function file with a BEAM statement and F.RADIATE parameter.

For exciton diffusion calculation, a factor of η_{ed} is added to Eq. 2-5, which yields

$$\frac{1}{q} \frac{\partial}{\partial x} J_n = (1 - P_{diss}) R - P_{diss} \eta_{ed} G_{exciton}. \quad (4-2)$$

This modification is included in the BEAM statement b1 in the Silvaco program.

As discussed in Chapter 6, several mechanisms contribute to non-geminate recombination; these include band-to-band recombination, monomolecular recombination through Shockley-Read-Hall (SRH) recombination at the heterojunction interface, and

reverse-diffuse recombination through contacts. Based on our recombination lifetime experiments and light intensity versus V_{oc} measurements, we have included trap-assisted SRH recombination in the P3HTT-TP:PC₆₁BM solar cell model. SRH recombination, first derived by Shockley and Read[112] and then by Hall [113], occurs through deep-level traps accompanied by phonon scattering. Recently, a theory for the SRH recombination rate has been developed for polymer solar cells [7]; it can be expressed as

$$R_{SRH} = \frac{(pn - n_i^2)}{N_t \left(\frac{n + n_i \exp(\frac{E_{trap}}{kT_L})}{C_p} + \frac{p + p_i \exp(-\frac{E_{trap}}{kT_L})}{C_n} \right)}, \quad (7-3)$$

where N_t is the density of traps, C_p and C_n are capture coefficients, E_{trap} is the difference between the trap energy level and the intrinsic Fermi level, and T_L is the lattice temperature. The SRH recombination rate has been added to both polaron pair and free polaron continuity equations in the Silvaco TCAD simulation. For P3HTT-BTD:PC₆₁BM solar cells, trap-assisted Auger recombination is introduced into the model. Auger recombination occurs through a three particle transition where a mobile carrier is either captured or emitted [114]. The Auger recombination rate is usually described as[115]

$$R_{auger} = C_{AUGN}(pn^2 - nn_i^2) + C_{AUGP}(np^2 - pn_i^2), \quad (7-4)$$

where C_{AUGN} and C_{AUGP} are the capture coefficients for negative polarons and positive polarons, respectively. Here, the Auger recombination rate is added to both polaron pair and free polaron continuity equations in the Silvaco TCAD simulation.

I-V simulation including R_s and R_{sh}

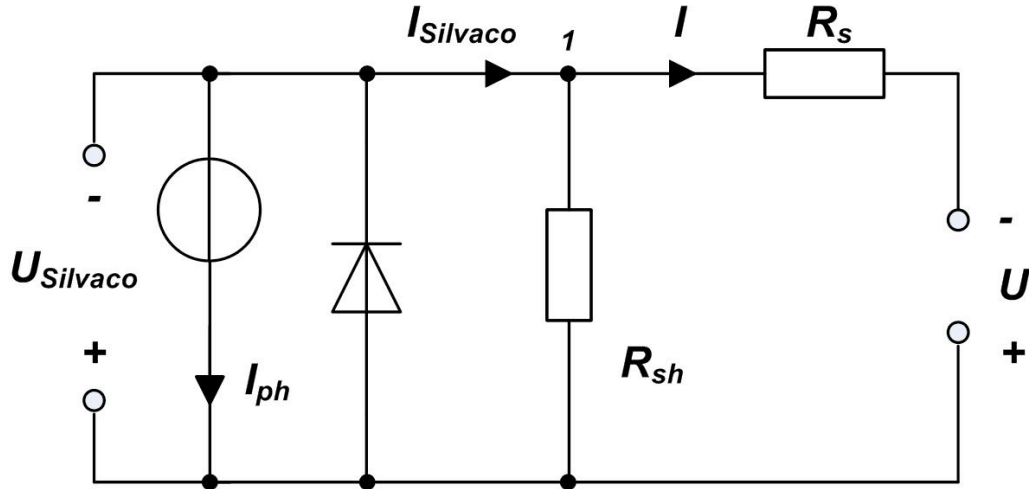


Figure 7-1. An equivalent circuit for a real solar cell.

In fact, the series resistance and shunt resistance are two important parameters that can not be omitted when fitting I-V curves. An equivalent circuit for a solar cell is shown in Fig.7-1 [4]. Generally, the I-V characteristic is described as

$$I = I_0 \left(e^{\frac{q}{nKT}(U - IR_s)} - 1 \right) + \frac{U - IR_s}{R_{sh}} - I_{ph} \quad (7-5)$$

where n is the ideality factor, I_0 is the saturation current, U is applied voltage on the device and I_{ph} is the photocurrent. For organic BHJ solar cells, analytical solutions obtained by deriving the I-V characteristics from the Poisson equation and the continuity equations have not provided good fits to experimental results. As a result, simulations have been pushed toward numerical solutions. Using Kirshoff's current law and voltage law [116], the current at node 1 in Fig. 7-1 follows

$$I = I_{Silvaco} + \frac{U_{Silvaco}}{R_{sh}}, \quad (7-5a)$$

and the applied voltage on the device is

$$U = U_{\text{SILVACO}} + R_s I, \quad (7-5b)$$

where I and U are the simulated current and voltage including a series resistance and a shunt resistance, I_{Silvaco} and U_{Silvaco} are the simulated current and voltage by Silvaco. Given a series resistance and a shunt resistance, the experiment I-V curve can be fitted. We want to note here this method is similar to the Simulation Program with Integrated Circuit Emphasis (SPICE) dc simulation [117]. SPICE is a general-purpose circuit simulation program for dc, transient and linear ac analysis. In the SPICE netlist, analysis modes and circuit description including device information need to be defined. Device information syntax in the netlist is typically linked to a device property file which includes device configuration and important electrical parameters. When a SPICE simulation is running, the device property file will be called and used in the main program. Here, our MATLAB main program is like SPICE and the Silvaco device simulation output file is like the device property file in the SPICE.

Simulation parameters

The simulation parameters are listed in Table 7-1 to Table 7-4 for P3HT:PC₆₁BM, P3HTT-DPP-10%:PC₆₁BM, P3HTT-TP:PC₆₁BM and P3HTT-BTD:PC₆₁BM solar cells, respectively. The bandgap is calculated from the difference between the HOMO level of the PC₆₁BM and the LUMO level of the polymer. The HOMO level for PC₆₁BM is 3.8 eV [111] and the LUMO levels for P3HT, P3HTT-DPP-10%, P3HTT-TP and P3HTT-BTD are 5.1eV [32], 5.2eV [32], 5.23eV [31] and 5.41eV [31], respectively. The exciton diffusion efficiency is extracted from I-V curve under the large reverse bias, as it is described in Table 4-1.

As it is shown in Table 5-1, the dielectric constants were extracted from the geometrical capacitance of the solar cells and the mobility were measured by the space charge limited current methods. The initial separation of polaron pair for P3HT is set to 1.9nm [78]. Based on the grazing-incidence X-ray diffraction (GIXRD) results [31, 32], the P3HTT-DPP-10% and P3HTT-BTD show the similar interchain distance as P3HT. Therefore the initial separations of polaron pair for them are both set to 1.9nm. For P3HTT-TP, on the other hand, seems to be completely amorphous by GIXRD study. As a comparison with three other polymers, we set the initial separations of polaron pair as 1.8nm.

The density of states of the polymers and PC₆₁BM, the polaron pair decay rate, series resistance and shunt resistance are calculated for the best fittings of I - V curves. This is because V_{oc} is strongly affected by polaron pair decay rate, the density of states of the HOMO level of PC₆₁BM and the LUMO level of the polymers, as V_{oc} is described as

$$V_{oc} = \frac{\Delta E_{HL}}{q} - \frac{kT}{q} \ln\left(\left(\frac{k_r}{k_{diss}}\right) \frac{k_{rec} N_{HOMO} N_{LUMO}}{J_x / a_0}\right). \quad (1-1)$$

Meanwhile, shape of I - V curves is influenced by series resistance, shunt resistance and polaron pair decay rate.

7.2 Simulation results for P3HT:PC₆₁BM solar cells

7.2.1 Photon generation rate and simulation parameters

The photon generation rate has been calculated by MATLAB and is shown versus distance from the surface in Fig.7-2. The exciton diffusion efficiency is arbitrarily set to

1, as stated in chapter 4.3. The parameters used in the simulation are shown in Table 7-1.

The temperature was set to room temperature.

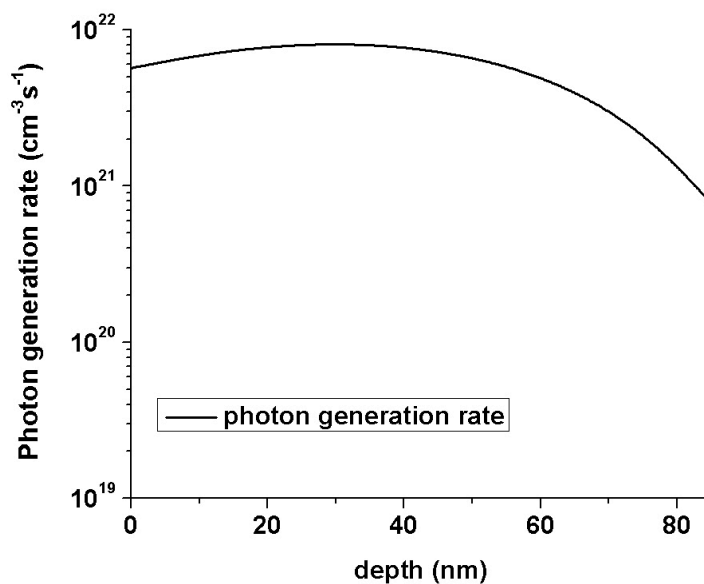


Figure 7-2. Photon generation rate for P3HT:PC₆₁BM solar cells.

Table 7-1. Simulation parameters for P3HT:PC₆₁BM solar cells.

parameter	value	parameter	value
Bandgap (eV)	1.4	Dielectric constant	3.4
Negative free polaron mobility (cm ² /Vs)	2×10 ⁻³	Positive free polaron mobility (cm ² /Vs)	2.8×10 ⁻⁴
Density of State $N_{HOMO}=N_{LUMO}$ (cm ⁻³)	1×10 ²³	Polaron pair decay rate (1/s)	5×10 ⁵
Initial separation of polaron pair (nm)	1.9	Exciton diffusion efficiency (%)	1
Sheet resistance (Ω)	50	Shunt resistance (kΩ)	10

7.2.2 I-V curve simulation including R_s and R_{sh}

The comparison between experiment data and simulation results are plotted in Fig. 7-3. The dark curve is measured and the blue curve is the simulation data extracted from Silvaco. The red dots curve is the simulation that includes the series and shunt resistances. Figure 7-6 shows good agreement between experiment and the simulation with R_s and R_{sh} . This demonstrates the affect of R_s and R_{sh} on the fill factor.

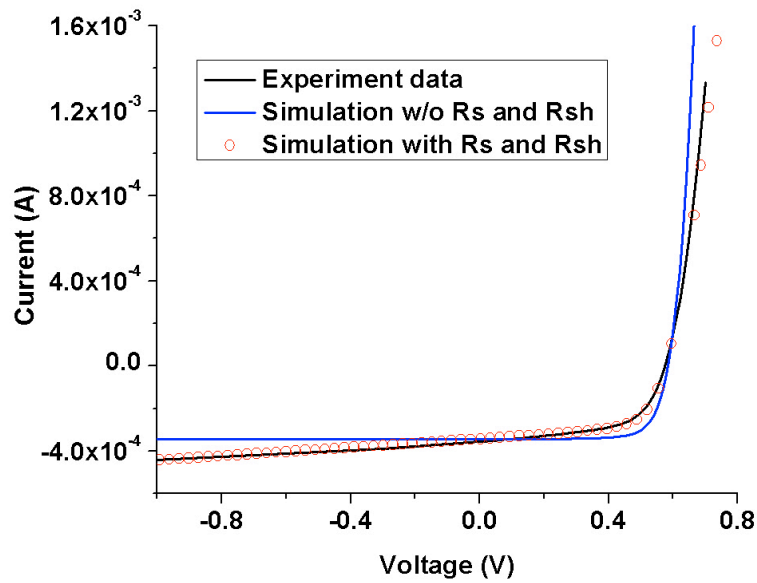


Figure 7-3. Comparison between experimental data and simulation results for P3HT:PC₆₁BM solar cells.

7.2.3 Short circuit condition, open circuit condition, and maximum power condition

Having determined the open circuit voltage and the max power point, the electric potential, electric field, recombination rate, and current densities have been simulated at short circuit condition, open circuit condition, and maximum power condition. In order to better know the device operating conditions, the open circuit point and maximum power

point are extracted from the experimental data. Here, the open circuit voltage is 0.577 V and the maximum power point occurs at 0.45 V.

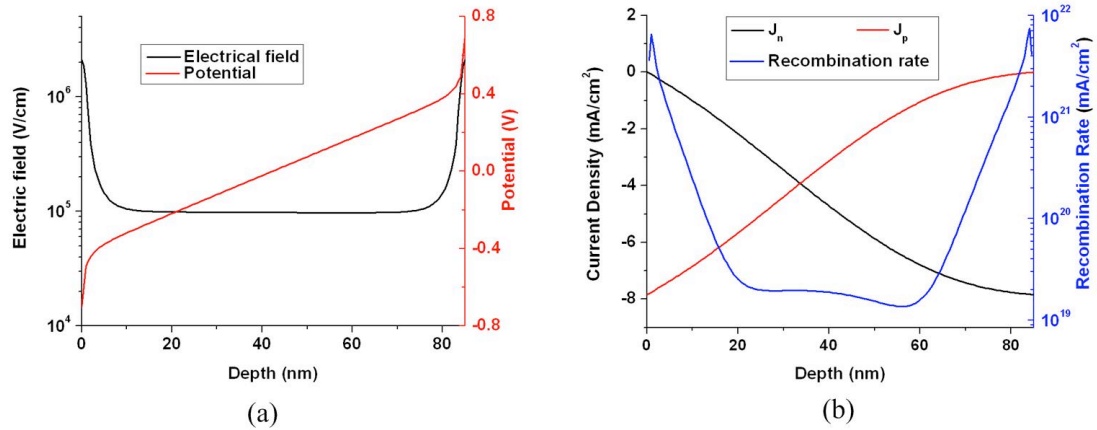


Figure 7-4. Electric potential, electric field, recombination rate and current densities at short circuit condition.

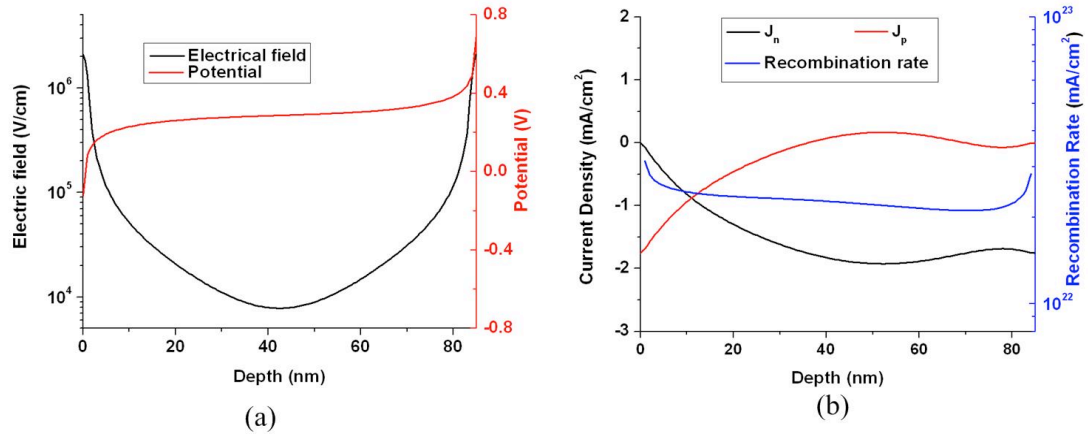


Figure 7-5. Electric potential, electric field, recombination rate and current densities at open circuit condition.

Fig. 7-4 to Fig. 7-6 show that the electric field is almost constant in the middle of the active layer at short circuit condition and the maximum power condition, while the field

near the contact is very high. This demonstrates that tunneling is more probably near the contact. The electric field in the middle of the active layer is almost equal to

$$E = (V_{oc} - V_a)/d, \quad (4-2)$$

which confirms our assumption for the electric field in chapter 4.2. Under the open circuit condition, the electric field exhibits large variation with depth. Thus, Eq. 4-2 is invalid everywhere in the active layer. Fig. 7-7 shows the electric field changes with applied voltage for P3HT:PC₆₁BM solar cells. The electric field near the contacts is always high at all applied voltages, while the electric field in the middle of the active layer decreases largely with voltage increases. For other three polymer: PC₆₁BM solar cells, the trend of electric field vs. applied voltage is similar, as it is shown in Fig. 13, Fig.19 and Fig.25. This is because the boundary conditions for free polaron density and electric potential are under the same assumptions for all the solar cells.

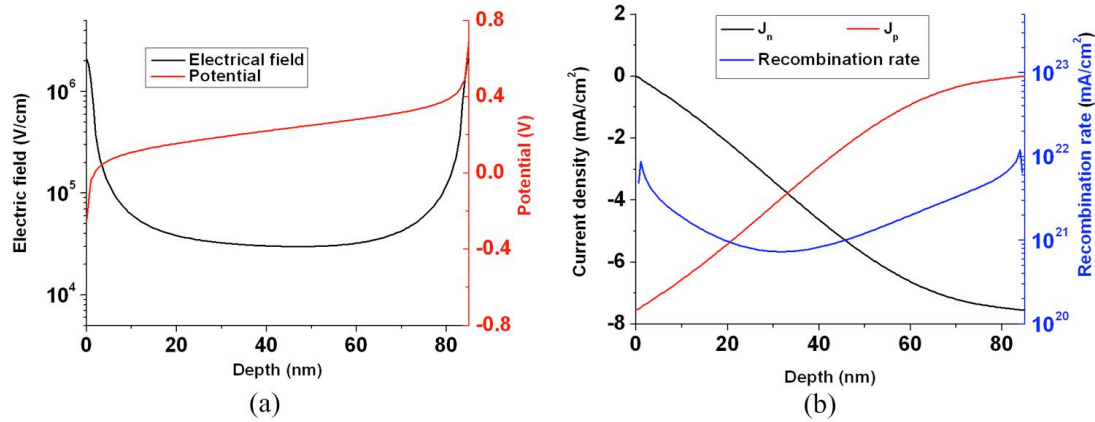


Figure 7-6. Electric potential, electric field, recombination rate and current densities at maximum power condition.

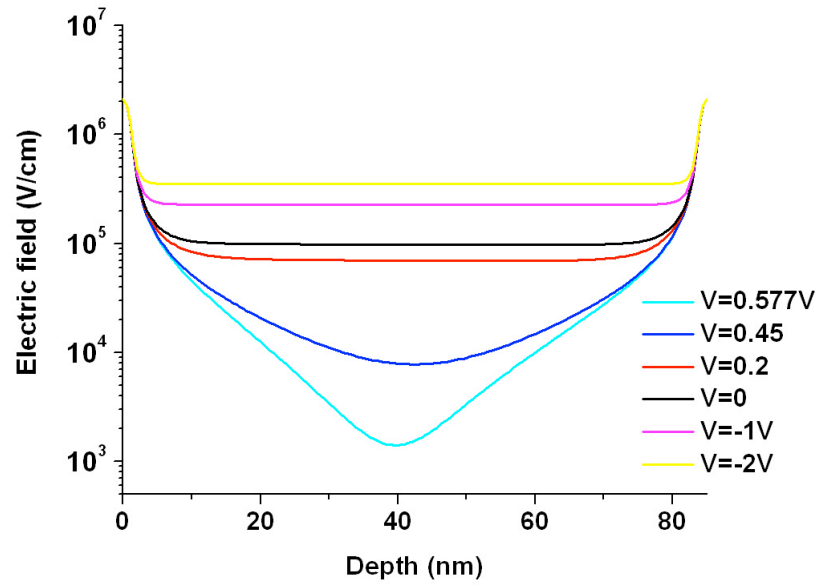


Figure 7-7. Electric field at different applied bias for P3HT:PC₆₁BM solar cells.

The electric potentials at the contacts satisfy the boundary conditions and they are spatially symmetric inside the active layer. The recombination rate changes dramatically at different conditions; it becomes larger as the internal voltage approaches to zero. At short circuit condition, the recombination rate at the contact is ~ 3 orders of magnitude larger than that in the middle of the active layer. This is due to the large density of free polarons at the contacts and the fact that the recombination rate is linearly proportional to $np - n_i^2$.

7.3 Simulation results for P3HTT-DPP-10%:PC₆₁BM solar cells

7.3.1 Photon generation rate and simulation parameters

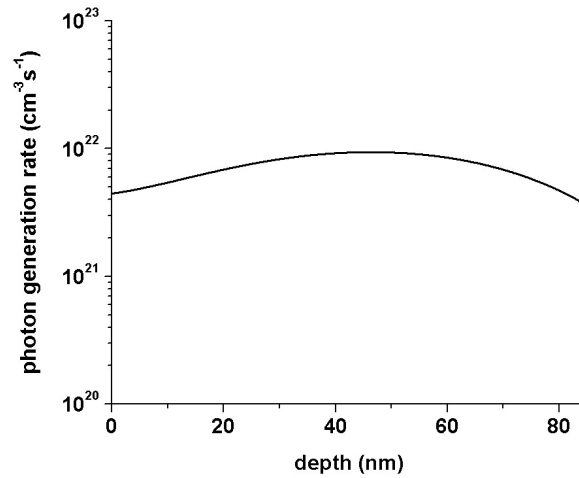


Figure 7-8. Photon generation rate for P3HTT-DPP-10%:PC₆₁BM solar cells.

Table 7-2. Simulation parameters for P3HTT-DPP-10%:PC₆₁BM solar cells.

parameter	value	parameter	value
Bandgap (eV)	1.4	Dielectric constant	3.4
Negative free polaron mobility (cm ² /Vs)	2×10^{-3}	Positive free polaron mobility (cm ² /Vs)	2.3×10^{-4}
Density of State $N_{HOMO}=N_{LUMO}$ (cm ⁻³)	1×10^{23}	Polaron pair decay rate (1/s)	6×10^5
Initial separation of polaron pair (nm)	1.9	Exciton diffusion efficiency (%)	1
Sheet resistance (Ω)	40	Shunt resistance (k Ω)	10

The photon generation rate has been calculated using MATLAB and is shown versus distance from the surface in Fig.7-8. The exciton diffusion efficiency is arbitrarily set to 1, as stated in Chapter 4.3. The parameters used in the simulation are shown in Table 7-1. The temperature was set to room temperature.

7.3.2 I-V curve simulation including R_s and R_{sh}

The measured and simulated current-voltage curves are shown in Fig. 7-9. The dark curve is measured and the blue curve is the simulation data extracted from Silvaco. The red dots curve is the simulation that includes the series and shunt resistances. There is good agreement between experiment results and simulation results with R_s and R_{sh} considerations. Compared with a P3HT:PC₆₁BM solar cell, the series resistance of a P3HTT-DPP-10%:PC₆₁BM solar cell is 10 Ω lower and the shunt resistance is the same.

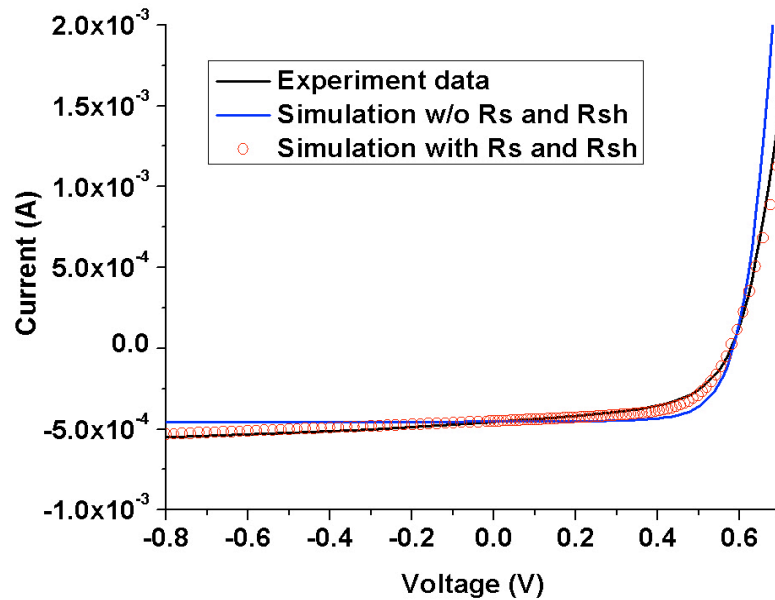


Figure 7-9. Comparison between experiment data and simulation results for P3HTT-DPP-10%:PC₆₁BM solar cells.

7.3.3 Short circuit condition, open circuit condition, and maximum power condition

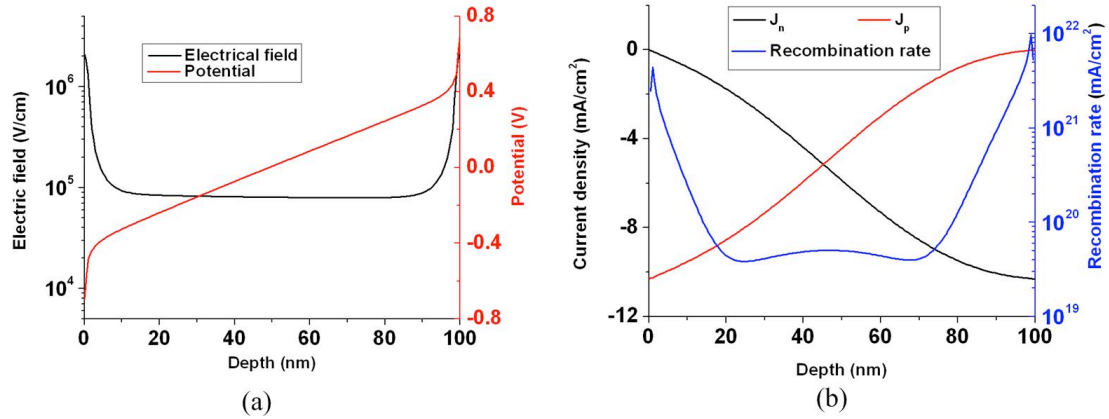


Figure 7-10. Electric potential, electric field, recombination rate and current densities at short circuit condition.

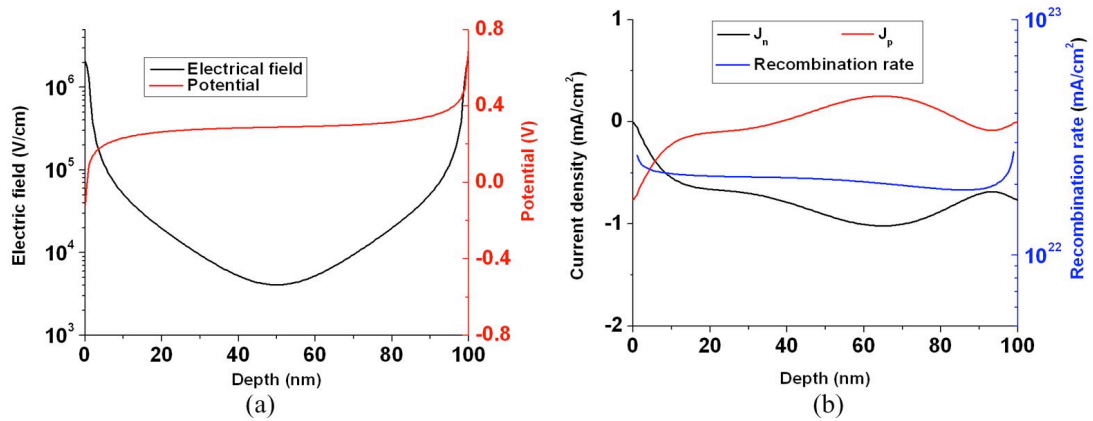


Figure 7-11. Electric potential, electric field, recombination rate and current densities at open circuit condition.

The calculated electric potential, electric field, recombination rate, and current densities at short circuit condition, open circuit condition and maximum power condition are depicted in Fig.7-10 to Fig. 7-12, respectively. The open circuit voltage is 0.579 and

the maximum power condition is at 0.44V. The electric field vs. applied voltage is shown in Fig. 7-13. Compared with the P3HT:PC₆₁BM solar cells, the electric field, electric potential, recombination rate, and current densities for P3HTT-DPP-10%:PC₆₁BM solar cells show similar trends.

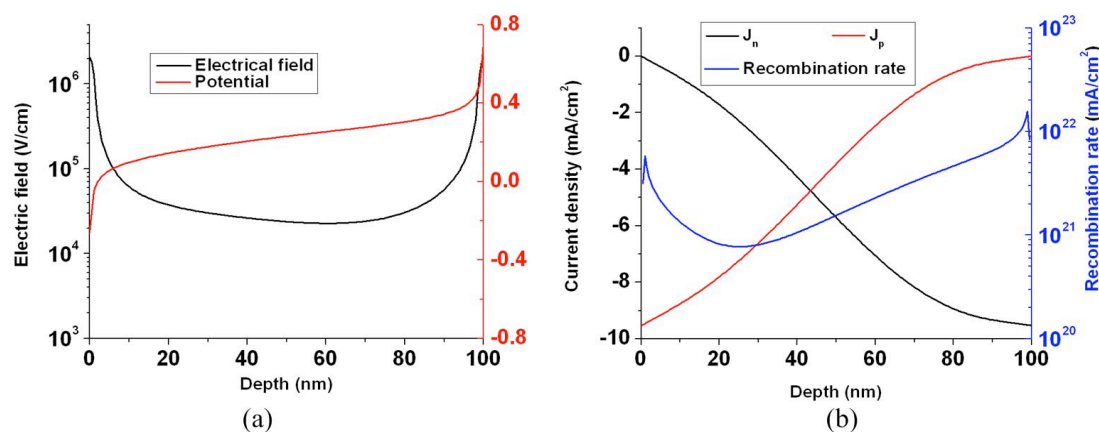


Figure 7-12. Electric potential, electric field, recombination rate and current densities at maximum power condition.

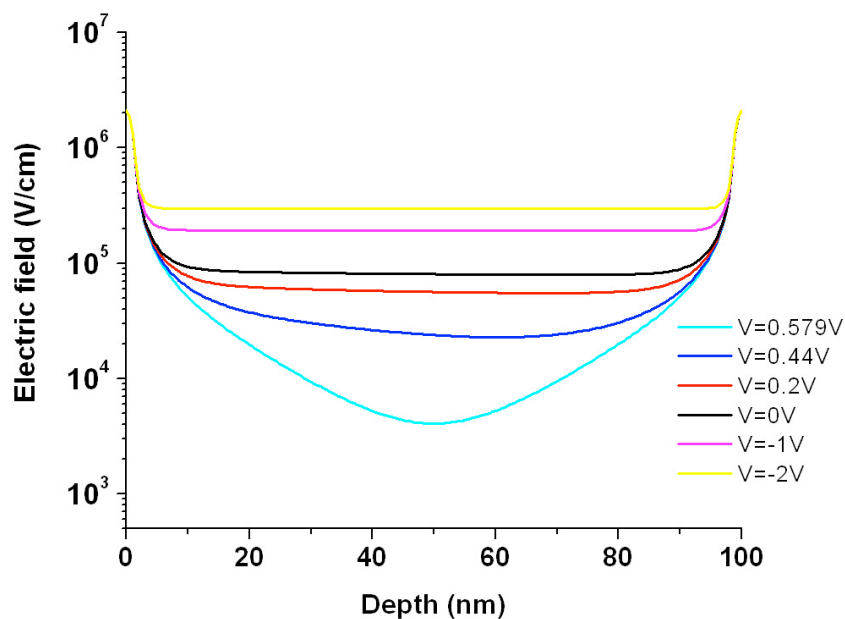


Figure 7-13. Electric field at different applied bias for P3HTT-DPP-10%:PC₆₁BM solar cells.

7.4 Simulation results for P3HTT-TP:PC₆₁BM solar cells

Table 7-3. Simulation parameters for P3HT:PC₆₁BM solar cells.

parameter	value	parameter	value
Bandgap (eV)	1.43	Dielectric constant	3
Negative free polaron mobility (cm ² /Vs)	2×10^{-3}	Positive free polaron mobility (cm ² /Vs)	2.5×10^{-4}
Density of State $N_{HOMO}=N_{LUMO}$ (cm ⁻³)	8×10^{23}	Polaron pair decay rate (1/s)	7.1×10^5
Initial separation of polaron pair (nm)	1.9	Excition diffusion efficiency (%)	33
Energy level difference between traps and HOMO/LUMO (eV)	0.19	Capture coefficient $C_p=C_n$ (s ⁻¹)	1×10^{-8}
Trap density (cm ⁻³)	1×10^{10}	Lattice temperature (K)	297
Sheet resistance (Ω)	150	Shunt resistance (Ω)	550

7.4.1 Photon generation rate and simulation parameters

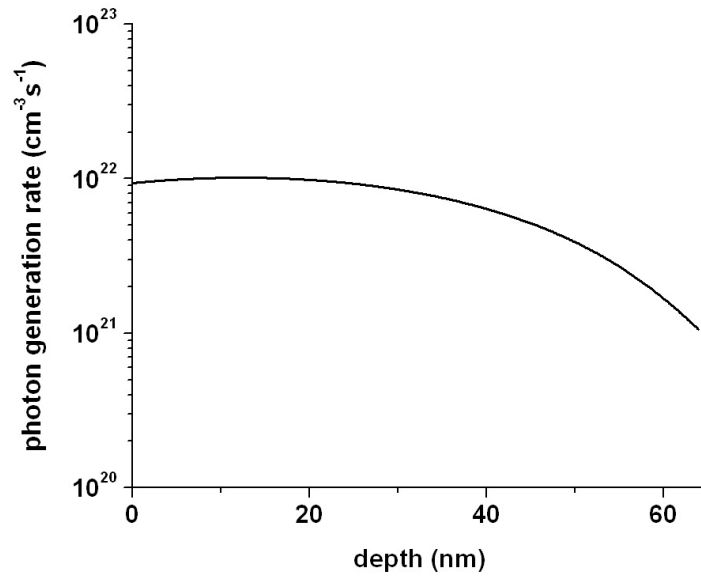


Figure 7-14. photon generation rate for P3HTT-TP:PC₆₁BM solar cells.

The photon generation rate has been calculated by MATLAB and is shown versus distance from the surface in Fig.7-14. The exciton diffusion efficiency is arbitrarily set to 1, as stated in chapter 4.3. The parameters used in the simulation are shown in Table 7-3. The temperature was set to room temperature.

7.4.2 I-V curve simulation including R_s and R_{sh}

The measured and simulated current-voltage curves are plotted in Fig. 7-15. For the P3HTTP:PC₆₁BM solar cells, a large series resistance and small shunt resistance are observed. The large series resistance is primarily due to two reasons [25]: interfaces between the active layer and the contacts, and the charge transport process. The resistance between the active layer and the contacts originates from the energy alignment at the interface, which will affect the interface charge transfer. On the other hand, the charge transport process inside the active layer also contributes significantly to the series resistance. Usually, thicker active layer devices are limited by incomplete collection of photogenerated charges [118], which results in a big series resistance. Here, although the active layer of a P3HTTP:PC₆₁BM solar cell is only ~ 64 nm, the shorter recombination time and the presence of the deep traps may ultimately inhibit charge transfer and thus the series resistance.

The shunt resistance typically reflects the leakage of the diode. The leakage becomes significant if the contact materials form complexes at localized points or non-uniformity in interfacial layers is present. These conditions can result in local variations in contact work functions, which will result in single carrier injection and give rise to leakage current [119].

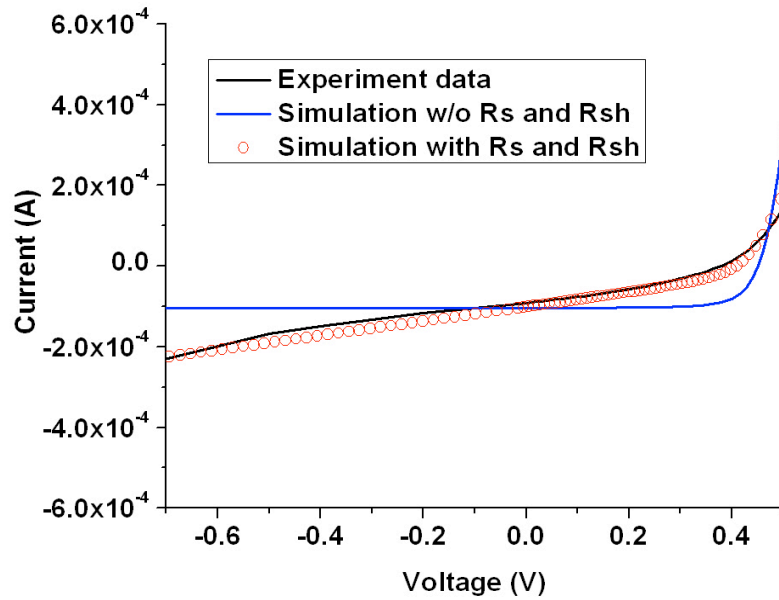


Figure 7-15. Comparison between experiment data and simulation results for P3HTTP:PC₆₁BM solar cells.

7.4.3 Short circuit condition, open circuit condition, and maximum power condition

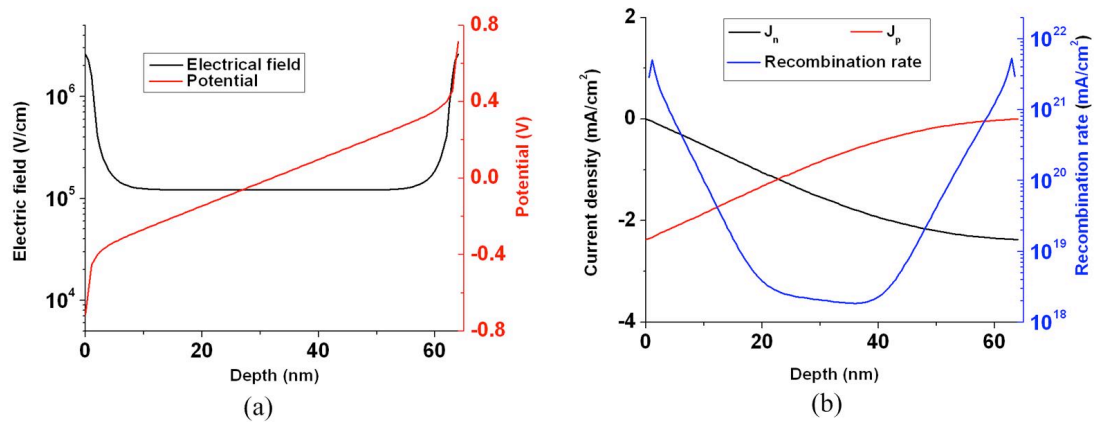


Figure 7-16. Electric potential, electric field, recombination rate, and current densities at short circuit condition.

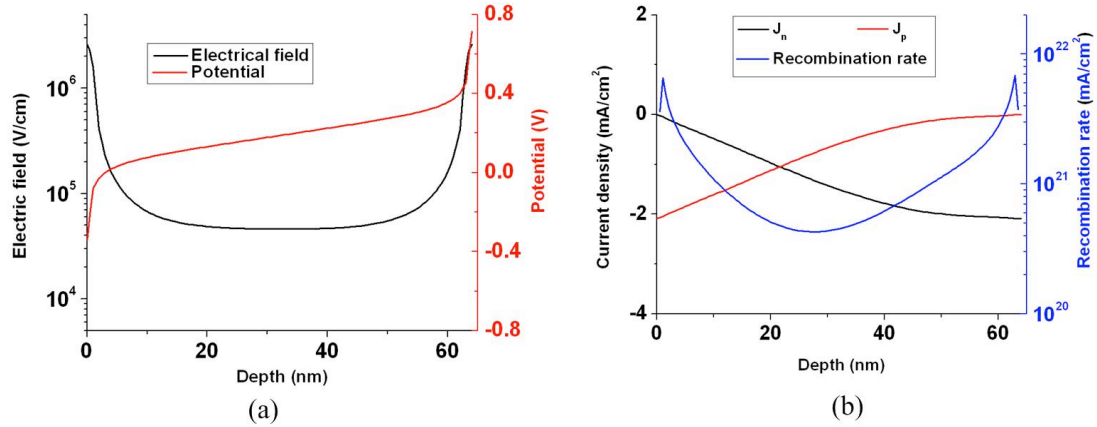


Figure 7-17. Electric potential, electric field, recombination rate, and current densities at open circuit condition.

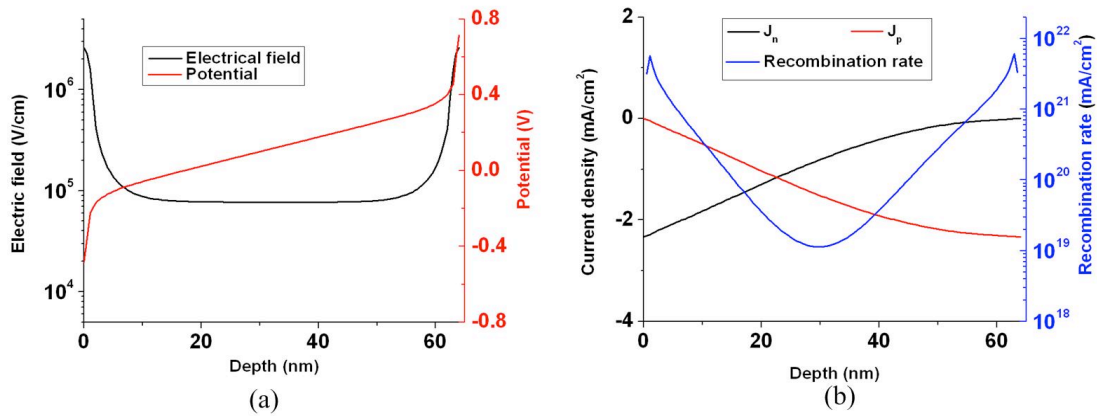


Figure 7-18. Electric potential, electric field, recombination rate, and current densities at maximum power condition.

The calculated electric potential, electric field, recombination rate and current densities at short circuit condition, open circuit condition and maximum power condition are depicted in Fig.7-16 to Fig. 7-18, respectively. The open circuit voltage is 0.373V and the maximum power condition is at 0.23V. The electric field vs. applied voltage is shown in Fig. 7-19. Compared with P3HT: PC61BM solar cells, the electric field under open circuit condition shows a constant value throughout most of active region. The

recombination rate is even lower than that of P3HT: PC61BM solar cells at open circuit condition. This is due to the lower polaron pair generation rate and higher intrinsic carrier density.

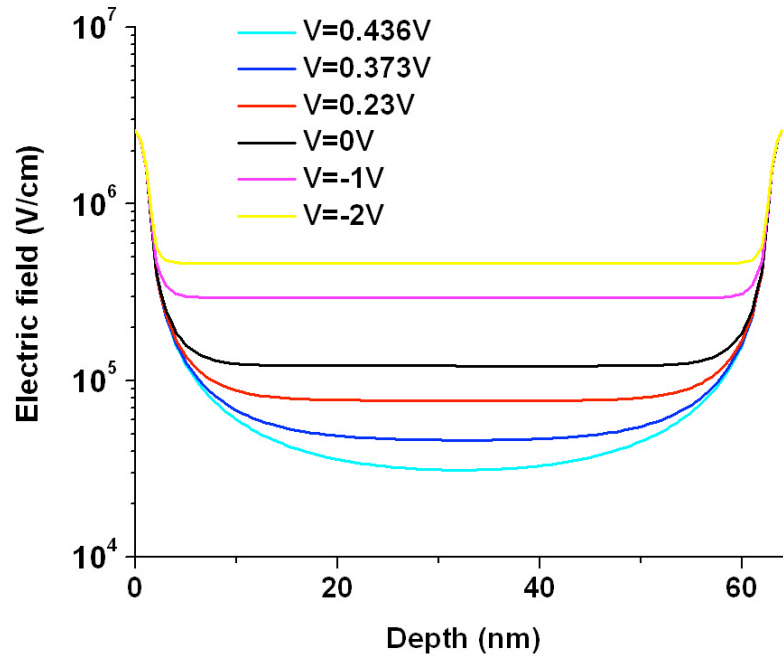


Figure 7-19. Electric field at different applied bias for P3HTT-DPP-10%:PC₆₁BM solar cells.

7.5 Simulation results for P3HT-BTD:PC₆₁BM solar cells

7.5.1 Photon generation rate and simulation parameters

The photon generation rate has been calculated by MATLAB and is shown versus distance from the surface in Fig.7-21. The exciton diffusion efficiency was set to 0.69, as stated in chapter 4.3. The parameters used in the simulation are shown in Table 7-4. As mentioned earlier, in addition to Langevin recombination, trap-assisted Auger

recombination is also included in the model. The temperature was set to room temperature.

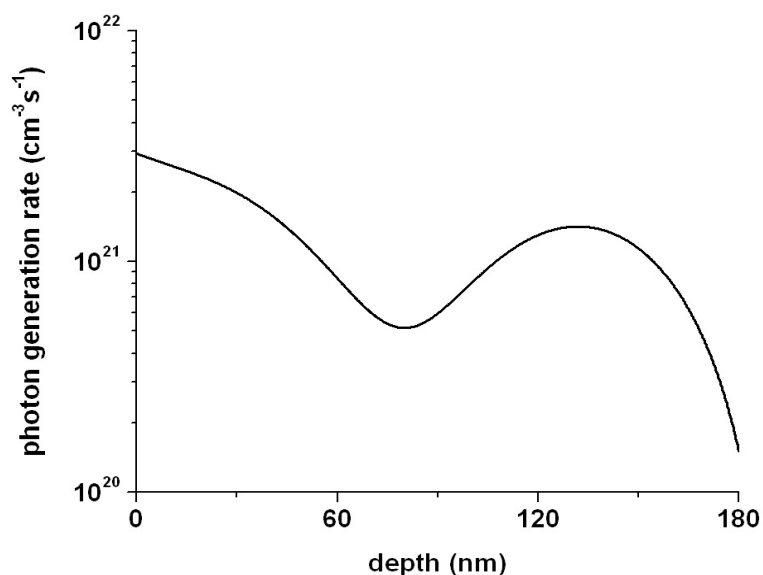


Figure 7-20. Photon generation rate for P3HT:PC₆₁BM solar cells.

Table 7-4. Simulation parameters for P3HTT-BTD:PC₆₁BM solar cells.

parameter	value	parameter	value
Bandgap (eV)	1.61	Dielectric constant	3.4
Negative free polaron mobility (cm ² /Vs)	2×10^{-3}	Postive free polaron mobility (cm ² /Vs)	2.1×10^{-4}
Density of State $N_{HOMO}=N_{LUMO}$ (cm ⁻³)	1×10^{24}	Polaron pair decay rate (1/s)	5×10^6
Initial separation of polaron pair (nm)	1.9	Excition diffusion efficiency (%)	69.6
Auger capture coefficient for negative polaron (cm ⁶ /s)	0	Auger capture coefficient for positive polaron (cm ⁶ /s)	9.9×10^{-32}
Sheet resistance (Ω)	75	Shunt resistance (k Ω)	10.4

7.5.2 I-V curve simulation including R_s and R_{sh}

The measured and simulated current-voltage curves are plotted in Fig. 7-20. The dark curve is measured and the blue curve is the simulation data extracted from Silvaco. The red dots curve is the simulation that includes the series and shunt resistances. The simulation curve that includes the series and shunt resistances (red circles) provides a better fit to the measured curve than the simulation without series and shunt resistance (blue curve). The sheet resistance is a little higher than that of a P3HT:PC₆₁BM and the shunt resistance is almost the same. Compared to P3HTT-TP:PC₆₁BM solar cells, the series resistance is 2 times smaller than that of a P3HTT-TP:PC₆₁BM solar cell. That means although we see a smaller recombination time and a non unity ideality factor for P3HTT-BTD:PC₆₁BM solar cells, the influence of charge transport on series resistance is not that significant as that on P3HTT-TP:PC₆₁BM solar cells.

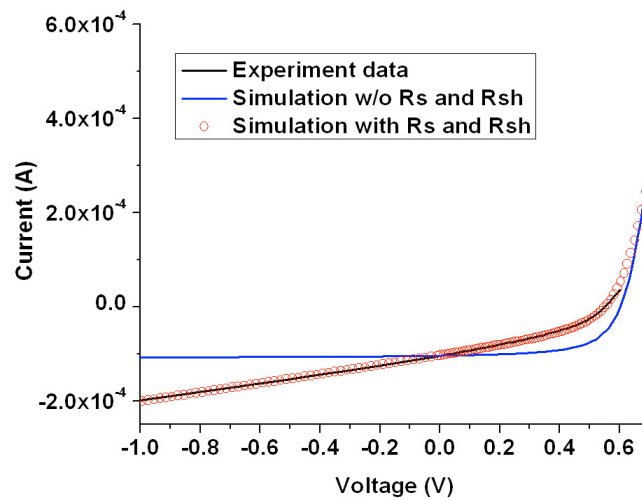


Figure 7-21. Comparison between measured (black curve) and simulated current-voltage curves with (red dots) and without (blue curve) R_s and R_{sh} for P3HTT-BTD:PC₆₁BM solar cells.

7.5.3 Short circuit condition, open circuit condition, and maximum power condition

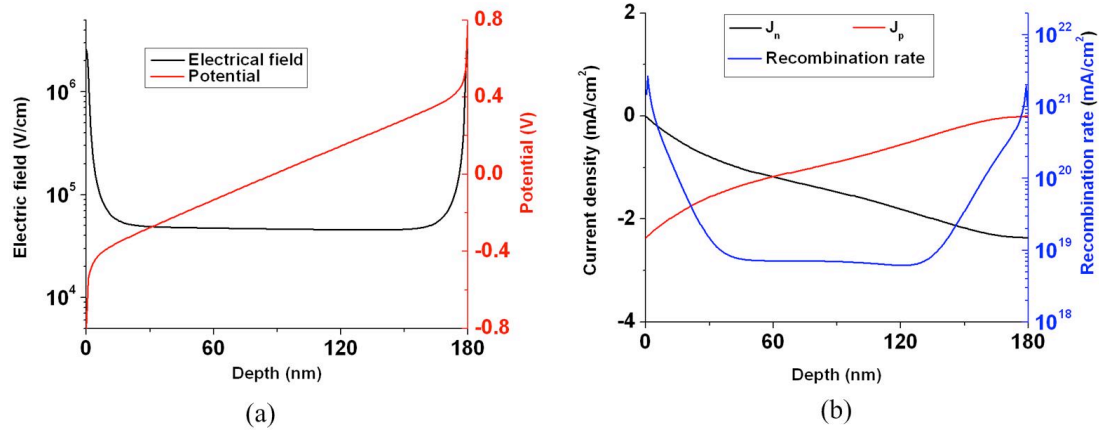


Figure 7-22. Electric potential, electric field, recombination rate, and current densities at short circuit condition.

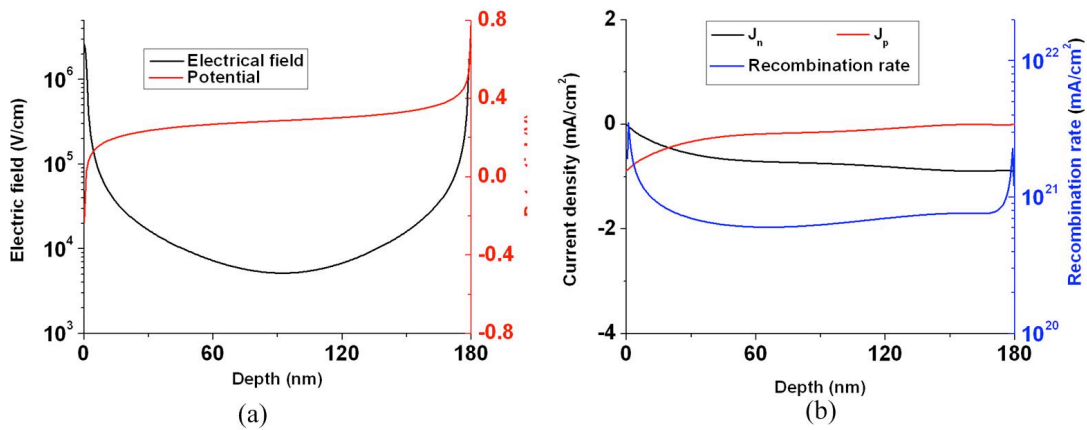


Figure 7-23. electric potential, electric field, recombination rate and current densities at open circuit condition.

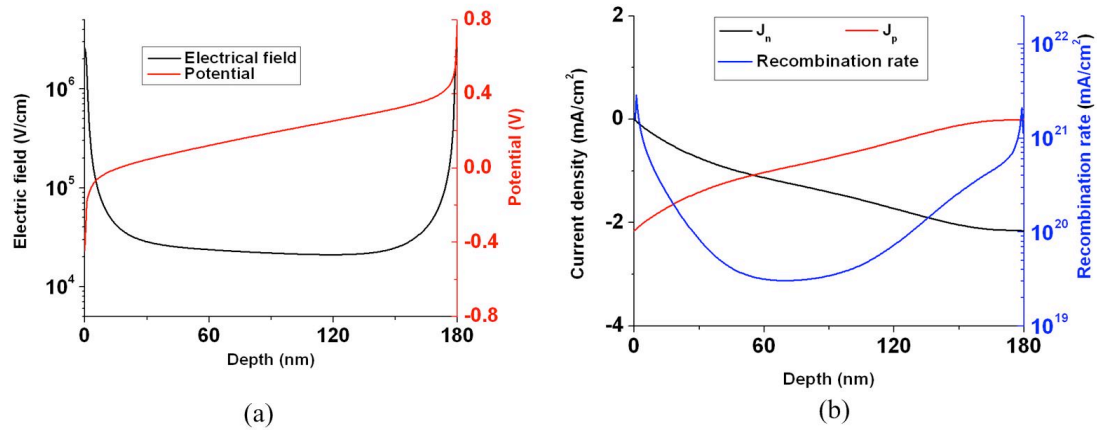


Figure 7-24. Electric potential, electric field, recombination rate and current densities at maximum power condition.

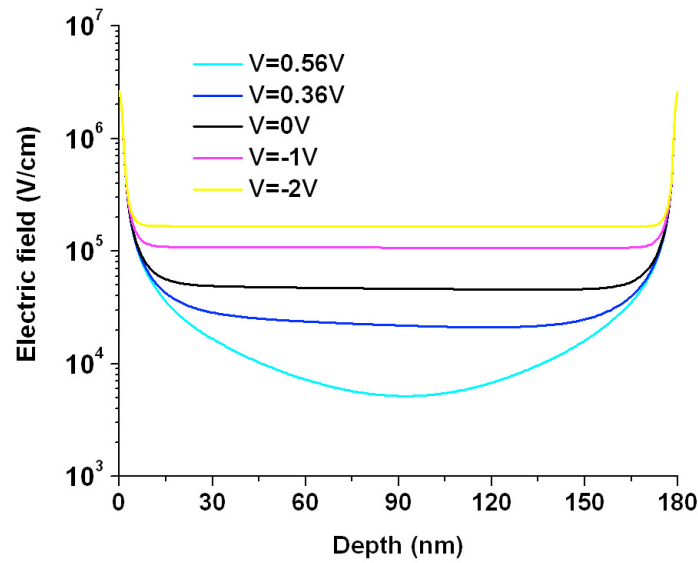


Figure 7-25. Electric field at different applied bias for P3HTT-BTD:PC₆₁BM solar cells.

The calculated electric potential, electric field, recombination rate and current densities at short circuit condition, open circuit condition and maximum power condition are depicted in Fig.7-22 to Fig. 7-24, respectively. The open circuit voltage is 0.566 and the maximum power condition is at 0.36V. The electric field vs. applied voltage is shown

in Fig. 7-19. Compared with P3HT:PC₆₁BM solar cells, the electric field, electric potential, recombination rate, and current densities for P3HTT-BTD:PC₆₁BM solar cells show the similar trends. The magnitude of the recombination rate is similar to that of the P3HTT-TP:PC₆₁BM solar cells, which is an order of magnitude lower than that of P3HT:PC₆₁BM solar cells. This arises from a lower polaron pair generation rate and higher intrinsic density.

7.6 Discussion and summary

In summary, an organic BHJ solar cell numerical model is developed in this chapter. Different from the basic Koster model, non-uniform photon absorption, exciton diffusion, non-geminate recombination, and R_s and R_{sh} effects are considered. These considerations are constructed based on experimental measurements for four types of polymer: PC₆₁BM. Current-voltage curves are simulated under AM1.5 condition. Electric field, electric potential, positive polaron and negative polaron current densities, and recombination rates are analyzed under dark, short circuit and open circuit condition.

The results show that the trap-assisted recombination mechanisms will not only affect the shape of the I-V characteristics, but will also influence the series resistance and shunt resistance. This is particularly obvious in P3HT-TP:PC₆₁BM solar cells.

Chapter 8. Overview, summary, and future work

8.1 Overview of efficiencies

Table 8-1. Efficiency summary for four polymer:PC₆₁BMS cells at 640nm.

	η_a	η_{ed}	η_{cd}	η_{cc}	$\eta_{eqe} (\%)$	$\eta_{eqe} (\%)$
	(%)	(%)	(%)	(%)	calculated	measured
P3HT:PC ₆₁ BM	10.8	100.0	91.0	82	8.1	9.1
P3HTT-DPP- 10%:PC ₆₁ BM	51.0	100.0	85.0	76.2	33.0	33.9
P3HTT-TP:PC ₆₁ BM	35.9	33.8	53.0	79.4	5.1	8.0
P3HTT-BTD:PC ₆₁ BM	43.6	69.6	27.0	69.4	5.7	6.5

The efficiencies of solar cells are generally expressed in three ways: power conversion efficiency (PCE), external quantum efficiency (EQE) and internal quantum efficiency (IQE). The short circuit current density, as an important parameter, strongly influences the PCE and is linked to the EQE and IQE. In the preceding chapters, we focused on the four sequential charge transport efficiencies. We now shift the analysis to how these efficiencies relate to the EQE and IQE, and, thus, the short circuit current density.

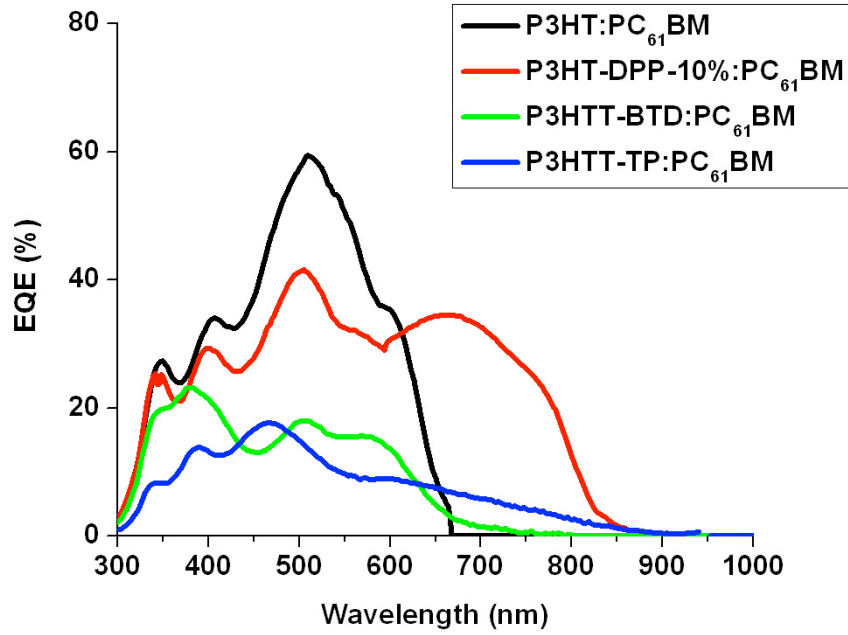
External quantum efficiency is defined as the ratio of the number of electrons collected by electrodes to the number of incident photons at a specific wavelength. Typically, the EQE in solar cells can be expressed as a product of the efficiencies of the primary physical mechanisms, absorption efficiency, η_a , exciton diffusion efficiency, η_{ed} , bound polaron dissociation efficiency, η_{cd} , and free polaron collection efficiency, η_{cc} :

$$\eta_e = \eta_a \eta_{ed} \eta_{cd} \eta_{cc} . \quad (6-4)$$

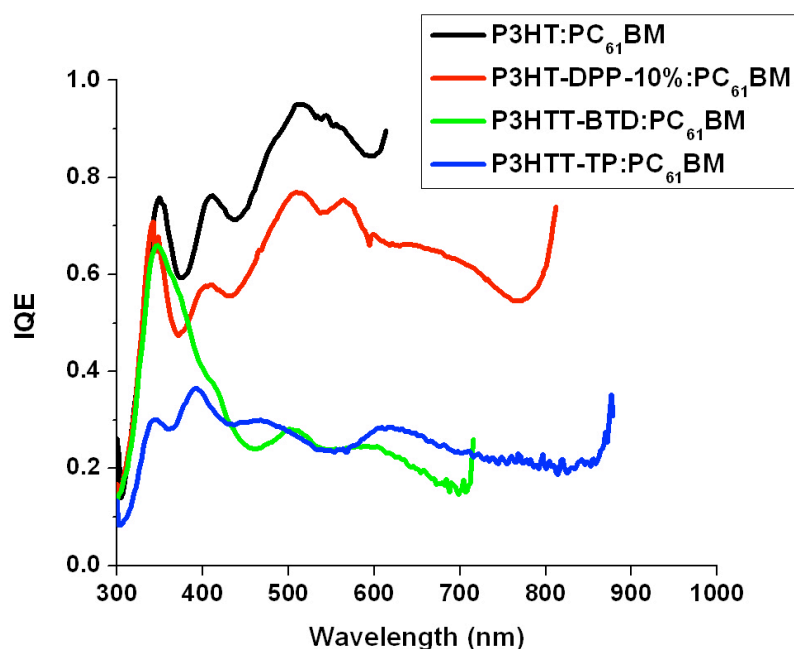
The EQE usually reflects the losses by absorption and charge transportation. Internal quantum efficiency, on the other hand, is defined as the ratio of the number of carriers collected at the electrode to the number of photons absorbed in the device. The IQE is usually described as

$$\eta_{iqe} = \frac{\eta_e}{\eta_a} = \eta_{ed} \eta_{cd} \eta_{cc} . \quad (8-1)$$

Compared with EQE, IQE excludes the influence of absorption.



(a)



(b)

Figure 8-1. (a) EQE and (b) IQE for four types of polymer:PC₆₁BM solar cells.

Table 8-1 summarizes all the efficiencies at 640 nm. The complete spectral EQE and IQE are plotted in Fig 8-1. There is a good correlation between the calculated EQE using Equation 6-4 and the measured EQE at 640 nm for P3HT:PC₆₁BM, P3HTT-DPP-10%:PC₆₁BM and P3HTT-BTD:PC₆₁BM solar cells. For P3HTT-TP:PC₆₁BM solar cells, the variance between measured EQE and calculated EQE is much bigger than for the other solar cells. We note, that the efficiencies of each step in the photocurrent generation of P3HT:PC₆₁BM obtained with the techniques described in this dissertation match closely with the data obtained using TAS by Guo et al. [120]. These results demonstrate the feasibility of applying these techniques to characterize the efficiencies of the key processes to different polymer:fullerene systems. The results provide insight to identify the most limiting step in the photoconversion process. The results presented above apply

only to 640 nm excitation and may be different at other wavelengths. There are several reasons for that. The first one is the light source for transient photocurrent measurement is 640 nm, which means the collection efficiency is only accurate at this wavelength. If we use a different wavelength pulse source, the spatial distribution of the absorption will change, which will also affect the free polaron transport pathway. The second reason is related to the light source for the exciton diffusion J - V measurements. A 632 nm light source was used as the measurement wavelength and tuned to the intensity to match the 1-sun condition. Since it is not at 640 nm, we encounter a similar issue. There are also other factors, such as surface scattering, the accuracy of the active layer thickness measurement, and the uniformity of the films that may affect the results [121].

The IQE of an organic BHJ solar cell is rarely reported in the literature. This is primarily due to inaccurate measurement of active layer absorption. As shown in Fig. 8-1(b), the IQE exhibits larger variations for above bandgap illumination than inorganic solar cells and is consistent with previous reports that IQE is not a constant value for all the wavelengths [121]. This is maybe due to surface scattering, the accuracy of the active layer thickness measurement, and the uniformity of the films. Further study is needed.

8.2 Summary

Harvesting energy from the sun is an attractive and easy way to benefit human society. Owing to their compatibility with flexible substrates, low-cost, and potential for large-area manufacture, organic solar cells have been widely studied in recent years. The increase in power conversion efficiency of single junction BHJ solar cells from 3% to 10.7% in the past 10 years can be attributed to multidisciplinary research and industrial

development. However, there is still a room for further improvement to reach the thermodynamic PCE limit of ~22%.

The goal of this work has been to study the photocurrent limitation mechanisms in organic bulk heterojunction solar cells. The photocurrent in a BHJ solar cell is related to four sequential charge transfer processes: photon absorption and exciton generation, exciton diffusion, polaron pair dissociation, and free polaron collection. By applying and developing complementary simulation tools and experiment techniques, the efficiency of each step was determined for P3HT:PC₆₁BM, P3HTT-DPP-10%:PC₆₁BM, P3HTT-TP:PC₆₁BM and P3HTT-BTD:PC₆₁BM BHJ solar cells.

In order to overcome the inaccuracy of absorption determination due to optical interference, the optical transfer-matrix-theory has been applied to organic BHJ solar cells. The complex refractive index was extracted first. Then, the optical electrical field and absorption profile were calculated for four different polymer: PC₆₁BM BHJ solar cells. Compared to P3HT:PC₆₁BM, the other three semi-random polymer:PC₆₁BM thin films exhibit significantly broader absorption spectra and thus an increase in AM1.5 absorption.

The exciton diffusion efficiency was analyzed by using J-V measurements at large reverse bias. The efficiencies for four polymers with PC₆₁BM are presented and compared. P3HTT-TP: PC₆₁BM and P3HTT-BTD solar cells show much smaller diffusion efficiency, which is possibly due to the shorter exciton decay time. Under large reverse bias, the currents for all the cells show a large drop after the electric field reaches $E=6 \times 10^7$ V/m. This is contrary to the field-independent current predicted by the Onsager-

Braun model. The current drop is analyzed in terms of the breakdown mechanisms, and the tunneling effect is found to be the dominate breakdown mechanism in most devices.

The polaron pair dissociation efficiency is analyzed using the well known Onsager-Braun model. At short circuit condition, η_{cd} is 91%, 85%, 53% and 27% for P3HT:PC₆₁BM, P3HTT-DPP-10%:PC₆₁BM, P3HTT-TP:PC₆₁BM and P3HTT-BTD:PC₆₁BM solar cells, respectively. The variation between materials arises from the difference in polaron pair decay rates. However, the underlying physical determination of the mechanisms for the different decay rates needs further study. The capacitance characteristics were also tested and analyzed. For four different polymer:PC₆₁BM solar cells, C-V curves exhibited similar behavior, which verified the available C-V theory for BHJ solar cells.

For characterizing the free polaron collection efficiency, the sweep out time and the recombination lifetime were studied. Three techniques were developed to analyze the recombination mechanisms. These techniques are transient photoconductivity, forward-to-zero transient-current response, and electric field dependent photoresponse techniques. Measurements on P3HT:PCB₆₁M solar cells show that these three measurement techniques yield consistent results. The recombination lifetime for a P3HT:PCB₆₁M solar cell is estimated to be $\sim 1\text{-}4\mu\text{s}$. The recombination lifetime for three other types of solar cells were also measured by transient photoductivity technique. For P3HTT-TP:PC₆₁BM and P3HTT-BTD:PC₆₁BM solar cells, the shorter recombination lifetimes reflect the possibility of deep trapping inside the BHJ solar cells. This was confirmed by light intensity dependent V_{oc} measurements. The non-unity ideality factor is consistent with deep trap-assisted SRH recombination in P3HTT-TP:PC₆₁BM solar cells, and trap-

assisted Auger recombination in P3HTT-BTD:PC₆₁BM solar cells. The free polaron collection efficiencies of these solar cell materials have been calculated and compared. Meanwhile, the thermal annealing effect on charge transport, recombination lifetime and mobility for P3HT:PC₆₁BM solar cells was measured for different thermal annealing temperatures. 140°C was shown to be the optimum annealing temperature, since that temperature yields the highest mobility-lifetime product and better morphology.

External quantum efficiency and internal quantum efficiency were also studied for four types of polymer: PC₆₁BM solar cells. At 640nm, the EQE is consistent with the product of the four efficiencies discussed above. These results demonstrate the feasibility of applying the techniques described above to characterize the efficiencies of the key processes to different polymer:fullerene systems and to identify the most limiting step in the photoconversion process.

In addition to the experiments, a new organic BHJ solar cell numerical model has been developed. Based on the Koster model [30], non-uniform photon absorption, exciton diffusion, non-geminate recombination, and the effect of series resistance, R_s , and shunt resistance, R_{sh} , are considered and added to the drift-diffusion model. These considerations are constructed based on measurements on four types of polymer: PC₆₁BM. The I-V curves have been simulated under AM1.5 condition. Electric field, electric potential, positive polaron and negative polaron current densities, and recombination rates were also analyzed under dark, short circuit and open circuit condition. The results show that the trap-assisted recombination mechanisms will not only affect the shape of I-V characteristic, but also influence the series resistance and shunt resistance.

8.3 Future work

The promising power conversion efficiency improvement of organic bulk heterojunction solar cells provides opportunities for future experimental and theoretical studies. In this section, some ideas for future work are presented.

8.3.1 Enhancement of absorption by fluorescence structure design

Compared to the inorganic solar cells, broadband and high absorption is still a big challenge in order to improve the efficiency of organic BHJ photovoltaic cells. The improvement of the absorption can be achieved by different methods, such as tandem structures [14, 122-124], downconversion[125-131], upconversion[132-138], synthesis of broad band absorption polymers[31, 32, 139-142], scattering, employing plasmonic effects[143-148], and using fluorescence concentrators[149-154]. Considering our lab's capability, the fluorescence converter appears to be a viable approach.

As shown in Fig. 8-2, two different structures with back fluorescence converters are proposed. Fig. 8-2(a) shows a typical BHJ solar cell with a back fluorescence converter. The key to this design is to find the right transparent cathode to match the work function of Al and the right fluorescent material that exhibits high conversion yield. Fig. 8-2 (b) shows another realization of a BHJ device with a fluorescence converter. The device itself is an inverted solar cell, which means ITO is the cathode and PEDOT:Au is the anode. This structure is typically used in the organic tandem solar cells to solve the transparent cathode problem[148]. The use of gold in PEDOT could also induce the plasmonic effect in the cells, which may enhance light absorption.

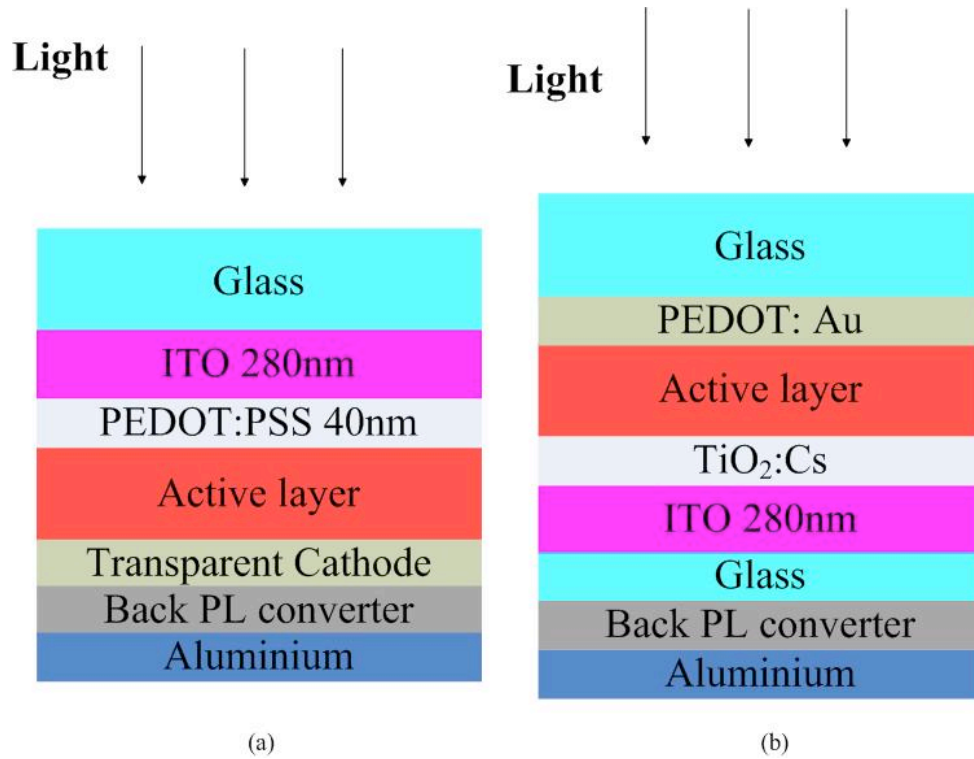


Figure 8-2. BHJ solar cells with back fluorescence converter (a) a typical BHJ device with a back fluorescence converter (b) a converted BHJ device with a back fluorescence converter.

8.3.2 Relationship between energetic disorder and fill factor by numerical simulation

In recent years, it has become clear that the energetic structure of conjugated materials is complex, and the reduction of a model to simple, well-defined, energy levels is an oversimplification [155]. Experimentally, the low fill factor has been shown to be related to the significant energetic disorder. This disorder leads to charge trapping in solar cells, which in turn causes higher carrier concentrations and more nongeminate recombination [156, 157]. Therefore, a systematic study of the relationship between energetic disorder and fill factor is important and meaningful. By introducing the energetic disorder to the density of states distribution, the fill factor can be simulated in

the numerical drift-diffusion model, and the results could provide a design guidance for new polymer synthesis.

8.3.3 Morphology effect on P3HTT-DPP-10%: PCB₆₁M P3HTT-TP: PCB₆₁M and P3HTT-BTD: PCB₆₁M solar cells performance

The morphology of the active layer of organic solar cells is crucial to device performance, since it reflects the domain scale, phase separation, and crystallization of the material. The morphology of P3HT: PCB₆₁M has been well studied [158-161], while the morphology effect on P3HTT-DPP-10%: PCB₆₁M P3HTT-TP: PCB₆₁M and P3HTT-BTD: PCB₆₁M solar cells is not yet fully understood. The morphology analyses could be conducted experimentally and theoretically.

The morphology of the devices is usually characterized by AFM, TEM and GIXD. Several conditions could be applied on the solar cells to better understand the morphology, i.e. the effect of thermal annealing, weight ratio of polymer and PCB₆₁M, and the thickness of the active layer. Meanwhile, Mesoscopic Monte Carlo simulation could also be used to analyze the effect of morphology on the performance of organic photovoltaics [162, 163].

REFERENCE

- [1] Solar Cell. Retrieved June. 17, from http://en.wikipedia.org/wiki/Solar_cells, "<Solar energy - Wikipedia, the free encyclopedia.pdf>."
- [2] R. N. International Statistics: world primary energy consumption by region and type, 2011, from <http://www.census.gov/compendia/statab/2012/tables/12s1380.pdf>, "<world primary production.pdf>."
- [3] M. A. Green, *et al.*, "Solar cell efficiency tables (version 40)," *Progress in Photovoltaics: Research and Applications*, vol. 20, pp. 606-614, 2012.
- [4] H. Hoppe and N. S. Sariciftci, "Organic solar cells: An overview," *Journal of Materials Research*, vol. 19, pp. 1924-1945, 2004.
- [5] T. Kietzke, "Recent Advances in Organic Solar Cells," *Advances in OptoElectronics*, vol. 2007, pp. 1-16, 2007.
- [6] B. C. K. Thompson, P. P.; Burkhart, B.; Aviles, A. E.; Rudenko, A.; Shultz, G. V.; Ng, C. F.; Mangubat, L. B. , "Polymer-Based Solar Cells: State-of-the-Art Principles for the Design of Active Layer Components," *Green*, vol. 1, pp. 29-54, 2011.
- [7] C. W. Schlenker and M. E. Thompson, "The molecular nature of photovoltage losses in organic solar cells," *Chemical Communications*, vol. 47, p. 3702, 2011.
- [8] T. M. Clarke and J. R. Durrant, "Charge photogeneration in organic solar cells," *Chem. Rev.*, vol. 110, pp. 6736-6767, 2010.
- [9] C. L. Chochos and S. A. Choulis, "How the structural deviations on the backbone of conjugated polymers influence their optoelectronic properties and photovoltaic performance," *Progress in Polymer Science*, vol. 36, pp. 1326-1414, 2011.
- [10] H. Zhou, *et al.*, "Rational Design of High Performance Conjugated Polymers for Organic Solar Cells," *Macromolecules*, vol. 45, pp. 607-632, 2012.
- [11] N. Giebink, *et al.*, "Thermodynamic efficiency limit of excitonic solar cells," *Physical Review B*, vol. 83, 2011.
- [12] J. D. Kotlarski and P. W. M. Blom, "Ultimate performance of polymer:fullerene bulk heterojunction tandem solar cells," *Applied Physics Letters*, vol. 98, p. 053301, 2011.
- [13] G. Dennler, *et al.*, "Polymer-Fullerene Bulk-Heterojunction Solar Cells," *Advanced Materials*, vol. 21, pp. 1323-1338, 2009.
- [14] T. Ameri, *et al.*, "Organic tandem solar cells: A review," *Energy & Environmental Science*, vol. 2, p. 347, 2009.
- [15] P. W. M. Blom, *et al.*, "Device Physics of Polymer:Fullerene Bulk Heterojunction Solar Cells," *Advanced Materials*, vol. 19, pp. 1551-1566, 2007.
- [16] C. Deibel and V. Dyakonov, "Polymer–fullerene bulk heterojunction solar cells," *Reports on Progress in Physics*, vol. 73, p. 096401, 2010.
- [17] M. C. Scharber, *et al.*, "Design Rules for Donors in Bulk-Heterojunction Solar Cells—Towards 10 % Energy-Conversion Efficiency," *Advanced Materials*, vol. 18, pp. 789-794, 2006.

- [18] M. D. Perez, *et al.*, "Molecular and morphological influences on the open circuit voltages of organic photovoltaic devices," *J. Am. Chem. Soc.*, vol. 131, pp. 9281-9286, 2009.
- [19] D. Veldman, *et al.*, "The Energy of Charge-Transfer States in Electron Donor-Acceptor Blends: Insight into the Energy Losses in Organic Solar Cells," *Advanced Functional Materials*, vol. 19, pp. 1939-1948, 2009.
- [20] L. J. A. Koster, *et al.*, "Light intensity dependence of open-circuit voltage of polymer:fullerene solar cells," *Applied Physics Letters*, vol. 86, p. 123509, 2005.
- [21] N. Giebink, *et al.*, "Ideal diode equation for organic heterojunctions. I. Derivation and application," *Physical Review B*, vol. 82, p. 155305, 2010.
- [22] S. van Bavel, *et al.*, "On the Importance of Morphology Control in Polymer Solar Cells," *Macromolecular Rapid Communications*, vol. 31, pp. 1835-1845, 2010.
- [23] C. J. Brabec, Heeney, M., McCulloch, I., Nelson, J., "Influence of blend microstructure on bulk heterojunction organic photovoltaic performance," *Chem. Soc. Rev.*, vol. 40, p. 1185, 2011.
- [24] J. D. Kotlarski, *et al.*, "Role of balanced charge carrier transport in low band gap polymer:Fullerene bulk heterojunction solar cells," *Journal of Polymer Science Part B: Polymer Physics*, vol. 49, pp. 708-711, 2011.
- [25] A. Guerrero, *et al.*, "Series resistance in organic bulk-heterojunction solar devices: Modulating carrier transport with fullerene electron traps," *Organic Electronics*, vol. 13, pp. 2326-2332, 2012.
- [26] S. M. Sze and K. K. Ng, *Physics of semiconductor devices*. New York: Wiley, 2005.
- [27] J. Xue, *et al.*, "4.2% efficient organic photovoltaic cells with low series resistances," *Applied Physics Letters*, vol. 84, p. 3013, 2004.
- [28] G. Li, *et al.*, "Investigation of annealing effects and film thickness dependence of polymer solar cells based on poly(3-hexylthiophene)," *Journal of Applied Physics*, vol. 98, p. 043704, 2005.
- [29] Y. Shen, *et al.*, "Bulk and contact resistance in P3HT:PCBM heterojunction solar cells," *Solar Energy Materials and Solar Cells*, vol. 95, pp. 2314-2317, 2011.
- [30] L. Koster, *et al.*, "Device model for the operation of polymer/fullerene bulk heterojunction solar cells," *Physical Review B*, vol. 72, p. 085205, 2005.
- [31] B. Burkhart, *et al.*, "'Semi-Random' Multichromophoric rr-P3HT Analogues for Solar Photon Harvesting," *Macromolecules*, vol. 44, pp. 1214-1246, 2011.
- [32] P. P. Khlyabich, *et al.*, "Efficient Solar Cells from Semi-random P3HT Analogues Incorporating Diketopyrrolopyrrole," *Macromolecules*, vol. 44, pp. 5079-5084, 2011.
- [33] K. Kawano, *et al.*, "Degradation of organic solar cells due to air exposure," *Solar Energy Materials and Solar Cells*, vol. 90, pp. 3520-3530, 2006.
- [34] M. Manceau, *et al.*, "Light-induced degradation of the P3HT-based solar cells active layer," *Solar Energy Materials and Solar Cells*, vol. 95, pp. 1315-1325, 2011.
- [35] S. Bertho, *et al.*, "Effect of temperature on the morphological and photovoltaic stability of bulk heterojunction polymer:fullerene solar cells," *Solar Energy Materials and Solar Cells*, vol. 92, pp. 753-760, 2008.

- [36] M. Jørgensen, *et al.*, "Stability/degradation of polymer solar cells," *Solar Energy Materials and Solar Cells*, vol. 92, pp. 686-714, 2008.
- [37] (2012, Aug. 4th). <http://www.delo.de/en/products/adhesives/delo-katiobond/>.
- [38] A. J. Moulé and K. Meerholz, "Interference method for the determination of the complex refractive index of thin polymer layers," *Applied Physics Letters*, vol. 91, p. 061901, 2007.
- [39] O. S. Heavens, *Optical properties of thin solid films*. New York: Dover, 1965.
- [40] R. Marcus, "Electron transfer reactions in chemistry. Theory and experiment," *Reviews of Modern Physics*, vol. 65, pp. 599-610, 1993.
- [41] R. A. Marcus, "On the Theory of Oxidation-Reduction Reactions Involving Electron Transfer. I," *The Journal of Chemical Physics*, vol. 24, p. 966, 1956.
- [42] A. Miller and E. Abrahams, "Impurity Conduction at Low Concentrations," *Physical Review*, vol. 120, pp. 745-755, 1960.
- [43] H. Bässler, "Charge transport in disordered organic photoconductors-A Monte Carlo simulation study," *Phys. Status Solidi b*, vol. 175, pp. 15-56, 1993.
- [44] H. Houili, *et al.*, "Investigation of the charge transport through disordered organic molecular heterojunctions," *Journal of Applied Physics*, vol. 100, p. 033702, 2006.
- [45] V. D. Mihailetschi, *et al.*, "Charge Transport and Photocurrent Generation in Poly(3-hexylthiophene): Methanofullerene Bulk-Heterojunction Solar Cells," *Advanced Functional Materials*, vol. 16, pp. 699-708, 2006.
- [46] C. Tanase, *et al.*, "Origin of the enhanced space-charge-limited current in poly(p-phenylene vinylene)," *Physical Review B*, vol. 70, p. 193202, 2004.
- [47] L. M. Popescu, *et al.*, "Thienyl analog of 1-(3-methoxycarbonyl)propyl-1-phenyl-[6,6]-methanofullerene for bulk heterojunction photovoltaic devices in combination with polythiophenes," *Applied Physics Letters*, vol. 89, p. 213507, 2006.
- [48] S. Cho, *et al.*, "Ambipolar organic field-effect transistors fabricated using a composite of semiconducting polymer and soluble fullerene," *Applied Physics Letters*, vol. 89, p. 153505, 2006.
- [49] E. Vonhauß, *et al.*, "Study of field effect mobility in PCBM films and P3HT:PCBM blends," *Solar Energy Materials and Solar Cells*, vol. 87, pp. 149-156, 2005.
- [50] V. Coropceanu, *et al.*, "Charge Transport in Organic Semiconductors," *Chemical Reviews*, vol. 107, pp. 926-952, 2007.
- [51] P. W. M. Blom, *et al.*, "Electric-field and temperature dependence of the hole mobility in poly(p-phenylene vinylene)," *physical review B*, vol. 55, pp. R656-R659.
- [52] C. J. Brabec, *et al.*, "Effect of LiF/metal electrodes on the performance of plastic solar cells," *Applied Physics Letters*, vol. 80, p. 1288, 2002.
- [53] E. Bundgaard and F. Krebs, "Low band gap polymers for organic photovoltaics," *Solar Energy Materials and Solar Cells*, vol. 91, pp. 954-985, 2007.
- [54] R. Kroon, *et al.*, "Small Bandgap Polymers for Organic Solar Cells(Polymer Material Development in the Last 5 Years)," *Polymer Reviews*, vol. 48, pp. 531-582, 2008.

- [55] D. W. Sievers, *et al.*, "Modeling optical effects and thickness dependent current in polymer bulk-heterojunction solar cells," *Journal of Applied Physics*, vol. 100, p. 115409, 2006.
- [56] L. A. A. Pettersson, *et al.*, "Modeling photocurrent action spectra of photovoltaic devices based on organic thin films," *Journal of Applied Physics*, vol. 86, p. 487, 1999.
- [57] J. D. Kotlarski, *et al.*, "Combined optical and electrical modeling of polymer:fullerene bulk heterojunction solar cells," *Journal of Applied Physics*, vol. 103, p. 084502, 2008.
- [58] O. Stenzel, *The physics of thin film optical spectra: an introduction*. New York: Springer Berlin Heidelberg, 2005.
- [59] P. M. Beaujuge, *et al.*, "Spectral engineering in π -conjugated polymers with intramolecular donor-acceptor interactions," *Acc. Chem. Res.*, vol. 43, p. 1396, 2010.
- [60] M. C. Gurau, *et al.*, "Measuring molecular order in poly(3-alkylthiophene) thin films with polarizing spectroscopies," *Langmuir*, pp. 834-842, 2007.
- [61] P. E. Shaw, *et al.*, "Exciton Diffusion Measurements in Poly(3-hexylthiophene)," *Advanced Materials*, vol. 20, pp. 3516-3520, 2008.
- [62] K. J. Bergemann and S. R. Forrest, "Measurement of exciton diffusion lengths in optically thin organic films," *Applied Physics Letters*, vol. 99, p. 243303, 2011.
- [63] A. Haugeneder, *et al.*, "Exciton diffusion and dissociation in conjugated polymer/fullerene blends and heterostructures," *Physical Review B*, vol. 69, p. 15346, 1999.
- [64] D. E. Markov, *et al.*, "Accurate Measurement of the Exciton Diffusion Length in a Conjugated Polymer Using a Heterostructure with a Side-Chain Cross-Linked Fullerene Layer," *Journal of Physical Chemistry A*, vol. 109, pp. 5266-5274, 2005.
- [65] P. Peumans, *et al.*, "Small molecular weight organic thin-film photodetectors and solar cells," *Journal of Applied Physics*, vol. 93, p. 3693, 2003.
- [66] S. Cook, *et al.*, "Estimate of singlet diffusion lengths in PCBM films by time-resolved emission studies," *Chemical Physics Letters*, vol. 478, pp. 33-36, 2009.
- [67] S. Lilliu, *et al.*, "Dynamics of Crystallization and Disorder during Annealing of P3HT/PCBM Bulk Heterojunctions," *Macromolecules*, vol. 44, pp. 2725-2734, 2011.
- [68] S. Lilliu, *et al.*, "Effects of Thermal Annealing Upon the Nanomorphology of Poly(3-hexylselenophene)-PCBM Blends," *Macromolecular Rapid Communications*, vol. 32, pp. 1454-1460, 2011.
- [69] R. C. Nieuwendaal, *et al.*, "Measuring Domain Sizes and Compositional Heterogeneities in P3HT-PCBM Bulk Heterojunction Thin Films with ¹H Spin Diffusion NMR Spectroscopy," *Advanced Functional Materials*, vol. 22, pp. 1255-1266, 2012.
- [70] C. L. Braun, "Electric field assisted dissociation of charge transfer states as a mechanism of photocarrier production," *The Journal of Chemical Physics*, vol. 80, p. 4157, 1984.

- [71] S. Cowan, *et al.*, "Transient photoconductivity in polymer bulk heterojunction solar cells: Competition between sweep-out and recombination," *Physical Review B*, vol. 83, p. 035205, 2011.
- [72] M. A. Loi, *et al.*, "Charge Transfer Excitons in Bulk Heterojunctions of a Polyfluorene Copolymer and a Fullerene Derivative," *Advanced Functional Materials*, vol. 17, pp. 2111-2116, 2007.
- [73] A. Morteani, *et al.*, "Exciton Regeneration at Polymeric Semiconductor Heterojunctions," *Physical Review Letters*, vol. 92, p. 247402, 2004.
- [74] Y. Zhou, *et al.*, "Observation of a Charge Transfer State in Low-Bandgap Polymer/Fullerene Blend Systems by Photoluminescence and Electroluminescence Studies," *Advanced Functional Materials*, vol. 19, pp. 3293-3299, 2009.
- [75] M. Scharber, *et al.*, "Optical- and photocurrent-detected magnetic resonance studies on conjugated polymer/fullerene composites," *Physical Review B*, vol. 67, p. 085202, 2003.
- [76] C. Deibel, *et al.*, "Role of the Charge Transfer State in Organic Donor-Acceptor Solar Cells," *Advanced Materials*, vol. 22, pp. 4097-4111, 2010.
- [77] V. Mihailetschi, *et al.*, "Photocurrent Generation in Polymer-Fullerene Bulk Heterojunctions," *Physical Review Letters*, vol. 93, p. 226601, 2004.
- [78] M. Limpinsel, *et al.*, "Photocurrent in bulk heterojunction solar cells," *Physical Review B*, vol. 81, p. 085203, 2010.
- [79] P. Langevin, *Ann. Chim. Phys*, vol. 28, p. 433, 1903.
- [80] C. Deibel, *et al.*, "Energetics of excited states in the conjugated polymer poly(3-hexylthiophene)," *Physical Review B*, vol. 81, p. 085202, 2010.
- [81] A. Kokil, *et al.*, "Techniques for characterization of charge carrier mobility in organic semiconductors," *Journal of Polymer Science Part B: Polymer Physics*, vol. 50, pp. 1130-1144, 2012.
- [82] M. Mingebach, *et al.*, "Built-in potential and validity of the Mott-Schottky analysis in organic bulk heterojunction solar cells," *Physical Review B*, vol. 84, 2011.
- [83] J. Bisquert, *et al.*, "Band unpinning and photovoltaic model for P3HT:PCBM organic bulk heterojunctions under illumination," *Chemical Physics Letters*, vol. 465, pp. 57-62, 2008.
- [84] E. H. Rhoderick and R. H. Williams, Eds., *Metal-Semiconductor Contacts*. Oxford: Clarendon Press, 1988, p. ^pp. Pages.
- [85] L. J. A. Koster, *et al.*, "Bimolecular recombination in polymer/fullerene bulk heterojunction solar cells," *Applied Physics Letters*, vol. 88, p. 052104, 2006.
- [86] D. J. D. Moet, *et al.*, "Impact of molecular weight on charge carrier dissociation in solar cells from a polyfluorene derivative," *Organic Electronics*, vol. 10, pp. 1275-1281, 2009.
- [87] K. Li, *et al.*, "Recombination lifetime of free polarons in polymer/fullerene bulk heterojunction solar cells," *Journal of Applied Physics*, vol. 111, p. 034503, 2012.
- [88] S. M. Tuladhar, *et al.*, "Ambipolar charge transport in films of methanofullerene and poly(phenylenevinylene)/methanofullerene blends," *advanced Functional Materials*, vol. 15, p. 1171, 2005.

- [89] S. A. Choulis, *et al.*, "High ambipolar and balanced carrier mobility in regioregular poly(3-hexylthiophene)," *Applied Physics Letters*, vol. 85, p. 3890, 2004.
- [90] A. J. Mozer and N. S. Sariciftci, "Negative electric field dependence of charge carrier drift mobility in conjugated, semiconducting polymers," *Chemical Physics Letters*, vol. 389, pp. 438-442, 2004.
- [91] R. Street, *et al.*, "Experimental test for geminate recombination applied to organic solar cells," *Physical Review B*, vol. 82, 2010.
- [92] R. A. Street and M. Schoendorf, "Interface state recombination in organic solar cells," *Physical Review B*, vol. 81, p. 205307, 2010.
- [93] R. D. Pensack, *et al.*, "Charge trapping in organic photovoltaic materials examined with time-resolved vibrational spectroscopy," *The Journal of Physical Chemistry C*, vol. 114, pp. 5344-5350, 2010.
- [94] I. Montanari, *et al.*, "Transient optical studies of charge recombination dynamics in a polymer/fullerene composite at room temperature," *Applied Physics Letters*, vol. 81, p. 3001, 2002.
- [95] G. Garcia-Belmonte, *et al.*, "Charge carrier mobility and lifetime of organic bulk heterojunctions analyzed by impedance spectroscopy," *Organic Electronics*, vol. 9, pp. 847-851, 2008.
- [96] G. Garcia-Belmonte, *et al.*, "Simultaneous determination of carrier lifetime and electron density-of-states in P3HT:PCBM organic solar cells under illumination by impedance spectroscopy," *Solar Energy Materials and Solar Cells*, vol. 94, pp. 366-375, 2010.
- [97] K. Li, *et al.*, "Determination of free polaron lifetime in organic bulk heterojunction solar cells by transient time analysis," *Journal of Applied Physics*, vol. 108, p. 084511, 2010.
- [98] W. Ma, *et al.*, "Thermally stable, efficient polymer solar cells with nanoscale control of the interpenetrating network morphology," *Advanced Functional Materials*, vol. 15, pp. 1617-1622, 2005.
- [99] A. Pivrikas, *et al.*, "Bimolecular Recombination Coefficient as a Sensitive Testing Parameter for Low-Mobility Solar-Cell Materials," *Physical Review Letters*, vol. 94, p. 176806, 2005.
- [100] M. Punke, *et al.*, "Dynamic characterization of organic bulk heterojunction photodetectors," *Applied Physics Letters*, vol. 91, p. 071118, 2007.
- [101] C. G. Shuttle, *et al.*, "Experimental determination of the rate law for charge carrier decay in a polythiophene: Fullerene solar cell," *Applied Physics Letters*, vol. 92, p. 093311, 2008.
- [102] N. S. Christ, *et al.*, "Nanosecond response of organic solar cells and photodetectors," *Journal of Applied Physics*, vol. 105, p. 104513, 2009.
- [103] Z. Li and C. R. McNeill, "Transient photocurrent measurements of PCDTBT:PC70BM and PCPDTBT:PC70BM Solar Cells: Evidence for charge trapping in efficient polymer/fullerene blends," *Journal of Applied Physics*, vol. 109, p. 074513, 2011.
- [104] S. R. Cowan, *et al.*, "Identifying a Threshold Impurity Level for Organic Solar Cells: Enhanced First-Order Recombination Via Well-Defined PC84BM Traps in

- Organic Bulk Heterojunction Solar Cells," *Advanced Functional Materials*, vol. 21, pp. 3083-3092, 2011.
- [105] C. van Berkel, *et al.*, "Quality factor in a-Si:H nip and pin diodes," *Journal of Applied Physics*, vol. 73, p. 5264, 1993.
 - [106] L. Li, *et al.*, "Photocurrent transients in polymer-fullerene bulk heterojunction organic solar cells," presented at the 38th IEEE Photovoltaic Specialists Conference (PVSC), Austin, TX., 2012.
 - [107] J. Tumbleston, *et al.*, "Analyzing local exciton generation profiles as a means to extract transport lengths in organic solar cells," *Physical Review B*, vol. 82, p. 205325, 2010.
 - [108] V. D. Mihailetschi, *et al.*, "Charge Transport and Photocurrent Generation in Poly(3-hexylthiophene): Methanofullerene Bulk-Heterojunction Solar Cells," *Advanced Functional Materials*, vol. 16, pp. 699-708, 2006.
 - [109] L. Tzabari and N. Tessler, "Shockley–Read–Hall recombination in P3HT:PCBM solar cells as observed under ultralow light intensities," *Journal of Applied Physics*, vol. 109, p. 064501, 2011.
 - [110] G. Li, *et al.*, "recent progress in modeling, simulation, optimization of polymer solar cells," *IEEE Journal of Photovoltaics*, vol. 2, pp. 320-340, 2012.
 - [111] R. C. I. MacKenzie, *et al.*, "Modeling Nongeminate Recombination in P3HT:PCBM Solar Cells," *The Journal of Physical Chemistry C*, vol. 115, pp. 9806-9813, 2011.
 - [112] W. Shockley and W. Read, "Statistics of the Recombinations of Holes and Electrons," *Physical Review*, vol. 87, pp. 835-842, 1952.
 - [113] R. Hall, "Electron-Hole Recombination in Germanium," *Physical Review*, vol. 87, pp. 387-387, 1952.
 - [114] S. Selberherr, Ed., *Analysis and simulation of semiconductor devices*. Wien, New York: Springer-Verlag, 1984, p.^pp. Pages.
 - [115] J. Dziewior and W. Schmid, "Auger coefficients for highly doped and highly excited silicon," *Applied Physics Letters*, vol. 31, p. 346, 1977.
 - [116] C. R. Paul, Ed., *Fundamentals of electric circuit analysis*. John Wiley & Sons, 2001, p.^pp. Pages.
 - [117] L. W. Nagel and D. O. Pederson, "Simulation program with Integrated Circuit Emphasis," presented at the 16th Midwest Symp. on Circuit Theory, Ontario, Canada, 1973.
 - [118] P. P. Boix, *et al.*, "Current-voltage characteristics of bulk heterojunction organic solar cells: connection between light and dark curves," *Advanced Energy Materials*, vol. 1, pp. 1073-1078, 2011.
 - [119] S. Dongaonkar, *et al.*, "Universality of non-ohmic shunt leakage in thin-film solar cells," *Journal of Applied Physics*, vol. 108, p. 124509, 2010.
 - [120] J. Guo, *et al.*, "Charge generation and recombination dynamics in poly(3-hexylthiophene)/fullerene blend films with different regioregularities and morphologies," *J. Am. Chem. Soc.*, vol. 132, p. 6154, 2010.
 - [121] G. F. Burkhard, *et al.*, "Accounting for Interference, Scattering, and Electrode Absorption to Make Accurate Internal Quantum Efficiency Measurements in Organic and Other Thin Solar Cells," *Advanced Materials*, vol. 22, pp. 3293-3297, 2010.

- [122] J. Y. Kim, *et al.*, "Efficient tandem polymer solar cells fabricated by all-solution processing," *Science*, vol. 317, p. 222, 2007.
- [123] S. Sista, *et al.*, "Highly Efficient Tandem Polymer Photovoltaic Cells," *Advanced Materials*, vol. 22, pp. 380-383, 2010.
- [124] J. Yang, *et al.*, "A Robust Inter-Connecting Layer for Achieving High Performance Tandem Polymer Solar Cells," *Advanced Materials*, vol. 23, pp. 3465-3470, 2011.
- [125] T. Trupke, *et al.*, "Improving solar cell efficiencies by down-conversion of high-energy photons," *Journal of Applied Physics*, vol. 92, p. 1668, 2002.
- [126] X. Y. Huang, *et al.*, "Broadband Downconversion of Ultraviolet Light to Near-Infrared Emission in Bi³⁺-Yb³⁺-Codoped Y₂O₃ Phosphors," *Journal of the American Ceramic Society*, vol. 94, pp. 833-837, 2011.
- [127] L. Aarts, *et al.*, "Downconversion for solar cells in NaYF₄:Er,Yb," *Journal of Applied Physics*, vol. 106, p. 023522, 2009.
- [128] X. Y. Huang and Q. Y. Zhang, "Efficient near-infrared down conversion in Zn₂SiO₄:Tb³⁺,Yb³⁺ thin-films," *Journal of Applied Physics*, vol. 105, p. 053521, 2009.
- [129] J. J. Eilers, *et al.*, "Efficient visible to infrared quantum cutting through downconversion with the Er³⁺-Yb³⁺ couple in Cs₃Y₂Br₉," *Applied Physics Letters*, vol. 96, p. 151106, 2010.
- [130] V. Badescu, *et al.*, "Improved model for solar cells with down-conversion and down-shifting of high-energy photons," *Journal of Physics D: Applied Physics*, vol. 40, pp. 341-352, 2007.
- [131] Z. e. R. Abrams, *et al.*, "Solar energy enhancement using down-converting particles: A rigorous approach," *Journal of Applied Physics*, vol. 109, p. 114905, 2011.
- [132] S. Fischer, *et al.*, "Enhancement of silicon solar cell efficiency by upconversion: Optical and electrical characterization," *Journal of Applied Physics*, vol. 108, p. 044912, 2010.
- [133] M. Liu, *et al.*, "Enhancing near-infrared solar cell response using upconverting transparentceramics," *Solar Energy Materials and Solar Cells*, vol. 95, pp. 800-803, 2011.
- [134] V. Badescu, "An extended model for upconversion in solar cells," *Journal of Applied Physics*, vol. 104, p. 113120, 2008.
- [135] V. Badescu and A. M. Badescu, "Improved model for solar cells with up-conversion of low-energy photons," *Renewable Energy*, vol. 34, pp. 1538-1544, 2009.
- [136] A. Shalav, *et al.*, "Luminescent layers for enhanced silicon solar cell performance: Up-conversion," *Solar Energy Materials and Solar Cells*, vol. 91, pp. 829-842, 2007.
- [137] A. C. Atre and J. A. Dionne, "Realistic upconverter-enhanced solar cells with non-ideal absorption and recombination efficiencies," *Journal of Applied Physics*, vol. 110, p. 034505, 2011.
- [138] S. Balushev, *et al.*, "Up-Conversion Fluorescence: Noncoherent Excitation by Sunlight," *Physical Review Letters*, vol. 97, p. 143903, 2006.

- [139] Y. Li and Y. Zou, "Conjugated Polymer Photovoltaic Materials with Broad Absorption Band and High Charge Carrier Mobility," *Advanced Materials*, vol. 20, pp. 2952-2958, 2008.
- [140] J.-H. Tsai, *et al.*, "Synthesis of new indolocarbazole-acceptor alternating conjugated copolymers and their applications to thin film transistors and photovoltaic cells," *Macromolecules*, vol. 42, pp. 1897-1905, 2009.
- [141] Y. Zou, *et al.*, "A thieno [3, 4-c] pyrrole-4, 6-dione-based copolymer for efficient solar cells," *Journal of the American Chemical Society*, vol. 132, pp. 5330-5331, 2010.
- [142] A. Mayer, *et al.*, "Polymer-based solar cells," *Materials Today*, vol. 10, pp. 28-33, 2007.
- [143] V. Kochergin, *et al.*, "Aluminum plasmonic nanostructures for improved absorption in organic photovoltaic devices," *Applied Physics Letters*, vol. 98, p. 133305, 2011.
- [144] H. A. Atwater and A. Polman, "Plasmonics for improved photovoltaic devices," *Nature Materials*, vol. 9, pp. 205-213, 2010.
- [145] M. I. Stockman, "Nanoplasmonics: past, present, and glimpse into future," *Optics Express*, vol. 19, pp. 22029-22106, 2009.
- [146] X. Chen, *et al.*, "Plasmon enhancement of bulk heterojunction organic photovoltaic devices by electrode modification," *Applied Physics Letters*, vol. 93, p. 123302, 2008.
- [147] M. A. Sefunc, *et al.*, "Plasmonic backcontact grating for P3HT:PCBM organic solar cells enabling strong optical absorption increased in all polarizations," *Optics Express*, vol. 19, pp. 14200-14209, 2011.
- [148] J. Yang, *et al.*, "Plasmonic polymer tandem solar cell," vol. 5, pp. 6210-6217, 2011.
- [149] G. Katsagounos, *et al.*, "Enhanced photon harvesting in silicon multicrystalline solar cells by new lanthanide complexes as light concentrators," *Journal of Luminescence*, vol. 131, pp. 1776-1781, 2011.
- [150] F. Wang, *et al.*, "Enhancement of the power conversion efficiency by expanding the absorption spectrum with fluorescence layers," *Optics Express*, vol. 19, pp. A361-A368.
- [151] D. Serrano, *et al.*, "Highly efficient energy transfer in Pr³⁺, Yb³⁺ codoped CaF₂ for luminescent solar converters," *J. Opt. Soc. Am. B*, vol. 28, pp. 1760-1765, 2011.
- [152] L. H. Slooff, *et al.*, "A luminescent solar concentrator with 7.1% power conversion efficiency," *physica status solidi (RRL) - Rapid Research Letters*, vol. 2, pp. 257-259, 2008.
- [153] W. G. Van Sark, *et al.*, "Luminescent Solar Concentrators – A review of recent results," *Optics Express*, vol. 16, pp. 21773-21792, 2008.
- [154] S.-Y. Wang, *et al.*, "Spectral coupling of fluorescent solar concentrators to plasmonic solar cells," *Journal of Applied Physics*, vol. 109, p. 074910, 2011.
- [155] J. Blakesley and D. Neher, "Relationship between energetic disorder and open-circuit voltage in bulk heterojunction organic solar cells," *Physical Review B*, vol. 84, 2011.

- [156] C. Groves, *et al.*, "Effect of Charge Trapping on Geminate Recombination and Polymer Solar Cell Performance," *Nano Letters*, vol. 10, pp. 1063-1069, 2010.
- [157] F. Etzold, *et al.*, "Ultrafast Exciton Dissociation Followed by Nongeminate Charge Recombination in PCDTBT:PCBM Photovoltaic Blends," *Journal of the American Chemical Society*, vol. 133, pp. 9469-9479, 2011.
- [158] D. Chen, *et al.*, "P3HT/PCBM Bulk Heterojunction Organic Photovoltaics: Correlating Efficiency and Morphology," *Nano Letters*, vol. 11, pp. 561-567, 2011.
- [159] L. F. Drummy, *et al.*, "Molecular-Scale and Nanoscale Morphology of P3HT:PCBM Bulk Heterojunctions: Energy-Filtered TEM and Low-Dose HREM†," *Chemistry of Materials*, vol. 23, pp. 907-912, 2011.
- [160] W. Wang, *et al.*, "High-efficiency polymer photovoltaic devices from regioregular-poly(3-hexylthiophene-2,5-diyl) and [6,6]-phenyl-C[₆₁]-butyric acid methyl ester processed with oleic acid surfactant," *Applied Physics Letters*, vol. 90, p. 183512, 2007.
- [161] H.-Y. Chen, *et al.*, "Fast-grown interpenetrating network in poly(3-hexylthiophene): methaofullerenes solar cells processed with additive," *J. Phys. Chem. C*, vol. 113, pp. 7946-7953, 2009.
- [162] K. Maturová, *et al.*, "Morphological device model for organic bulk heterojunction solar cells," *Nano Letters*, vol. 9, pp. 3032-3037, 2009.
- [163] C. Groves, *et al.*, "Simulation of loss mechanisms in organic solar cells: A description of the mesoscopic Monte Carlo technique and an evaluation of the first reaction method," *The Journal of Chemical Physics*, vol. 133, p. 144110, 2010.

APPENDIX A: PUBLICATIONS

- [1] **Kejia Li**, P. P. Khlyabich, Lijun Li, B. Burkhart, B. C. Thompson and J. C. Campbell, "Influence of exciton diffusion and charge-transfer state dissociation efficiency on the short-circuit current densities in semi-random donor/acceptor polymer:fullerene solar cells," *J. Phys. Chem. C.*, submitted, 2012.
- [2] **Kejia Li**, Lijun Li, J. C. Campbell, "Recombination lifetime of free polarons in polymer/fullerene bulk heterojunction solar cells," *J. Appl. Phys.*, Vol. 111, No. 3, pp. 034503 (2012).
- [3] **Kejia Li**, Lijun Li, P. P. Khlyabich, B. Burkhart, B. C. Thompson and J. C. Campbell, "Efficiency limitations in organic bulk heterojunction solar cells," *Photovoltaic Specialists Conference (PVSC), 2012 38th IEEE*, pp.003035-003039, 3-8 June 2012
- [4] **Kejia Li**, Yang Shen, Lijun Li, Petr Khlyabich, Ellen S. Reifler, Barry C. Thompson and Joe C. Campbell (2011). "Thermal Annealing Effect on P3HT:PCBM Free Polarons Lifetime and Charge Transport," *MRS Proceedings*, pp. 1322, mrss11-1322-b09-11, 2011.
- [5] **Kejia Li**, Yang Shen, N. Majumdar, Chong Hu, M. C. Gupta, J. C. Campbell, "Determination of free polaron lifetime in organic bulk heterojunction solar cells by transient time analysis ", *J. Appl. Phys.*, Vol. 108, No. 8, pp. 084511 (2010).
- [6] **Kejia Li**, H. Liu, Q. Zhou, D. C. McIntosh, and J. C. Campbell, "SiC avalanche photodiode array with microlenses," *Optics Express*, vol. 18, no. 11, pp. 11713-11719, 2010.

- [7] Lijun Li, **Kejia Li**, P. P. Khlyabich, B. Burkhardt, B. C. Thompson and J. C. Campbell, "Photocurrent transients in polymer-fullerene bulk heterojunction organic solar cells," *Photovoltaic Specialists Conference (PVSC), 2012 38th IEEE*, pp.002756-002760, 3-8 June 2012.
- [8] Yang Shen, **Kejia Li**, N. Majumdar, M. C. Gupta, J. C. Campbel, "Bulk and contact resistance in P3HT:PCBM heterojunction solar cells", *Solar Energy Materials and Solar Cells.*, Vol. 95, No. 8, pp. 2314-2317 (2011).
- [9] Yang Shen, **Kejia Li**, N. Majumdar, M. C. Gupta, J. C. Campbel, "Contact resistance in P3HT:PCBM heterojunction solar cells", *2011 MRS Spring Meetings*, OO10.18, 25-29 April 2011.